Smooth Inductively Coupled Ring Trap for Cold Atom Optics

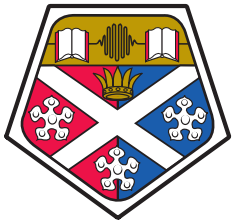

Aline Dinkelaker

Department of Physics and SUPA

University of Strathclyde

A thesis presented in the fulfilment of the requirements for the degree of

Doctor of Philosophy

2013

This thesis is the result of the author's original research. It has been composed by the author and has not been previously submitted for examination which has led to the award of a degree.

Signed:

Date:

Für meine Eltern und meinen Bruder.

Abstract

The main topic in this thesis is the proof-of-principle experiment for an inductively coupled magnetic ring trap for applications in atom interferometry and quantum gas investigations. Atom interferometry utilises the wave nature of atoms for precision measurements of gravitational and inertial effects and to test fundamental physics.

Due to their symmetry, their periodic boundary conditions and their large enclosed areas, ring traps provide attractive geometries for atom interferometry. By tightening the trap and reducing the trap radius, toroidal traps also have excellent conditions to study superfluid properties in degenerate gases.

The trapping potential for the inductively coupled magnetic ring trap is formed by the superposition of an external AC field and a local AC field, created by the induced current in a copper ring. These fields cancel in a ring and create a time-averaged trapping potential. By inducing the current in the conductor and using AC over DC fields several problems of existing trapping mechanisms are addressed. We create a smooth, scalable trapping potential for cold atoms.

We load the inductively coupled ring trap with $\sim 10^6$ laser cooled ^{87}Rb atoms. The atoms can be observed evolving around the ring in the horizontal plane, until the ring is completely filled. We record vacuum limited lifetimes of ~ 1.3 s after initial Majorana losses. With an added offset field we also gain flexibility in the trap geometry regarding the radius (~ 5 mm) and the trap width (~ 0.5 mm).

In a subsequent experiment, the setup and the ring trap parameters are changed to allow for the creation of ^{87}Rb Bose-Einstein condensate and for the implementation of atom interferometry in the ring trap. A vertical, smaller ring trap with a radius of ~ 1.8 mm is created. Laser cooled atoms are loaded either at the top or at the bottom of the ring.

Acknowledgements

I have gratitude and respect for my supervisors Erling Riis and Paul Griffin; I have learnt so much from you over the past years. A big thank you for showing me a very progressive approach to experimental physics, for answering hundreds of questions and for guiding me through the maze that is thesis writing. Thanks for your near infinite patience with me. Jon, my thanks go out to you, not only for taming the LabVIEW beast and Matlab codes but also for all the great work in the lab and your explanations and support. Aidan, you were not my supervisor but this didn't stop me from knocking at your office door when I had questions; thanks for your help over the years.

Ewan and Bob, our lab is full of proof of the amazing work you have done! Thank you so much for all the beautiful parts you have built in great detail, for your help with every design that I scribbled on a piece of paper and for cheering me up whenever I visited you in the workshop.

Thanks also to the electronics workshop. Not only did you produce all those nice circuits, your knowledge and help has saved me more than once. And of course, thanks to the IT team, when switching it off and on again just wasn't enough. I would also like to mention the friendly atmosphere in the physics department and the support for us student from the university staff, especially from the secretaries.

My regards also go to my partners in crime who have already left: Matt, Chris, Neal and Chidi. I also wish the best to everyone in the photonics group who makes this a lovable and social place (with top-notch research, of course): Pedro, Yoann, Savino, Jesus, Chris, Billy, Graham, Elmar, Andrew, James, Nicolas, Dylan, Jakob, Andreas, Thorsten and Stefan. It has been great to be able to

learn from you all and to have this kind of exchange and interaction between our groups.

Research and studying is a big part of the PhD experience but it is not everything. Being able to talk about the research and to get excited and exchange ideas is equally important. I was lucky enough to attend a number of summer schools and conferences, which always kick-started my motivation. This is a good place to note that my time here was heavily influenced by my participation in the student chapter SCOPE: I had a wonderful time with you all, especially at IONS and the leadership meetings. The physics community out there is fantastic and I hope that these bonds and the fun we shared will not cease after finishing the PhD. If we keep this spirit alive, we can achieve so much more.

Friends and family are a substantial part of my life. You were always there for me, especially when times were difficult. Andrew, thanks for being there for me every day and for being such a superawesome boyfriend. Best wishes go to all the friends I have made throughout my PhD: for the climbing, hiking, philosophical discussions and all the fun we had. I miss having you around but I am looking forward to seeing what the future brings for all of us. I am also grateful for my good friends back home and around the globe. Finally, I would not have been able to start or finish my PhD without the endless support of my parents.

It were an exciting three and a half years and I am curious about what comes next. There is one thing that I really want to do - a wee sarcastic rover says it best:

"Let's do a science!"

Contents

List of Figures

List of Tables

Chapter 1

Introduction

Atom interferometry is one of the most promising tools to have emerged from the increasing control gained over atoms during the last decades. I am fascinated by the prospect of gravitational wave detection with atoms: we can potentially observe ripples in space-time that are caused by inspiralling black holes and neutron stars – some of the most exotic objects imaginable. Not only that, with gravitational waves we might also unravel the secrets of the early universe during the Dark Ages, from which no light can reach us, or even answer the question about the fabric of the cosmos, be it stringy or looped. All this big scale physics is projected onto a small quantum object called atom, which does crazy things such as behaving like a wave and being in two places at once. In an atom interferometer we try to extract information about the surrounding world from the atoms. Every step on the way to improving atom interferometry is important, and the atom trap described in this thesis will hopefully add to that and increase our possibilities further.

1.1 Thesis outline

We here describe the realisation of an inductively coupled magnetic ring trap for cold atoms. Our design is mainly motivated by the application of atom interferometry, and the Introduction will provide the necessary background information to understand our considerations. We finish the Introduction with a brief

overview on the different techniques to create toroidal atom traps, which leads to a description of our technique and the theory behind the ring trap in Chapter 2, including simulations of the trapping potential. The experimental setup for the first generation of the ring trap, which is a successful proof-of-principal experiment for the inductively coupled ring trap with ^{87}Rb atoms, is described in Chapter 3. After an explanations as to how the data is analysed in Chapter 4, the results are discussed in Chapter 5. The findings have also been published [1].

A second generation of the ring trap experiment has been built, to allow for the implementation of atom interferometry with a Bose-Einstein condensate (BEC) in the ring trap. The changes with respect to the first generation, the setup and the successful loading of the new ring trap with cold atoms, as well as the creation of a BEC in the ring region, are shown in Chapter 6.

1.2 Motivation

Atoms are fascinating things. The atoms' most intriguing properties include their strong interaction with electromagnetic waves, their quantum nature and the atomic wavefunction (see below), and also the fact that they condense to a new state of matter (Bose-Einstein condensate), which leads to effects such as superfluidity. Studying and utilising these properties mostly require the atoms being trapped, i.e. confined in space. Atom optics are therefore designed to trap or guide the atoms in the desired geometry. A ring provides a unique, versatile trapping geometry: it is symmetric, it has periodic boundary conditions making it an infinitely long waveguide that guides the atoms back to their initial position, therefore removing the need for a mirror. Additionally, it can create a quasi 1D-geometry by tightening the trap to limit atomic motion to the azimuthal direction.

There are several ways to create a toroidal trapping potential for atoms, and an overview will be presented below. By combining existing solutions for atom trapping with a new method to create a ring potential, we have built the first inductively coupled magnetic ring trap for cold atoms. Following the proposal in Griffin et al. [2], it is realised by placing a circular conductor (a copper ring) in a homogeneous AC field [1]. The current inductively induced in the conductor

creates a magnetic field of opposite direction, falling off radially from the inner edge of the copper ring. As a result of the superposition of both these fields, a time-varying circle of magnetic zeros forms that time-averages to a toroidal potential minimum in the plane of the ring. With this method, we can avoid current carrying wires to the circular conductor, which would destroy the otherwise cylindrical symmetry. For reasons common to magnetic traps (*Majorana spin-flips*, see Section 2.1), we need to add an offset field to avoid atom loss.

Similar to fibres in light interferometers, ring traps can be used as waveguides for atom interferometers, where the two arms of the interferometer are then provided by the ring when the wavepackets travel in opposite directions. At the time of writing, atom interferometry in rings has been performed by two groups [3, 4], and our ring trap is designed and built with interferometry applications in mind. Atom interferometry is an exciting and constantly expanding subject: already, it is used as an accelerometer to precisely measure inertial effects under micro gravity [5], gravitational acceleration [6] and rotation [7]. Atom interferometry can be used to measure fundamental constants, such as $\frac{h}{m}$ (via the recoil frequency), from which the fine structure constant α can be inferred [8]; techniques are developed to test fundamental physics such as QED (via α, see [8]) and general relativity [9, 10, 11, 12]. Different experiments on Earth and in space for the detection of gravitational gradients [13, 14] and gravitational waves [15, 16] – complementing the bandwidth of existing optical interferometers – are proposed. An additional advantage to the obtainable precision is that atom interferometers can be scaled down, and small interferometry systems on chips exist [17, 18]. Commercially available small scale cold atom systems and atom chips (e.g. ColdQuanta) simplify the scientific progress in this area. The working principle of atom interferometry will be introduced in Section 1.4. But first, to provide the necessary background information, we briefly describe atom-light interaction – specifically in the context of atomic cooling and trapping – and the wave nature of atoms, which is the reason for interference effects between atoms.

1.3 Atom waves and optical cooling

The interaction of atoms with light and wave-particle duality are two important features that are constantly pushing the boundaries in the field of atomic physics. The fact that the internal atomic states can be manipulated with magnetic and electric fields (making use of the Zeeman- and Stark-effects) and that we can address specific atomic transitions means that we have a high level of control over the absorption and emission of light. In the context of this experiment it not only enables laser cooling via absorption of red-detuned light [19, 20] and using light for atom diffraction [21, 22], but it also opens the door for other exciting possibilities, such as entanglement of atoms via interaction with light in a cavity [23, 24, 25] and superradiant emission [26].

It is the fascinating wave-particle duality of atoms in close analogy to light, which makes atom interferometry possible. Throughout history, the nature of light and matter has been a puzzle for scientists and philosophers. From Maxwell's equations for the propagation of electromagnetic waves in the 19th century onwards, light was mainly thought to have wave properties, until Einstein recognised its particle properties [27]. Atoms on the other hand were assumed to behave solely as particles, until de Broglie ascribed to all matter – including atoms – a wavelength, using the de Broglie relation [28]

$$\lambda_{\mathrm{dB}} = \frac{h}{p} \,, \tag{1.1}$$

where $p = mv$ is the particle's momentum. As with light, which can be used to build highly sensitive interferometers, the wave nature of atoms may be used to create interference, e.g. in an atomic version of Young's double slit interferometer [29] or even with a single atom [30]. Example images of light and atom interference are shown in Figure 1.1. As all matter has an associated wavelength, interference is not an effect observed exclusively for atomic particles (interference effects in electrons and neutrons have been observed much earlier than for atoms, in the 1920s and 30s). Working towards interference of larger objects (e.g. C_{60} molecules [31]) increases the scale on which quantum effects are visible.

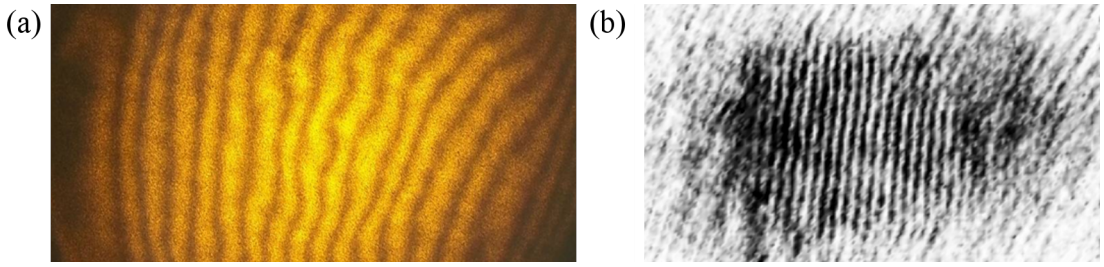

Figure 1.1: (a) Interference pattern from a Mach-Zender interferometer with 589 nm light and (b) interference pattern from atomic matterwaves. Image (b) from A. Arnold, based on [32].

A well known example of the power of atom interferometry is the Sagnac effect: in a Sagnac interferometer with area A and rotational velocity Ω_{rot}, the phase difference for a wave of wavelength λ and a propagation velocity v is [33]

$$\Delta\Phi = \frac{4\pi A\Omega_{\mathrm{rot}}}{\lambda v} \ , \tag{1.2}$$

which means that the sensitivity (for the same interferometer) has a ratio of

$$\frac{\Delta\Phi_{\mathrm{atom}}}{\Delta\Phi_{\mathrm{light}}} = \frac{\lambda_{\mathrm{light}}c}{\lambda_{\mathrm{dB}}v} \tag{1.3}$$

$$= \frac{mc^2}{\hbar\omega_{\mathrm{light}}} \ . \tag{1.4}$$

The ratio of energy carried by atoms ($E = mc^2$) compared to photons ($E = \hbar\omega$) means that atoms have the potential to be more sensitive to measure inertial effects: taking ^{87}Rb and $\lambda_{\mathrm{light}} = 780$ nm as an example, the sensitivity per particle for atoms is larger by a factor of $\frac{\Delta\Phi_{\mathrm{atom}}}{\Delta\Phi_{\mathrm{light}}} \approx 5 \times 10^{10}$ (see also e.g. [33, 34, 35]).

The strong interaction of atoms with gravitational and electromagnetic fields not only leads to high sensitivity, it is also the reason that atoms can be trapped, e.g. in a magnetic trap like our ring trap or in optical dipole traps made of light. For trapping to work, the atoms have to be sufficiently cold. Commonly, radiative cooling in a magneto-optical trap (MOT) and optical molasses are used, which comes back to manipulating atoms using light. These methods form important building block for many atom experiments – including ours – and the

basic mechanisms are introduced in the following Section.

1.3.1 Optical cooling and magneto-optical trapping

Cooling atoms with light is a crucial tool for subsequently trapping them, because atoms with energies higher than the necessarily finite trap depths will escape (when $E_{\text{trap}} < E_{\text{kin}}$). The depth of the trapping potential can be expressed as a temperature, which is typically of the order of hundreds of μK to several mK. Our atoms at room temperature are much hotter than that ($\sim$ 300 K) so that the vast majority will not feel the effect of the potential. Therefore, the first step of our experiment is to sufficient optically cool the atoms to trap them in the ring. Cooling is also a necessary step for creating a BEC (see e.g. [36]), which is important for the second generation experiment. For complete and extensive reviews of atom cooling and manipulation using light, see e.g. [37, 38].

The working principle of optical cooling is photon momentum transfer during photon absorption to decrease an atom's kinetic energy, see [39]. Because the momentum transfer for each absorption is $\hbar k$, where $k = 2\pi/\lambda$ is the wave-vector of the laser light, and the velocity change is very small ($\hbar k/m$ is of the order of a few cm/s [38, 39]), many absorption-emission cycles are needed. This makes a *closed transition* vital, in which an atom only decays back into the initial state, so that it stays in resonance with the cooling light (additional *repump light* brings "lost" atoms back into the cooling cycle). Alkali atoms are often used for experiments requiring laser cooling, as they have a single valence electron and thus lack the transitions that arise from coupling between multiple electrons on the same valence shell. For the Doppler cooling scheme, we approximate the atom as a two-level system, with the hyperfine states F and F' being the ground and excited state, respectively. The next Sections describe the process of Doppler and sub-Doppler cooling in an *optical molasses*, as well as the closely related magneto-optical trap (MOT).

1.3.1.1 Doppler cooling

Optical molasses is generally implemented in three dimensions but, for simplicity, here we start by looking at the cooling process in 1D: we consider a gas of two-level

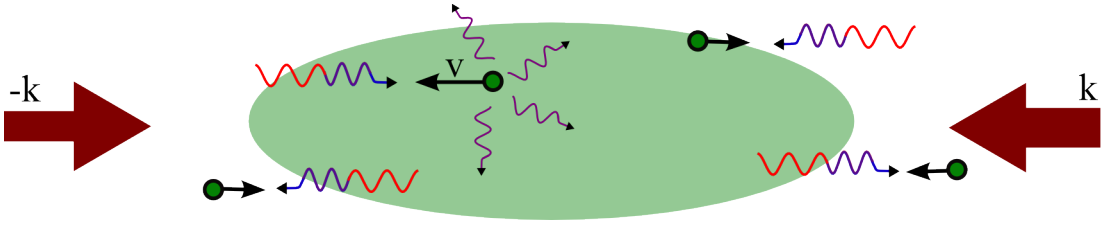

Figure 1.2: Schematics of Doppler cooling: atoms are irradiated by two counter-propagating laser beams that are red-detuned in the lab frame. Atoms moving towards one of the beams with velocity v see a blue-shifted frequency, which leads to a higher scattering rate of that light and hence cooling.

atoms at room temperature inside a vacuum chamber. Two counter-propagating laser beams with a frequency below the atomic cooling transition frequency ("red-detuned") irradiate the gas. A schematic of the situation is shown in Figure 1.2. If an atom moves *towards* a beam, it sees the frequency of the light Doppler shifted closer to resonance, which leads to enhanced absorption and thus increases the scattering rate (equivalently, scattering decreases when the atom moves away from the beam) [40]:

$$\gamma_{\mathrm{sc}} = \frac{\Gamma}{2} \frac{I/I_{\mathrm{sat}}}{1 + I/I_{\mathrm{sat}} + (2(\Delta - kv)/\Gamma)^2} \ , \tag{1.5}$$

where Γ is the transition linewidth and I_{sat} the saturation intensity of the atoms; the light has the intensity I and the detuning from resonance Δ, which is altered by the Doppler shift, kv, due to the atomic motion. Taking the scattering rates from both beams into account (towards and away from the atoms) results in a velocity dependent, "viscous" damping force for small v (the capture range is $\sim \pm\Gamma/k$ [34]):

$$F = -\alpha \ v \ . \tag{1.6}$$

For cooled atoms with a velocity approaching $v = 0$, heating due to the stochastic nature of the absorption and emission becomes significant [40]. The balance between cooling and heating forces defines the minimum kinetic energy, which is expressed in the Doppler temperature:

$$T_D = \frac{\hbar\Gamma}{4k_B} \frac{1 + (2\Delta/\Gamma)^2}{2|\Delta|\Gamma} \ . \tag{1.7}$$

The Doppler cooling limit is the minimum Doppler temperature $T_{\mathrm{Dmin}} = \frac{\hbar\Gamma}{2k_B}$, which is achieved for $\Delta = -\Gamma/2$ [40]. For ^{87}Rb, this is 146 μK [41]. An extension of optical molasses to three dimensions requires to consider the force acting on the velocity components along different directions, a discussion can be found in [40]. Three-dimensional optical molasses has first been created by the group of Chu [20].

1.3.1.2 MOT

The mechanisms described above cool the atoms by decreasing their kinetic energy, but they don't confine them. After a sufficiently long time, atoms diffuse out of the cooling volume. In a magneto-optical trap (MOT) cooling and trapping mechanisms are combined, as first demonstrated by Raab et al. [42]. To explain the trapping, we have to leave the two-level atom behind and take the magnetic sub-levels (m_F-levels) into account.

As for the 3D molasses, six red-detuned beams overlap in a central region, with two-counter-propagating, circularly polarised beams on each axis. Additionally, magnetic coils in an anti-Helmholtz configuration produce a quadrupole (QP) field (a linearly varying magnetic field, $B(x, y, z) = (-B_{\mathrm{QP}} \cdot x, -B_{\mathrm{QP}} \cdot y, 2B_{\mathrm{QP}} \cdot z)$, with a magnetic field zero in the centre at which point it changes direction).

Here, the 1D-case is described for the x-direction, but it can be extended to 3D in a similar manner to the previous discussion on optical molasses. A schematic for the 1D-case is shown in Figure 1.3.

If an atom moves out of the zero magnetic field the Zeeman splitting shifts the energy of the different m_F-levels by an amount proportional to the magnetic field magnitude, $\Delta E \propto g_F m_F |\vec{B}|$. For simplicity, let us consider an atom in the $|F = 0, m_F = 0\rangle$ ground state, which can be excited into the $|F' = 1, m_{F'} = -1, 0, 1\rangle$ states. With circularly polarised light, we can either excite the atom into the $|F' = 1, m_{F'} = 1\rangle$ state (σ^+ polarisation for $\Delta m_F = 1$ transitions) or into the $|F' = 1, m_{F'} = -1\rangle$ state (σ^- polarisation for $\Delta m_F = -1$ transitions). Regarding the transitions, the σ-polarisation is defined with respect to the magnetic field axis, where σ^- refers to a clockwise rotation around the magnetic field, along the magnetic field direction, and σ^+ refers to the anti-clockwise rotation.

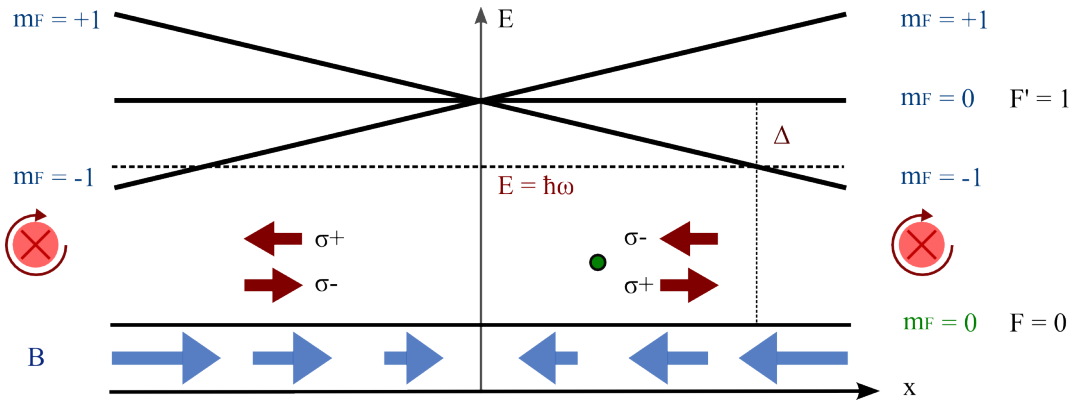

Figure 1.3: Schematic of a MOT in 1D: an atom in the $|F = 0, m_F = 0\rangle$ ground state at position x experiences a shift of its $|F' = 1, m_{F'}\rangle$ magnetic sub-levels due to the magnetic field (blue arrows). This reduces the detuning, Δ, of the light with appropriate polarisation (σ^- for $\Delta m_F = -1$) and enhances absorption of the incoming laser beam. The handedness is shown left of the diagram for the beam going from $-x$ to $+x$ and on the right for the beam going from $+x$ to $-x$. The polarisation for each beam with respect to the magnetic field is shown at $x < 0$ and $x > 0$.

While the handedness with respect to the direction of light propagation stays constant along x (in our example we have clockwise rotation of the electric field vector when looking along the direction of beam propagation for both beams), the polarisation with respect to the magnetic field axis inverts at $x = 0$, as the magnetic field changes direction. Thus the same beam drives different transitions at different positions.

For an atom moving along $x > 0$ where $B < 0$, it not only sees the Doppler shift as for optical molasses, but also the energy of the sub-levels with $m_{F'} < 0$ is lowered (in our example, $g_F > 0$). This brings the atom closer to resonance with the red-detuned light, and it absorbs a photon with the correct circular polarisation, σ^-. The handedness of the light is chosen such that the *incoming* beam is absorbed, and the atom gets a momentum kick towards the centre. An atom moving along $x < 0$ also has the $m_{F'} < 0$ level shifted closer to resonance, but because the magnetic field axis changes, it now absorbs a photon from the opposite laser beam (σ^-) and also experiences a momentum kick towards the centre. The further the atoms move along x, the stronger the energy shifts due

to B, which changes the coupling to the light. This leads to not only a damping force with v, but also a restoring force along x,

$$F = -\alpha\ v - \beta\ x, \tag{1.8}$$

which causes the atoms to accumulate in the field minimum at the centre of the trap [34].

Not all atoms from a room temperature gas of atoms can be captured by the MOT, and only atoms with velocities below the capture velocity, v_c, can be cooled and trapped. The capture velocity of the MOT for a given atomic species depends on the magnetic field gradient ($\mathrm{d}B/\mathrm{d}x$), the laser beam size and on the detuning from the atomic resonance. This is important for our cooling laser frequency shifts in the experimental setup.

1.3.1.3 Sub-Doppler cooling

It turns out that optical cooling is *not* limited by the Doppler temperature, and "sub-Doppler cooling" was first observed in an optical molasses by the group of Phillips [43]. To explain the apparent additional cooling, atomic sub-levels and the polarisation of the light become important. This Section does not aim to explain sub-Doppler cooling in great detail, it is succinct to merely give an idea of the mechanisms at work. A thorough theoretical and experimental discussion of the 1989 sub-Doppler cooling experiment by the group of Chu can be found in [44] and [45], respectively.

The molasses setup is the same as in Section 1.3.1.1, with six counter-propagating beams (and no magnetic fields), but we will restrict the discussion to the 1D-case. The two beams along the x-axis have opposite circular polarisation, σ^+ and σ^-, which interfere to produces a standing wave with linear polarisation that varies orientation along x (see e.g. [37, 38]). This is also shown in Figure 1.4.

The spatially varying polarisation of the light locally optically pumps the atoms into the most light shifted magnetic sub-state. Let us chose as an example an atom in the $F = 1$ ground state, with the magnetic sub-levels $m_F = -1, 0, 1$ and the $F' = 2$ excited state, with $m_{F'} = -2, -1, 0, 1, 2$. We only regard the dynamics of the ground state. For linearly polarised light, the transitions

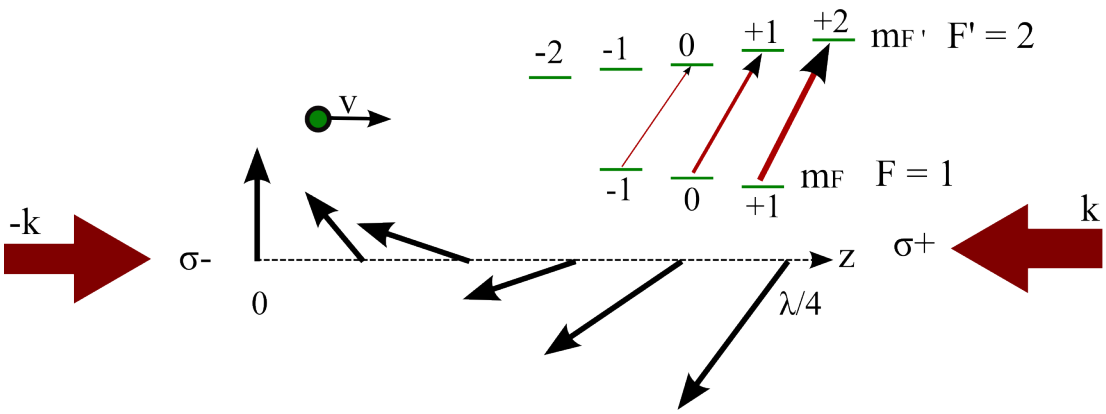

Figure 1.4: Sub-Doppler cooling: two counter-propagating, opposite circular polarised beams produce a standing wave with linear polarisation. The polarisation axis changes with position x. While for an atom at rest, the $m_F = 0$ state is most coupled to the linear polarised light, an atom moving with v causes stronger coupling of magnetic sub-states with $m_F = 1$. This increases scattering of σ^+ light and causes damping. The Figure is based on [37, 38].

for atoms at rest would be coupled such that the atoms are pumped into the $|F = 1, m_F = 0\rangle$ state. For moving atoms, this depends on the direction of motion. First of all, atoms moving toward the σ^+ (σ^-) beam are Doppler-shifted closer to resonance and therefore undergo $\Delta m_F = +1$ ($\Delta m_F = -1$) transitions. After several absorption cycles, the atoms are pumped into the state $|F = 1, m_F = +1\rangle$ ($|F = 1, m_F = -1\rangle$). Additionally, the motion along x and the consequently changing quantisation axis leads to coupling of the $|F = 1, m_F = 1\rangle$ ($|F = 1, m_F = -1\rangle$) states to the light field field such that the population transfer increases the scattering rate for σ^+ (σ^-) light further. With the coupling proportional to v, this leads to a damping force (see [37, 38]). For a detailed description, see [46].

As before, the atoms are heated by stochastic absorption and emission processes, so that the minimum temperature obtainable is proportional to I/Δ [46]. Fundamentally, the cooling with this method is limited by the recoil the atom gets from spontaneous emission. This defines the recoil temperature, $T_{\text{rec}} = \hbar^2 k^2 / m k_B$ [47], which is 362 nK for ^{87}Rb [41]. Experimentally, the lowest temperatures achieved with optical molasses are several T_{rec} [48].

In the experimental sequence, we start with a MOT and then release the atoms

into the optical molasses for sub-Doppler cooling. During the optical molasses phase, the magnetic fields are switched off, the light is detuned further from resonance and the intensity of the light beams lowered compared to the MOT, to achieve colder temperatures.

For radiative cooling to work efficiently in a MOT and optical molasses, frequency stability is of importance. As the cooling depends on the detuning, it is essential to have a stable laser, with a linewidth smaller than the linewidth of the atomic transition and the detuning; in practice, the laser linewidth is narrowed to $\sim \Gamma/10$.

1.3.2 Temperature

It has been addressed [40, 47] that the term "temperature" in thermodynamics is defined for a system in thermal equilibrium with its surrounding, requiring that a heat exchange can take place. During laser cooling, atoms are in a different situation as there is energy exchange, but no heat exchange with the surrounding. Nevertheless, the definition below for the temperature of cooled atoms has been justified, see [40, 47]. For laser cooled atoms, the temperature is defined via the kinetic energy (in 1D) [47]:

$$\langle E_{\text{kin}} \rangle = k_B T/2 \ . \tag{1.9}$$

For this to be a valid description, the momentum distribution of the atomic cloud must be a Maxwell-Boltzmann distribution, which has then the momentum spread

$$\Delta p = \sqrt{k_B T m} \ , \tag{1.10}$$

see Figure 1.5 (a). Cooling therefore corresponds to reducing the momentum spread of the atomic cloud [35]. To measure the temperature of a cloud of atoms experimentally, we use a time of flight method. Here, the spatial atom distribution is imaged at different times, so that the initial velocity distribution can be inferred from the *change* in spatial width with time (see e.g. [35, 43]):

$$\sigma^2(t) = \sigma_0^2 + \Delta v^2 t^2 \ , \tag{1.11}$$

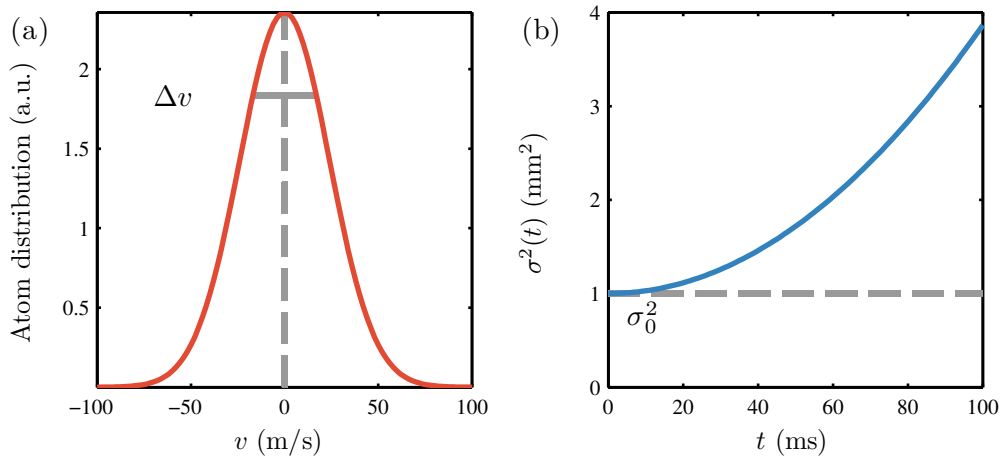

Figure 1.5: (a) 1D Maxwell-Boltzmann distribution of velocity, v, for ^{87}Rb atoms at $T = 3$ K. The grey lines indicate the momentum spread, Δv, and the mean momentum, v_0. (b) The initial velocity distribution determines the spatial distribution σ of an atom cloud with initial size σ_0 after a time of flight, t.

from which the temperature can be extracted, see Figure 1.5 (b). The time of flight method is also explained in the context of our data analysis in Section 4.4.

1.4 Atom interferometry

The first proposed application of our apparatus is atom interferometry. A good review and in-depth explanations of the topic can be found in [34, 35]. This Section will introduce the main principles so that the motivation for the ring trap and its future application can be better understood.

Atom interferometry utilises the wave nature of atoms. As in light interferometry, the wavepacket is split, travels along two different paths (the "arms" of an interferometer) and is then recombined to produce an interference pattern, which depends on the phase of the waves incident from each arm. Throughout this Section, we will discuss the Mach-Zender interferometer as an example, which is schematically shown in Figure 1.6. Our starting point is a cloud of atoms, with the individual atomic wavefunctions forming the wavepacket with an initial momentum p_0. The wavepacket is split coherently and the atoms are brought into

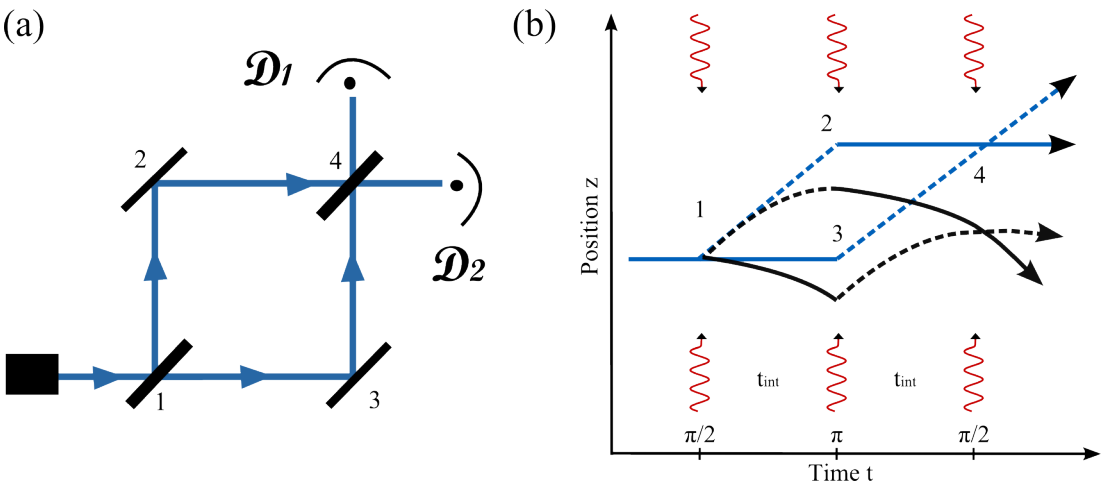

Figure 1.6: (a) The two paths of a Mach-Zender interferometer: 1–2–4 and 1–3–4. (b) Schematic of an atom interferometer, using standing light waves as beamsplitters ($\pi/2$-pulse) and mirrors (π-pulse). If the action along the paths 1–2–4 and 1–3–4 differ then the atoms accumulate a different phase while propagating along the paths. The atoms have an initial momentum p_0 (here: $p_0 = 0$, solid line), which is changed during the interaction with standing light waves to $p_0 + \Delta p_l$ (dashed line). The paths are shown without (blue) and with (black) the effect of gravity.

a superposition of travelling along path 1–2–4 and along path 1–3–4. During the propagation, a phase difference is accumulated in each path. For the propagation of the wavepacket from position 1 with $z = z_1$, $t = t_1$ to position 2 with $z = z_2$, $t = t_2$, the wavefunction at position 2 is [49]:

$$\psi_2(z_2, t_2) = e^{iS/\hbar}\psi_1(z_1, t_1) \ , \tag{1.12}$$

where S is the (classical) action along the path:

$$S = \int_{t_1}^{t2} L(z, \dot{z})dt \ , \tag{1.13}$$

with the Lagrangian $L = E_{\text{kin}} - E_{\text{pot}} = \frac{1}{2}m\dot{z}^2 - mgz$ for the 1D path along z. The accumulated phase along the two arms of an interferometer differs depending on the energy in each path. After recombination, this phase difference between the split parts of the wavepacket produces interference, which is mapped onto state

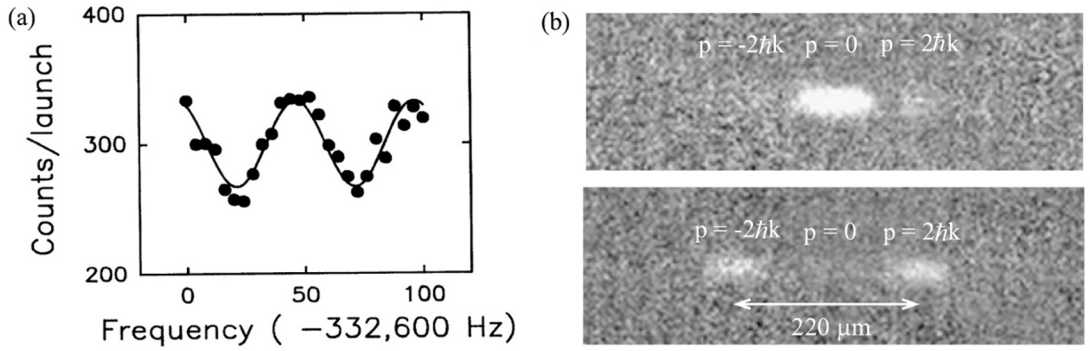

Figure 1.7: Two different ways to measure the phase in atom interferometry: (a) the phase is mapped onto the population in a specific internal state, Figure from [51], (b) the phase is extracted from population in different momentum states that separate spatially after re-combination, Image from [17].

population or atom momentum [50] and can be monitored by counting the atoms appropriately: by internal state selective detection, or by detecting atoms in one spatial position via e.g. fluorescence, absorption or ionisation [50]. Examples are shown in Figure 1.7 (a) and (b), respectively. In this context we will only consider atom interferometers with different spatial paths, i.e. different centre of mass motion, as opposed to splitting with respect to solely internal states.

1.4.1 Splitting and reflecting the atomic wavepacket

To split the atomic wavepacket and guide it along the paths of the interferometer, we need atom optics equivalents of beamsplitters and mirrors. Although matter gratings can be used to spatially separate particles (as demonstrated for atom interferometry in [52], see also [34, 35, 50]), more important for us is the use of *standing light waves* created from two counter-propagating waves as splitting and deflecting elements (a discussion can be found in [53]). The cloud is spatially separated by transferring the atoms into a superposition of different momentum states, using a pulsed standing-wave field. We use subsequent pulses to reflect and re-combine the atoms. To imitate the different optical elements of a light interferometer for an atom interferometer, the duration of each pulse is adjusted. If we apply the pulse for a duration equal to the $\pi/2$ time of a Rabi cycle then we

create a superposition of moving and non-moving atoms (assuming atoms initially at rest in the lab frame, $p_0 = 0$). This is called a "$\pi/2$-pulse", and it acts as a beamsplitter at the start of the sequence, splitting the wavepacket. Equivalently, a pulse with duration of the π time of a Rabi oscillation swaps the momentum of the states - atoms with $p = 0 \rightarrow p = 2\hbar k$ and $p = 2\hbar k \rightarrow 0\hbar k$. This "$\pi$-pulse" has the effect of a mirror for atomic waves. Re-combination of the atomic wavepackets is achieved via another $\pi/2$-pulse. Figure 1.6 (b) shows a schematic of the atom interferometer sequence using standing light waves as atom optics. As an example for atom interferometry using standing light waves, let us look at an early atom interferometer from Kasevich and Chu [51].

1.4.2 Example: the first cold atom interferometer

The first cold atom interferometer for inertial measurements was realised by Kasevich and Chu in 1991 [51]. The experiment is based on an atomic Mach-Zender type interferometer, similar to Figure 1.6 (b), and is built to measure the acceleration due to gravity. In their setup, cold sodium atoms from an atomic fountain propagate along z (with gravity acting along z), parallel to the splitting light. The atomic wavepacket is split using Raman pulses, which couple internal states to momentum states. The atoms are then in a superposition of $|F = 2, m_F = 0, p\rangle$ and $|F = 1, m_F = 0, p + 2\hbar k\rangle$. With a velocity recoil of $v_r = 2\hbar k/m \approx 6$ cm/s, a spatial separation of the order of 1 cm is achieved after 0.5 s. After recombination, the population in the $F = 2$ state is detected and recorded as a function of the recombination light frequency, as shown in Figure 1.7 (a). The phase is extracted from the sinusoidal fit to the data, and g is calculated. After several repetitions, a total integration time of 1000 seconds is achieved with a sensitivity to changes in g at the level of 3×10^{-6}.

1.4.3 Sensitivity

The sensitivity of an atom interferometer depends on the number of atoms involved in the measurement, N, the interrogation time, Δt_{int}, the coupling to the measurand and the coherence of the states.

For improving sensitivity by increasing the number of particles involved in the measurement, atoms have a disadvantage over photons: it is easier to increase the number of photons in an interferometer than to increase the number of atoms. Nevertheless, gyrometers for rotational sensing using atoms already compare favourably with laser gyrometers [33]. A bigger potential for better sensitivity lies in longer interaction times, Δt_{int}, by making the paths longer. The path length is mainly restricted by the coherence of the atoms, which limits the visibility of the interference pattern. We will consider coherence below. Additionally, the motion of the atoms (due to gravity, or thermal velocity) out of the observation region of the experimental setup restricts the path length. The latter can be avoided by using guided interferometers [54]. To enhance coupling to the measurand, we can prepare the atoms in the optimum atomic state (e.g. magnetically sensitive states for measuring magnetic fields), or choose an optimum geometry (e.g. large area for Sagnac interferometry). To gain sensitivity and exclude noise sources, more elaborate schemes for atom interferometry have been developed, such as using multiple atom interferometers for differential measurements of counter-propagating atom beams for common mode rejection [55, 56].

To improve the coherence, it is worth looking at ultracold atoms, but first we need some disclaimers. The topic of coherence in atoms is not always well defined. From our point of view (in the context of atom interferometry experiments), only the visibility of the interference fringes (i.e. the fringe contrast) is of prime importance, which depends on the *spatial coherence* of a wavepacket. The spatial coherence refers to the length scale over which a defined phase relation exists over the atomic wavpacket.

In this context, the *coherence time* refers to the time over which the wavepacket keeps its fixed phase relation. The spatial coherence decays with time due to atom collisions and interaction with light, and the phase becomes more random [35]. The coherence time is therefore the "decay time" of the spatial coherence. For a BEC, it is measured via the decay of the interference visibility to be around 100 ms [57]. We expect the coherence time to depend on the momentum spread of the atoms, and it is said to behave as $\propto (\Delta v)^{-1}$ [8]. A large spatial coherence together with a long coherence time to maintain good visibility is desirable. Using

cold, or even degenerate atoms could provide the means for maintaining coherence over longer measurement times. It is therefore worthwhile to take a closer look at degenerate gases in atom interferometry, and the next Section introduces some important points.

1.4.4 Cold atoms in atom interferometry?

The potential that atom interferometry has to offer is very convincing, but what are the advantages of using cold instead of hot atoms, and do we want to use a BEC or even degenerate Fermi gas? It is not an easy question. The main reason to use cold atoms over hot atoms lies in their coherence. For clouds with smaller momentum spread, the coherence time is longer, which means longer interaction times and thus better phase sensitivity. The transition to the use of BEC interferometry can be compared to using a laser in light interferometry – as opposed to white light – where all interfering particles are in the same mode [58]. Making a BEC, on the other hand, means a sacrifice in atom number, thereby reducing sensitivity. Another disadvantage is that atomic interactions in a BEC cause phase shifts [50], which counteract an improvement of the atom interferometer precision. This is less of a problem for fermions: atoms in a degenerate Fermi gas (DFG) lack interaction, because they avoid occupying the same space when they are in the same quantum state, due to the Pauli exclusion principle. Using fermions instead of bosons brings other problems instead.

Whether it is more useful or not to make the transition from using cold atoms to using degenerate quantum gases for atom interferometry, it does open the door to unique techniques, such as squeezing [58] or tuning of the scattering length to reduce the interaction [12]. We prepare our experiment to be able to use both atomic species (bosonic ^{87}Rb and fermionic ^{40}K), which should allow for a comparison of measurement results from atom interferometry with BEC and DFG. An additional advantage of trapping ultracold atoms in a BEC in our ring trap lies in its use as probe, to characterise the ring trap with regard to its smoothness. Because the properties of BEC and DFG influenced our decisions on experimental design and setup and play a key part in atom interferometry in general, we will now look at both atomic species in a bit more detail.

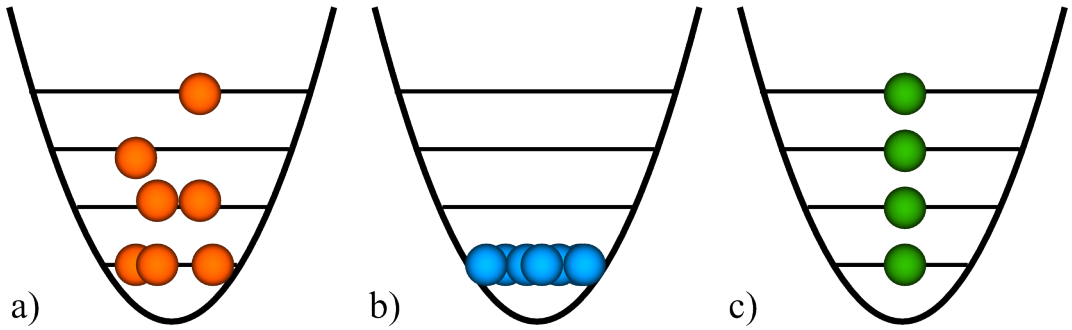

Figure 1.8: Illustration of atoms in a potential, occupying different energy levels: (a) thermal atoms, (b) bosons in the ground state in a BEC and (c) fermions in their lowest state, defined by the Pauli exclusion principle. The energy level spacing and their occupation are not realistic but only an illustration; thermal atoms see a quasi-continuum if their temperature is large compared to the energy level separation [36].

1.4.4.1 Bosons and fermions

Depending on their spin and on the symmetry of their atomic wavefunction, there are two kinds of particles, which have recognisably different properties when the atoms are very cold: bosons have integer spin and symmetric wavefunctions under exchange of (indistinguishable) particles. Fermions have half integer spin and an antisymmetric wavefunction under exchange of (indistinguishable) particles [36]. The Pauli exclusion principle follows for fermions from the antisymmetric wavefunction, as the combined wavefunction for multiple fermionic particles goes to zero if the distance between the particles goes to zero [59]. This is reflected in the different atom distributions over energy levels for bosons and fermions (only for low temperatures, they both approach a Maxwell-Boltzmann distribution for high temperatures). For temperatures below a critical temperature (see below), bosons form a Bose-Einstein condensate (BEC) and fermions form a degenerate Fermi gas (DFG). An illustration of the lowest possible states for bosons and fermions is shown in Figure 1.8. The different energy level occupation has important implications for a cold atomic wavepacket, such as in an atom interferometer: because all atoms are allowed to be in the same state, a BEC has a very narrow momentum distribution. For fermions in a DFG, the fermions all occupy different momentum states and a DFG therefore has a broader momentum distribution.

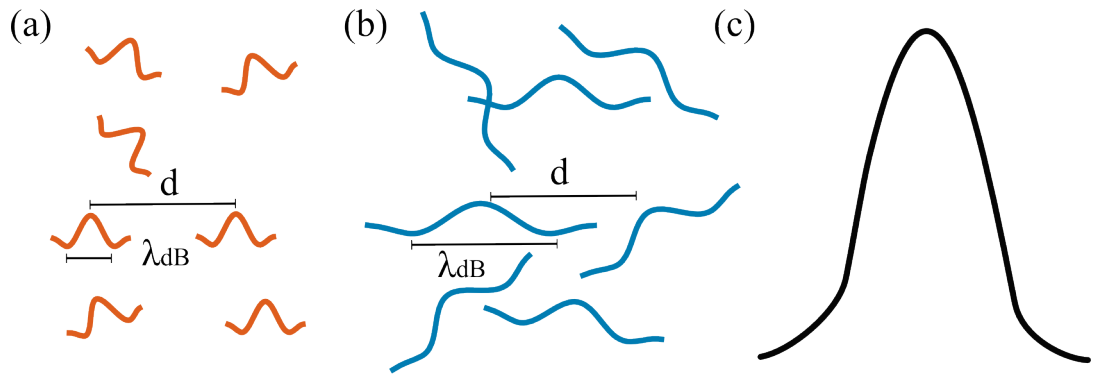

Figure 1.9: De Broglie waves: (a) thermal atoms have a de Broglie wavelength, λ_{dB}, smaller than the interparticle spacing, d. (b) Close to the transition temperature, T_C, the two scales become comparable. (c) A perfect BEC can be described by a single wavefunction. Figure adapted from [60].

BEC A gas of bosonic atoms can make the transition from a "saturated" gas to a "condensed" gas (BEC). A gas is saturated when it has reached the maximum number of atoms that it can accommodate in the excited energy levels without changing its temperature or volume, and additional atoms need to occupy the ground state (see [35]). By reducing the temperature, the maximum atom number decreases, until the transition to BEC occurs at the critical temperature, T_C [35, 36]:

$$T_C = \frac{2\pi}{[\zeta(3/2)]^{2/3}} \frac{\hbar^2 n^{2/3}}{m\ k_B}\ , \tag{1.14}$$

with the particle mass, m, the atom density ($n = N/V$) and the Riemann zeta function $\zeta(3/2)$. Note that this equation is for a gas in a 3D box and needs modification when the atoms are in a different potential (e.g. in a three-dimensional, isotropic harmonic trap with angular trapping frequency ω_0, the critical temperature is $T_C \approx 0.94 \frac{\hbar\omega_0 N^{1/3}}{k_B}$ [35]). The particle size is also helpful for understanding BEC, which in a gas with temperature T is described by the de Broglie wavelength:

$$\lambda_{\mathrm{dB}} = \sqrt{\frac{2\pi\hbar^2}{mk_BT}}\ . \tag{1.15}$$

When a gas makes the phase transition to a BEC, then λ_{dB} is of the order of the mean distance between the atoms, so that the atoms' wavefunctions are spatially

overlapping (as illustrated in Figure 1.9). This is expressed in the relation between the critical temperature and the thermal de Broglie wavelength, which is called the *phase-space density*:

$$PSD = n\lambda_{\mathrm{dB}}^3(T) \ , \tag{1.16}$$

At the transition to BEC, it is $PSD_C = n\lambda_{\mathrm{dB}}^3(T_C) = \zeta(3/2) \approx 2.6$ [35]. This shows that it is not only important to reduce the temperature, but also to keep the atom number density high. The fraction of atoms in the condensed state increases with decreasing temperature, and at absolute zero, the gas would be purely in the ground state. The narrow momentum distribution of a BEC produces a characteristic (non-Gaussian) spatial distribution after releasing the BEC from the trap, which can be used to identify the transition for a cold cloud of atoms to degeneracy (as e.g. in [61]).

BECs were first realised with ^{87}Rb atoms at $T_C \approx 170$ nK by the group of Cornell and Wieman [61] and with Na atoms at $T_C \approx 2$ μK by the group of Ketterle [62]. For a review of this topic, see e.g. [34, 35], for an experimental approach see [60].

DFG The simplification that all atoms in a BEC are in the same state without any interaction is not valid in reality, instead the total energy of a BEC is $E_{\mathrm{kin}} + E_{\mathrm{pot}} + E_{\mathrm{int}}$. It is this interaction, which causes a decoherence in the atomic wavepacket over time. This effect has been studied theoretically by Jamison et al. [63] for the experiment from Gupta et al. [8]. Although interactions don't prevent a high interferometer precision, alternatives are explored by using fermions for interferometry [64, 65, 66].

Fermions can not occupy the same state due to the Pauli exclusion principle. Instead, for an atomic gas with N atoms, the energy level occupation reduces down to the lowest N energy levels with decreasing temperature, see Figure 1.8. The highest energy level occupied at absolute zero is the Fermi energy, E_F, which depends on the atom number, N, and the energy levels in the potential. The Fermi temperature is defined by the Fermi energy [67]:

$$T_F = E_F/k_B \ , \tag{1.17}$$

and degeneracy is observed when $T/T_F \approx 1$. For fermions, the transition to degeneracy shows in emerging quantum properties of the gas, such as non-classical momentum distribution [67, 68]. A degenerate Fermi gas with ^{40}K atoms at $T_F \approx$ 600 nK was created by DeMarco and Jin [68]. A review with an experimental focus can be found in [69].

Although the lack of interaction is a useful property with respect to the coherence, it has the disadvantage that the cooling process is less effective as the atoms don't re-thermalise as easily (in fact, if they were all in the same internal state, they would not re-thermalise at all at low energies). One approach is to combine the advantages of both species so that bosons can be used to cool fermions: by mixing both species, the bosons collide with the fermions and kinetic energy is transferred. The fermionic atoms re-thermalise with the help of the bosons as a buffer gas ("sympathetic cooling", see e.g. [70]). Our experiment aims to start with interferometry using a BEC of ^{87}Rb atoms, but the addition of ^{40}K is considered for interferometry with a DFG, and the atom source and the optical setup account for that.

Now that we have discussed the atoms and some of their properties, the following Sections focuses on toroidal trapping geometries and how atoms are confined.

1.5 Toroidal atom traps

For atom interferometry, the features of toroidal traps are of advantage: ring traps provide symmetric, two-dimensional confinement with periodic boundary conditions. The trap acts as a circular waveguide, guiding the atoms back to their initial position, so that only the splitting and re-combination pulse are necessary. For atoms propagating in opposite directions around the ring, the two paths also have common mode rejection (like a dual atom-interferometer, as e.g. [56]). Having guided paths in a toroidal atom interferometer also reduces phase noise due to the Coriolis force, e.g. in gravity measurements [71, 72]. The biggest advantage for Sagnac interferometry comes from the enclosed area: free-propagating atom interferometers generally use momentum transfer from standing light waves not only to split the atoms, but also to spatially separate them.

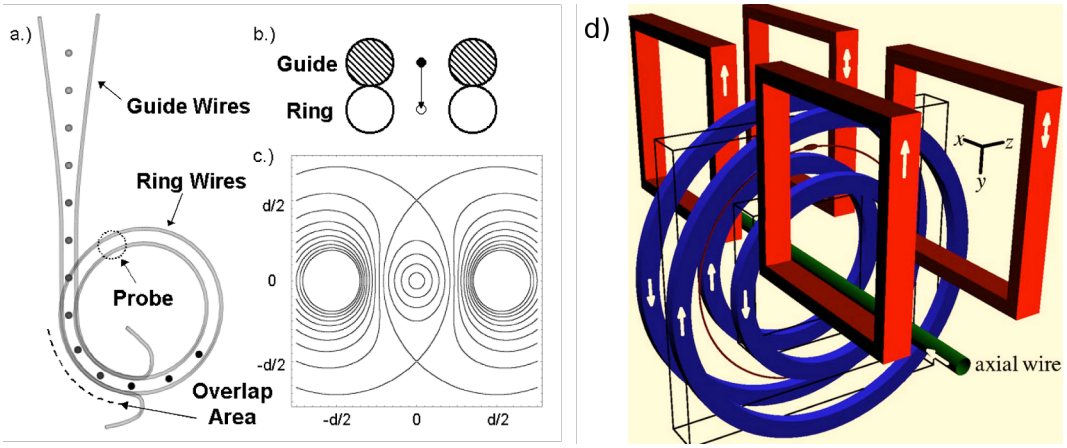

Figure 1.10: Two examples of magnetic ring traps: (a)-(c) are taken from [80] and show the ring trap created from the magnetic fields from two circular wires with DC current in the same direction. (d) is taken from [81] and shows the four circular wires that create a quadrupole field with a ring-shaped magnetic minimum.

The resulting separation is limited, e.g. for a typical momentum transfer of $2k_L$ it is $s = t_{\text{int}} 2\hbar k_L/m \approx 1$ mm for ^{87}Rb with $t_{\text{int}} = 100$ ms. To increase sensitivity, the paths are made long (~ 1 m, e.g. [33]), but the large size of the setup is a disadvantage. Large enclosed areas with compact spatial extend can be achieved by using guided interferometers [54, 73], where the atoms are confined during propagation along the paths – as in a ring trap. Note that work also goes into maximising the photon momentum transfer to increase the spatial separation in free space interferometers [74, 75], at the time of writing, the maximum transferable photon momentum is 102 $\hbar k$ [75].

With ring traps that are small enough to be filled completely by the atoms, the superfluid properties of a BEC can be studied [76, 77]. Work on superfluidity includes vortex creation and decay [3, 76] and atomic SQUIDs [78]. Small traps also enable the imitation of situations and environments that are otherwise difficult to study, such as the sonic equivalent to black holes [79]. The quasi one-dimensionality of a tight ring trap is then of advantage, as the motion in two dimensions is restricted (for a ring axially aligned on z, in cylindrical coordinates: z and r motion is harmonically constrained, and dynamics and propagation of atoms only occurs azimuthally, along ϕ, for sufficiently tight traps).

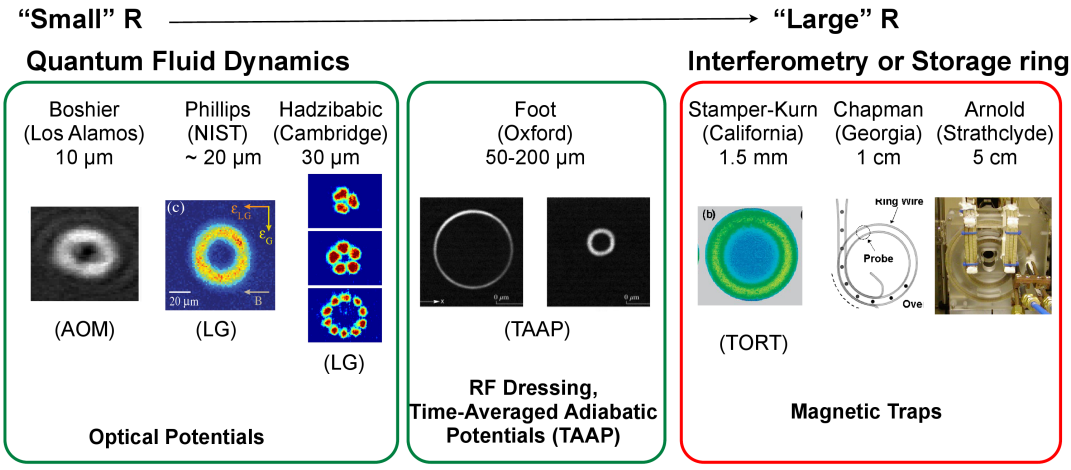

Figure 1.11: Examples of ring traps around the world, created with different methods: small traps ($\sim \mu$m) can be used for superfluid investigation, and large traps (mm-cm) are most suitable as storage rings and atom interferometry. While small rings are mainly made with optical potentials, large rings tend to be created with magnetic fields. Versatile traps with intermediate, tunable radius are produced with RF-dressed states. Our ring trap is a magnetic trap with a radius of the order of several mm.

Ring traps for atoms can be developed using magnetic fields, light, or a combination of both. Small scale traps tend to be created with light, while magnetic fields are mostly used for macroscopic ring traps. The stability and homogeneity over large scales and the readily available large scale coils with which the magnetic trapping fields can be created, make larger traps accessible with magnetic fields. Light, on the other hand, can be focused and shaped on the wavelength scale, providing a very flexible tool for atom trapping on a smaller scale. Because ring traps are so versatile and unique, a large number of research groups work on creating ring traps for neutral atoms, some of which are already successfully employed. This Section aims to give an impression of the different methods for the creation of ring traps. Only the basic working principles are described in order to show the variety of methods explored, please refer to the references for details. An overview is also given in Table 1.1.

Magnetic ring traps The first ring trap for neutral atoms was a magnetic trap, developed by the Chapman group [80]: wires form two concentric circles of different radius, with equal DC current in the same direction. The fields oppose each other in the region between the wires and cancel in a ring, as shown in Figure 1.10 (a). The resulting trap has a radius of 2 cm and a trap depth of 2.5 mK. Majorana spin-flips at the magnetic zero point are suspected to cause atom loss, and the authors in [80] recommend adding an axial wire to create an azimuthal field. This has been implemented in the purely magnetic trap from Arnold [81], where four coils with DC currents form a "ring-shaped quadrupole". The magnetic minimum creates a ring with a radius of 4.8 cm, as shown in Figure 1.10 (d). Here, a central wire along the axis of the coils prevents Majorana losses. Arnold's large magnetic storage ring is also at Strathclyde, next to our experiment. Apart from having been an inspiration for the inductively coupled magnetic ring trap, much of the work on the two experiments is done in parallel.

An alternative idea to circumvent spin-flip losses is the time-orbiting ring trap (TORT) [82] (similar to a time orbiting potential (TOP) trap, discussed in Section 2.1.1). The group of Stamper-Kurn has realised this by creating magnetic field, in which a ring of magnetic zeroes rotates with a frequency of 5 kHz, thereby creating a non-zero, time averaged magnetic minimum with an adjustable radius of 0.6 to 1.5 mm [83].

Magnetic and optical potentials can also be combined to form the desired trapping geometry: in [76], a harmonic magnetic trapping potential and a repulsive potential from blue-detuned light in the centre are superimposed to create a ring trap with a radius $\gtrsim 8$ μm around the beam, in which BEC can be captured.

Optical ring traps An all-optical, toroidal atom trap can be obtained by shaping the intensity distribution of light spatially, to trap atoms in either the maximum (red-detuned) or the minimum (blue-detuned) intensity-regions. The laser beam intensity can be modified in a number of ways.

A BEC has been successfully trapped in a high intensity optical ring trap at the intersection of a light sheet and a (hollow) Laguerre-Gaussian (LG) beam, with a radius of ~ 20 μm by the group of Phillips and Campbell [78]. Here, the small toroidal trapping geometry is employed for studying superflow in BEC;

vortices are induced and the effect of adding a barrier to the system is studied. The same method (LG beam plus light sheet) is also applied by the group of Hadzibabic [3, 77], who induce vortices in superfluid BEC, and the angular momentum of the vortex is studied using interferometry in the ring [3]. Another great application for this kind of trap is the acoustic interferometer by the group of Stamper-Kurn [4]: similar to the LG beam method, the overlap of a red-detuned and a smaller blue-detuned beam form a repulsive potential in the centre and a potential minimum at the outside edge of the beam. Overlapped with a light sheet, a toroidal trap with a radius of 16 μm is formed, and ^{87}Rb atoms are trapped. The atoms are then evaporated in the ring potential to degeneracy, and the BEC is used for rotational sensing by "collective excitation interferometry" [4], using standing sound waves in the BEC.

In analogy to an "optical TOP trap", arbitrary trapping geometries can be painted onto a light sheet, using a focused, red-detuned laser beam ("optical tweezers") as a brush. By rapidly scanning the beam, toroids with radii of 25 μm and 10 μm (amongst other shapes) have been created and shown to trap BECs [84]. Not only that, the potentials can be changed dynamically: a BEC can be trapped in a toroid, which is then adiabatically transformed into a ring lattice and back to a toroid.

Also explored are the use of a spatial light modulator that is feedback coupled to an intensity-monitoring CCD camera to shape the beam intensity [85], to overlap Laguerre-Gauss beams with different angular momentum so as to create a toroidal intensity maximum of the order of 80 μm [86] or to manipulate beam deflection angle and power with an AOM in two dimensions and scan the beam, creating a ring with a radius of 44 μm [87]. However, these methods have not yet trapped atoms. Other proposals for new trapping geometries – including ring lattices – obtained from the superposition of Laguerre-Gaussian beams with different orders can be found in [88].

RF dressed ring traps New ways of forming flexible trapping potentials emerged with the use of radio frequency (RF) dressed states, as first proposed by Garraway [89]. In RF dressing, new eigenstates are created for the combined system of an atom and a photon. By exposing a magnetic QP trap to RF radiation,

the magnetic sub-levels are coupled, and due to the resulting avoided crossings of the dressed states, a shell-like potential minimum is then formed. RF dressed state ring traps were first realised by the Foot group: within the shell potential, atoms are confined to a ring, either with two blue-detuned light sheets, resulting in a ring with tunable radius ($0 - 85$ μm) [90], or by using a time averaged adiabatic potential (TAAP [91]) where an axial, oscillating magnetic field creates a ring trap (tunable radius of $50 - 250$ μm) [92]. It has also been proposed to combine RF dressed states with optical standing waves, in order to create adjustable ring traps [93].

Radius	Method	Atoms	Source
4.8 cm	magnetic	^{87}Rb BEC	[81]
2 cm	magnetic	^{87}Rb	[80]
$0.6 - 1.5$ mm (tunable)	magnetic	^{87}Rb BEC	[83]
$50 - 250$ μm (tunable)	RF dressing + magnetic	^{87}Rb BEC	[92]
$0 - 85$ μm (tunable)	RF dressing + optical	^{87}Rb BEC	[90]
20 μm	optical	^{23}Na BEC	[78]
16 μm	optical	^{87}Rb BEC	[4]
10 μm, 25 μm (tunable)	optical	^{87}Rb BEC	[84]
$8 - 30$ μm (tunable)	optical	^{87}Rb BEC	[3]
$\gtrsim 8$ μm	magnetic + optical	^{23}Na BEC	[76]

Table 1.1: Examples of atomic ring traps of different sizes using various methods.

Inductively coupled magnetic ring trap Our ring trap is a purely magnetic trap with a size of 5.3 mm (ring 1) and 1.8 mm (ring 2), with which it adds to the range of available sizes (compare Figure 1.11 and Table 1.1). It is based on the same principle as the ring traps in Figure 1.10 in that it creates a minimum position in a "quadrupole-ring" by superposition of opposing magnetic fields. It also incorporates aspects of the TORT trap [82, 83] by moving the magnetic zeroes to create a time-averaged magnetic minimum. However, the main difference to all these is that the magnetic minimum is not created by sets of current carrying looped wires with DC currents, instead one conducting loop carries current that is induced by an external AC magnetic field from a set of Helmholtz coils. The next Chapter describes the creation of our ring trap and its expected trap properties in more details.

Chapter 2

Ring trap theory

As introduced in the previous Chapter, ring traps for cold atoms have various potential applications, the size of the trap bringing out different advantages of the ring shaped trapping potential. As a storage device for cold atoms, it allows us to study e.g. the interaction between different species of atoms and manipulation of Bose-Einstein condensates (BEC) and degenerate Fermi-gases (DFG). Large ring traps are also ideal for atom interferometry, especially rotational measurements, while small ring traps have a suitable geometry for studying persistent currents, as the atoms can fill out small rings completely and form a multiply connected BEC. The development of ring traps on a variety of scales for a variety of applications, as shown in the previous Chapter, try to take full advantage of the properties of this geometry.

In this Chapter, we discuss the trapping potential of our ring trap in greater detail. The trap is specifically built to work for cold ^{87}Rb atoms, but the use with any other magnetically trappable atomic species is possible. For future experiments with fermions, the addition of ^{40}K has been considered and is accounted for in the experiment's layout. If other experiments require a different layout or orientation, the setup for the trap itself (i.e. coils and copper ring) can be modified to fit, but the atom sample preparation and trap loading may need to be re-designed. The trap is scalable, which we make use of in the transition from the first to the second generation experiment.

To better understand the mechanism of our ring trap, the following Section briefly recalls the relevant concepts of magnetic atom trapping.

2.1 Magnetic trapping

Magnetic trapping makes use of the fact that the energy of atoms in an external magnetic field, $\vec{B}$, scales with the magnetic field, see e.g. [37]:

$$E = -\vec{\mu} \cdot \vec{B} \ . \tag{2.1}$$

The scaling depends on the orientation of the atomic magnetic moment, $\vec{\mu}$, relative to the field, which is different for the magnetic sub-levels (m_F-levels). With static magnetic fields, we can only trap low-field seeking atoms, i.e. atoms in those m_F states for which the potential energy *increases* with magnetic field:

$$U_B = g_F m_F \mu_B |\vec{B}| \ , \tag{2.2}$$

with $g_F m_F > 0$. High-field seeking atoms can not be trapped, because there can not be any local field maxima in a charge free space [94, 95], as stated by the Earshaw theorem (also expressed in Maxwell's equation $\nabla \vec{B} = 0$).

For low field seeking atoms, on the other hand, we can generate a potential minimum by locally minimising the *magnitude* of a non-uniform magnetic field. The trap depth depends on the field strength, and the steepness of the trap depends on the field gradient, as the force acts on the atoms with $\vec{F} = -g_F m_F \mu_B \nabla B$. This force causes the atoms to move (or "orbit" [96]) in trajectories close to the centre (see e.g. [34]). The first atoms were magnetically trapped by the group of Philips [96] with laser cooled atoms, which is necessary due to the weak confinement for neutral atoms (especially in comparison with charged particles). In [96], the atoms are trapped in a spherical quadrupole (QP) trap, which is created by two coils in anti-Helmholtz configuration:

$$\vec{B}_{QP} = (B_{QP} \cdot x, B_{QP} \cdot y, -2B_{QP} \cdot z), \tag{2.3}$$

with $\vec{z}$ being the symmetry axis of the field producing coils. The field has a zero point at the axial and radial centre of the coils and a gradient that increases linearly with radius.

Adiabaticity The confinement depends on the atoms staying in the low-field seeking state, otherwise the trapping potential becomes anti-trapping and the atoms are expelled. To stay in the trapped state, the magnetic moment must be able to follow the magnetic field lines and keep the projection constant. The ability to do so depends on the Larmor frequency, ω_L, with which the atom's magnetic moment precesses around an external magnetic field:

$$\omega_L = g_F m_F \mu_B |\vec{B}|/\hbar \ . \tag{2.4}$$

It also depends on how fast the magnetic field changes, which must be slow compared to ω_L:

$$\mathrm{d}\Theta/\mathrm{dt} < \omega_\mathrm{L} \ , \tag{2.5}$$

where

$$\mathrm{d}\Theta/\mathrm{d}t = \frac{|\mathrm{d}\vec{B}/\mathrm{d}t \times \vec{B}|}{|\vec{B}|^2} \tag{2.6}$$

is the normalised change of the magnetic field. If the atoms in a magnetic field don't spin-flip (i.e. don't change their m_F-state), they are said to follow the magnetic field "adiabatically" [36].

Towards the centre of the trap, the magnetic field vanishes and the adiabatic condition is not fulfilled, and atoms can then spin flip out of the trap. These "Majorana losses" are relevant for every magnetic trap with magnetic zero points – including our ring trap. In a QP trap (with z being the symmetry-axis), the Majorana loss rate is found to be:

$$\Gamma_M = C\frac{\hbar}{m}\left(\frac{\mu \mathrm{dB/dz}}{k_B T}\right)^2 \ , \tag{2.7}$$

with a scaling factor C of the order of unity (see [97]). For a given atomic species, the Majorana losses then depend on the magnetic field gradient and the temperature. In a QP, it is cold atoms that are most affected by spin-flips, as low energy atoms spend more time close to the non-adiabatic centre of the trap.

To avoid spin-flips, potentials without magnetic zeroes can be created: a QP field can be modified, e.g. by adding an axial offset field, B_off, which makes the bottom of the trap round, as described in [34]. By approximating the trap-

ping potential to be parabolic at the trap bottom, the atom's movement can be described as an harmonic oscillation, which leads to the definition of the trap frequency, ω_r (here: radial trap frequency, taken from [34]):

$$V(r) = V_0 + \frac{1}{2} m\omega_r^2 r^2 \ , \tag{2.8}$$

with $\omega_r = \sqrt{\frac{g_F m_F \mu_B}{m B_{\text{off}}}} \frac{\text{dB}}{\text{dr}}$. Alternatively, the addition of a repulsive potential from blue-detuned light can provide a "plug" for Majorana losses at the bottom of the QP trap [97]. Optical trapping becomes important at a later stage (for evaporation in the second generation ring experiment, see Section 6.1.2), but we now focus on purely magnetic trapping. Important for us is the method of time-varying magnetic fields for the creation of time-averaged trapping potentials, which can have adiabatic, non-zero regions near the trap minimum.

2.1.1 Time averaged traps

Time-dependent magnetic fields, $B(\vec{r}, t)$, that vary with a frequency ω_F can be used to create a time-averaged trapping potential with a minimum [98]:

$$\langle U_B \rangle_t = \frac{\omega_F}{2\pi} \int_0^{2\pi/\omega_F} U(t)\text{dt} \neq 0 \ . \tag{2.9}$$

By choosing $U_B(t)$ such that there are no magnetic zeroes at the potential minimum, Majorana losses can be reduced. Such a time-averaged orbital potential (TOP) trap for atoms was first demonstrated by the group of Cornell [98], where a rotating, horizontal bias field is added to a spherical QP. This produces a magnetic QP field in which the zeroes orbit around the atom cloud, resulting in a non-zero time-averaged magnetic field minimum. It is important to note that Majorana losses can be reduced with this method, but they don't disappear: atoms with enough energy to move close to the orbiting zeroes still have a probability to spin flip and be lost [98]. However, in traps for cold atom experiments it better to lose high energy atoms due to spin flips than low energy atoms.

When using time-varying fields, it is important to choose the right frequency for ω_F: the atoms have a motional frequency, ω_A ($\sim$ 100 Hz in [98], equivalent to the trap frequency when harmonic), while their magnetic moment is precessing around the field axis with ω_L ($\sim$ 7 MHz in [98]). To create a time-averaged trap, the frequency of the time-varying magnetic field must be fast enough so that the atoms can not spatially follow, but slow enough to allow the atomic magnetic moment to follow (see e.g. [98]). This is expressed in the condition:

$$\omega_L > \omega_F > \omega_A \ . \tag{2.10}$$

The application of the TOP trap principle in combination with other than the pure QP trap can also produces more complex trapping geometries, such as the time-orbiting ring trap (TORT) [82, 83] that was introduced in Section 1.5. Common to TORT-like traps is the "torus of death": similar to a magnetic zero point that orbits the time-averaged magnetic minimum in a TOP trap, a ring of magnetic zeroes oscillates around the time-averaged minimum in a TORT trap. Equivalently, atoms with large enough kinetic energy may still move close enough to the non-adiabatic regime near the magnetic zeroes and spin-flip out of the trap.

For our ring trap, we employ a combination of time-varying fields that produce a time-averaged trapping potential and a static field to offset the magnetic zeroes and create a safe, adiabatic region for the atoms near the trap minimum. With above concepts in mind, we now discuss the magnetic field and the resulting trapping potential for the inductively coupled magnetic ring trap.

2.2 The inductively coupled magnetic ring trap

The inductively coupled ring trap is created by the superposition of opposing magnetic fields, which results in a magnetic minimum. We can understand the potential better if we unfold the ring and start by looking at the magnetic field from a straight wire.

When a wire carries a constant current, I (constant current along z), a magnetic field is produced around the wire, according to Ampère's law (electrostatic

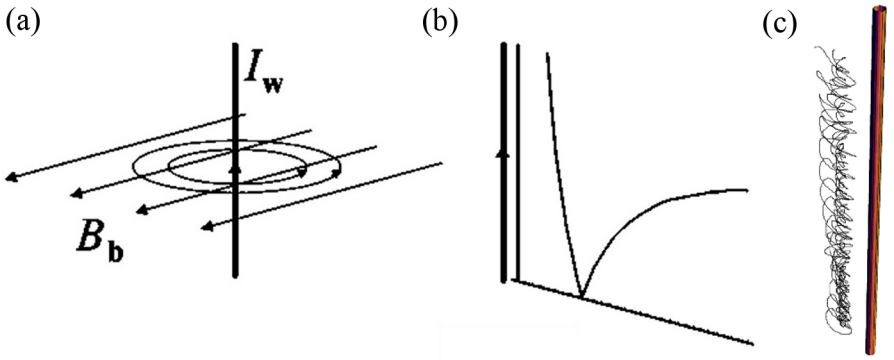

Figure 2.1: The magnetic field from a wire can be used to guide atoms in a 2D trap by adding a bias. Here, (a) shows the magnetic fields, (b) the radial potential and (c) probable positions for the atoms in a line close to the wire. Images (a) and (b) taken from [100], (c) taken from [99].

case):

$$\nabla \times \vec{B} = \mu_0 \vec{j} \ , \tag{2.11}$$

where μ_0 is the magnetic permeability and $\vec{j}$ is the current density. The field, $\vec{B}(r, z, \phi)$, is symmetric along z and ϕ, but it falls off radially:

$$B(r) = \frac{\mu_0}{2\pi} \frac{I}{r} \ . \tag{2.12}$$

So far, there is no potential minimum and no trap yet. But when a bias field, B_b, is added then the magnetic field cancels at one radial position, namely where $B(r) = B_b$ [99]. This produces a line of magnetic zeroes, parallel to the wire, which can be used as a guide for atoms, as has been recognised by the group of Schmiedmayer [99]. Figure 2.1 shows a schematic of the magnetic fields and the resulting atom guide geometry for the atom guide experiment (taken from [99, 100]). Majorana losses at the zero points (introduced in the previous section) are also addressed: to offset the magnetic zero and create a magnetic minimum with $B \neq 0$, a bias field *along* the direction of the wire can be added [101].

To get from this linear atom guide to a toroidal atom trap, we bend the straight wire, keeping the guiding potential on the inside, so that the closed conducting loop forms a closed, ring shaped guide, i.e. a ring trap.

However, with a closed conductor we do have the problem that there are no

wire ends anymore where the voltage can be applied to generate the current. We don't want to cut the ring to attach wires, because it would destroy the symmetry of the current along the wire and thus of the trapping potential. Fortunately, currents not only create magnetic fields, but magnetic fields also create currents: a changing magnetic flux through a surface enclosed by a conductor induces a voltage (electromotive force), resulting in a current in the conductor (Faraday's law).

This means that we now need a time-varying magnetic field to induce the current, plus the bias field to produce the magnetic zero line at the (inner) edge of the looped conductor. Here, the *direction* of the induced current is in our favour, as it is such that the induced current produces a magnetic field *opposing* the field that causes the current. As a result, at each point of the magnetic field cycle, the two fields oppose each other to cancel in the ring. We create the ring of magnetic zeroes with a time-varying bias field and a single, looped conductor.

With the ring-shaped magnetic zeroes, we now need to find a way to reduce Majorana losses. We can't apply a bias along the wire direction as easily as for the straight conductor. One solution is to add a current carrying wire through the centre of the loop, to produce an azimuthal offset field at r_0 [81], but the wire is an obstacle that reduces optical access in the vicinity of the ring and requires a special vacuum chamber. To avoid these complications, we add an offset bias field along the z-axis.

In our trap, we create a magnetic minimum to trap low-field seeking atoms. Because we are using time-varying fields with large enough frequencies, the trapping potential is the result the time-average (similar to the TOP trap). At each point through the cycle, we have a superposition of several magnetic fields:

1. AC drive field: $\vec{B}_{\text{drive}}$;
2. The secondary AC magnetic field, coming from the induced current in the closed, conducting loop: $\vec{B}_{\text{ind}}$;
3. DC field to offset the magnetic zeroes: $\vec{B}_{\text{DC}}$.

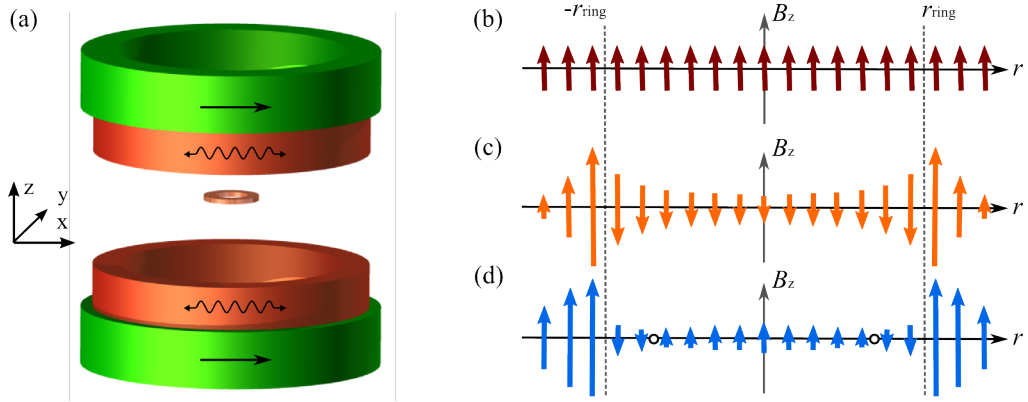

Figure 2.2: (a) Schematic of the Helmholtz coils that produce the AC drive field (red) and the bias coils (green) with the copper ring in the centre. The AC drive field (b) and the field from the induced current in the copper ring (c) are in a superposition to form an effective magnetic field (d) at a given point in time.

Here, the AC drive field acts to firstly induce a current in the ring and secondly to provide the bias field that cancels with $\vec{B}_{\text{ind}}$ from the conducting loop at a position r_0.

The following Sections go into more detail regarding the magnetic fields that are involved in creating the ring trap and the resulting trapping potentials. The theory of our trap is also described in [1, 2].

2.2.1 Drive and secondary magnetic field

Let's have a look at the electric and magnetic fields: the AC drive field is provided from a set of Helmholtz coils, and the conducting loop is a copper ring placed at the centre of the coils, see Figure 2.2. This makes the heart of the experiment. With the axes of the coils and the copper ring aligned along z, the AC drive field is cylindrically symmetric along the z-axis. It is

$$\vec{B}_{\text{drive}}(t) = B_0 \cos(\omega t)\hat{e}_z \ , \tag{2.13}$$

where B_0 is the amplitude of the AC drive field and $\omega = 2\pi f$ is the angular frequency, with f of the order of tens of kHz. We apply an external AC magnetic field with the drive coils with an amplitude of $B_0 \approx 50$ G. In the first instance,

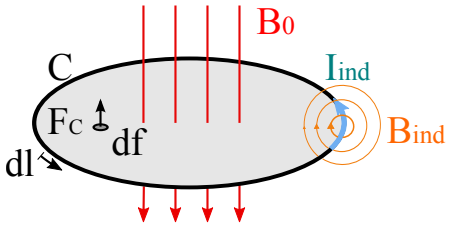

Figure 2.3: Schematic of a conducting loop, C, where the changing flux of an external magnetic field through the enclosed area F_C induces a current, I_{ind}, in the conductor.

we simply regard the flux through the copper ring as the flux through a closed loop C of radius r_{ring}, enclosing the surface $F_C = \pi r_{\text{ring}}^2$:

$$\Phi_B = \int_{F_C} \vec{B} \cdot \mathrm{d}\vec{f}\,, \tag{2.14}$$

where $\mathrm{d}\vec{f}$ are the elements of surface F_C [102], see Figure 2.3 for a schematic.

A changing magnetic flux induces an electric field, $\vec{E}_{\text{ind}}$, in the copper ring, according to Faraday's law. The line integral along C of the electric field is the electromotive force (EMF) [102] here denoted by U_{EMF}:

$$U_{\text{EMF}} = \oint_C \vec{E}_{\text{ind}} \cdot \mathrm{d}\vec{l}, \tag{2.15}$$

where $\mathrm{d}\vec{l}$ is the vector element of the loop C.

U_{EMF} causes a current $\vec{I}_{\text{ind}}$, which is directed in such a way that it produces a magnetic field opposing the first one, according to Lenz's law [102]:

$$U_{\text{EMF}} = -\frac{\mathrm{d}\Phi_{\text{B}}}{\mathrm{dt}}\ . \tag{2.16}$$

The copper ring has a resistance, R_{ring}, and an inductance, L_{ring}, so that the relationship between the induced current and the induced voltage is that for a RL-circuit [102]:

$$U_{\text{EMF}} = L_{\text{ring}} \frac{\mathrm{d}I_{\text{ind}}}{\mathrm{dt}} + I_{\text{ind}} R_{\text{ring}}\ . \tag{2.17}$$

From Equations 2.13 and 2.16, we know that the current has the form $I_{\text{ind}} = I_0 \cdot$

$\cos(\omega t + \delta_0)$. The current propagates along the direction of the looped conductor, $\hat{e}_\phi$. We find I_0 via the EMF amplitude, U_0, and the impedance, $Z = R + i\omega L$ [102]:

$$I_0 = \frac{U_0}{|Z|} \tag{2.18}$$

$$= \frac{-\omega B_0 \pi r_{\text{ring}}^2}{\sqrt{R_{\text{ring}}^2 + \omega^2 L_{\text{Ring}}^2}} \, . \tag{2.19}$$

We rewrite this equation to get

$$I_{\text{ind}} = -\frac{I_{\text{max}}}{\sqrt{1+\Omega^{-2}}} \cdot \cos(\omega t + \delta_0) \, , \tag{2.20}$$

with $I_{\text{max}} = \frac{B_0 \pi r_{\text{ring}}^2}{L}$ and the unitless frequency dependent term $\Omega = \frac{\omega L_{\text{Ring}}}{R_{\text{Ring}}}$. The phase shift is $\delta_0 = \tan^{-1}(1/\Omega)$. This notation is chosen to be consistent with [1, 2], see Appendix A for details.

In the first generation ring experiment, we have $\Omega \approx 18$, and with $\tan^{-1}(x)$ approaching 0 for small x, we get $\delta_0 \approx 0$. The induced current produces the secondary magnetic field, $\vec{B}_{\text{ind}}(t)$, which is in phase with $\vec{I}_{\text{ind}}(t)$. This leaves us with the maximum phase lag of $\vec{B}_{\text{ind}}$ with respect to $\vec{B}_{\text{drive}}$, the fields have a phase of $\sim \pi$ (a larger δ_0 decreases the phase lag). Figure 2.4 (a) shows the value for δ_0 as a function of Ω. Also shown, in Figure 2.4 (b), is the dependence of the current amplitude, I_0, as a function of Ω. This shows how well the inductor couples to the AC field at a given frequency. Indicated are the values for ring 1 (first generation experiment) and ring 2 (second generation experiment). In both cases, the current reaches about its maximum value (the AC frequency and ring properties were matched to do so) and the phase lag is close to π (i.e. δ_0 is small).

From the induced current we can now obtain the secondary magnetic field, $\vec{B}_{\text{ind}}$. The off-axis magnetic field (z and $r \neq 0$) of a looped conductor can be solved using elliptic integrals [103]:

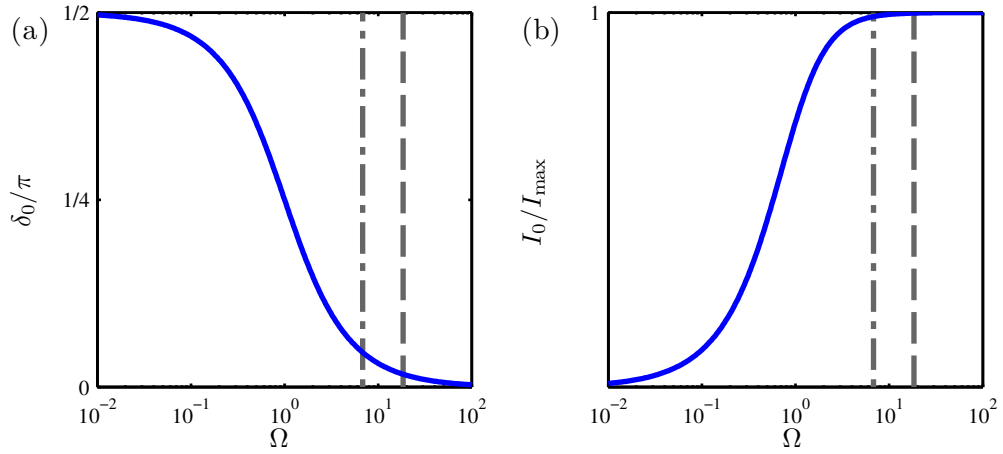

Figure 2.4: The induced current in the copper ring depends on the value $\Omega = \frac{\omega L}{R}$. (a) The phase δ_0 decreases with Ω, and the phase shift between $\vec{B}_{\text{ind}}$ and $\vec{B}_{\text{drive}}$ is π when $\delta_0 = 0$. (b) The maximum current is reached when the conductor couples well to the AC field. The estimated values for Ω for the copper ring parameters of ring 1 (dashed) and ring 2 (dash-dotted) are indicated, for $\omega/2\pi = 30$ kHz and $\omega/2\pi = 50$ kHz, respectively.

$$
\begin{aligned}
B_z(r,z,t) &= I_{\text{ind}}(t)\mu_0/(2r_{\text{ring}}\pi\sqrt{Q})(E\cdot(1-\alpha^2-\beta^2)/(Q-4\alpha)+K) \\
B_r(r,z,t) &= I_{\text{ind}}(t)\mu_0\gamma/(2r_{\text{ring}}\pi\sqrt{Q})(E\cdot(1+\alpha^2+\beta^2)/(Q-4\alpha)-K),
\end{aligned}
$$

where $K = K(m)$ and $E = E(m)$ are the complete elliptic integrals of the first and second kind respectively, their definition can be found in [103]. Additionally, the following substitutions are used in above equations:

$$
\begin{aligned}
\alpha &= r/r_{\text{ring}} \\
\beta &= z/r_{\text{ring}} \\
\gamma &= z/r \\
\text{defining } \gamma(r=0) &= 0 \\
Q &= ((1+\alpha)^2+\beta^2) \\
m &= (4\alpha/Q).
\end{aligned}
$$

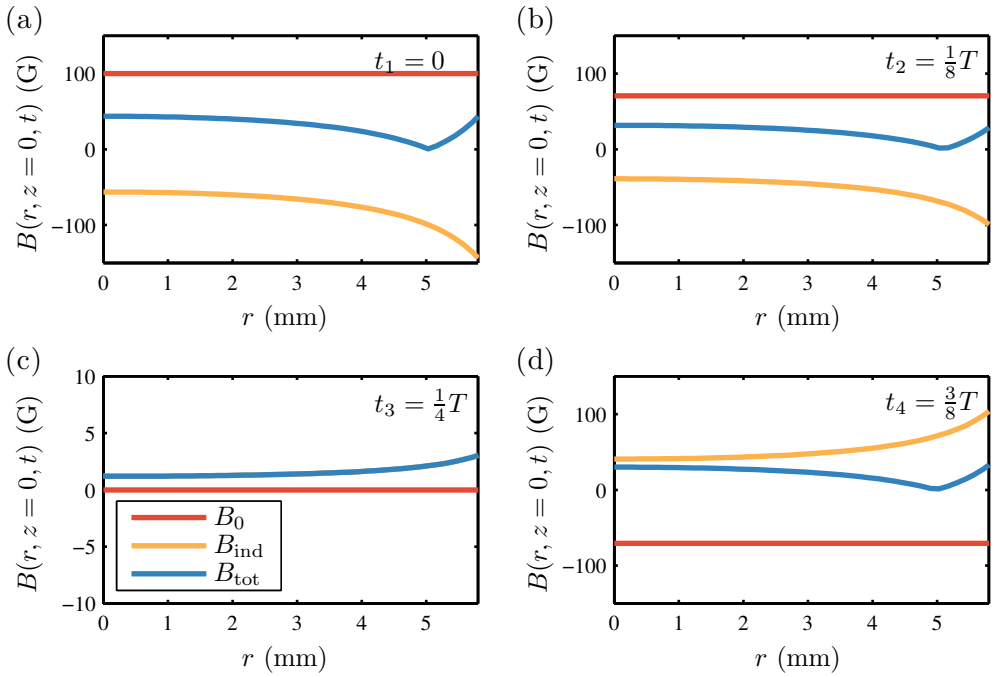

Figure 2.5: Drive magnetic field (B_0, red), secondary magnetic field (B_{ind}, orange) and their superposition (B_{tot}, blue) at different steps in the cycle of duration T for a conducting loop centred at $r = 0$, with radius $r = 7$ mm. The drive field is at its maximum at $t = 0$ (a), decreases for $t = \frac{1}{8}T$ (b), is zero for $t = \frac{1}{4}T$ (c) and has changed sign for $t = \frac{3}{8}T$ (d). There is a phase difference of $\pi - \delta_0$ between the drive and the secondary field.

The direction of the magnetic fields is $\vec{B}_r = B_r \cdot \hat{e}_r$ and $\vec{B}_z = B_z \cdot \hat{e}_z$. There is no magnetic field along $\hat{e}_\Phi$. The total magnetic field at each point is then

$$\vec{B}_{\mathrm{tot}}(r, z, t) = \vec{B}_{\mathrm{drive}}(r, z, t) + \vec{B}_{\mathrm{ind}}(r, z, t) \tag{2.21}$$

$$= B_r(r, z, t) \cdot \hat{e}_r + (B_0(r, z, t) + B_z(r, z, t)) \cdot \hat{e}_z \ . \tag{2.22}$$

Several steps of a cycle with period T are shown in Figure 2.5 for $t = 0, \frac{1}{8}T, \frac{1}{4}T$, and $\frac{3}{8}T$. Displayed is the drive field, B_0, the secondary magnetic field, B_{ind}, and the superposition, B_{tot}, in the plane of the ring ($z = 0$), as a function of the distance, r, from the ring centre. The input parameters are $B_0 = 100\ G$ and $\omega_{\mathrm{drive}}/2\pi = 30$ kHz for the magnetic field, the ring parameters are as for ring 1 in Table 2.1. In the infinitely thin wire approximation, the inner radius (7 mm)

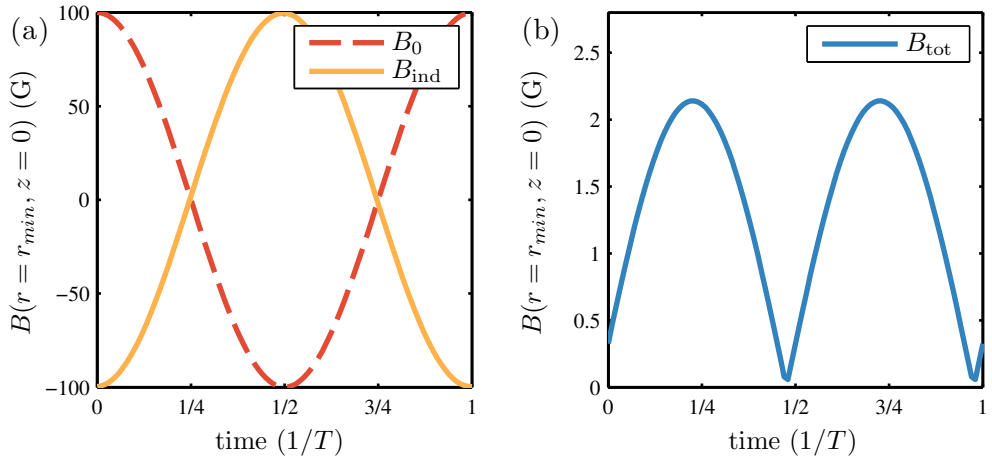

Figure 2.6: Magnetic field time evolution over one cycle (with period T) at the position of the time-averaged magnetic minimum: (a) individual fields and (b) their superposition.

is taken as the position of the current carrying loop. We discuss later that this is not a valid assumption for a finite conductor, but it avoids the trap forming inside the conductor in the simulation. We can see that over the whole radius of the ring, the total field is small for $t = \frac{1}{4}T$, because the fields are $\pi - \delta_0$ out of phase, but it is not zero. The time evolution of the magnetic fields and their superposition at the time-averaged minimum position is shown in Figure 2.6.

When we now take the above magnetic field and look at it not only along r, but in 3D, then we see that the fields cancel out in a time-varying circle in the plane of the ring, wherever $\vec{B}_{\text{ind}}(r, z = 0, t) = -\vec{B}_{\text{drive}}(t)$, to give $|\vec{B}_{\text{tot}}(r, z, t)| = 0$ at the radial position $r_{\text{zero}}(t)$. This is just like the bias field cancelling the field around a straight wire in [99], however the fact that we use AC field with a phase lag means that the cancellation point, $r_{\text{zero}}(t)$, travels between the centre and the edge of the copper ring with the frequency of the AC drive field.

With our drive frequency of tens of kHz we are in the TOP trap regime, where the atoms are too slow to physically follow the magnetic minimum instantaneously, and it is the time average of the magnitude of the magnetic field, $\langle|\vec{B}_{\text{tot}}(r, z)|\rangle_t$, that creates the trap. The time-averaged magnetic minimum is obtained from the time-varying fields in Figure 2.5. It forms in the plane of the

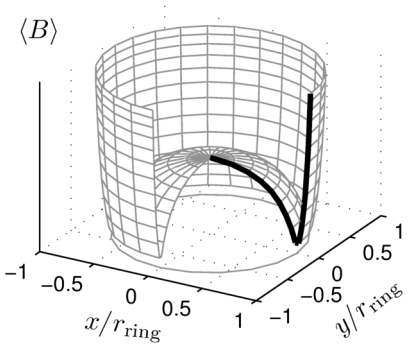

Figure 2.7: Wine bottle: the time-averaged magnetic field at $z = 0$ as a function of the relative positions x/r_{ring} and y/r_{ring}. The magnetic field becomes infinitely large towards the edge of the ring and, displayed is only a limited range.

ring, close to the inner edge, which produces the wine bottle shape shown in Figure 2.7. We can see that this potential has different confinement towards the outer edge and the inside of the trap, with the outer confinement being much stronger and the trap much steeper than at the central saddle-point. The trap depth for the ring trap is then defined over the potential difference between the minimum and the saddle-point.

Additionally to the magnetic potential, the atoms also feel the gravitational potential along $\hat{e}_z$:

$$U_g = M_{\text{Rb}} g z \ . \tag{2.23}$$

With Equation 2.2, the total time-averaged potential is then:

$$U(r, z) = m_F g_F \mu_B \langle |\vec{B}_{\text{tot}}(r, z)| \rangle_t + M_{\text{Rb}} g z \ , \tag{2.24}$$

the minimum of which marks the trapping position, r_0 and z_0. The time-averaged potential along r and z, including gravity, is shown in Figure 2.8. The input parameters are the same as in Figure 2.5. Here, the trap minimum is at $r_0 \approx 5$ mm and $z_0 \approx 0$ mm. The trap depth is $U_{\text{trap}} = 1.7$ mK, which is the potential difference between the trap minimum, U_{min}, and the potential at the lowest saddle point, U_{saddle}, at the centre of the ring. In this example, the saddle point is at $r_s = 0$ mm, due to the symmetry of the potential, and $z_s = -0.7$ mm, which is due to gravitational sag.

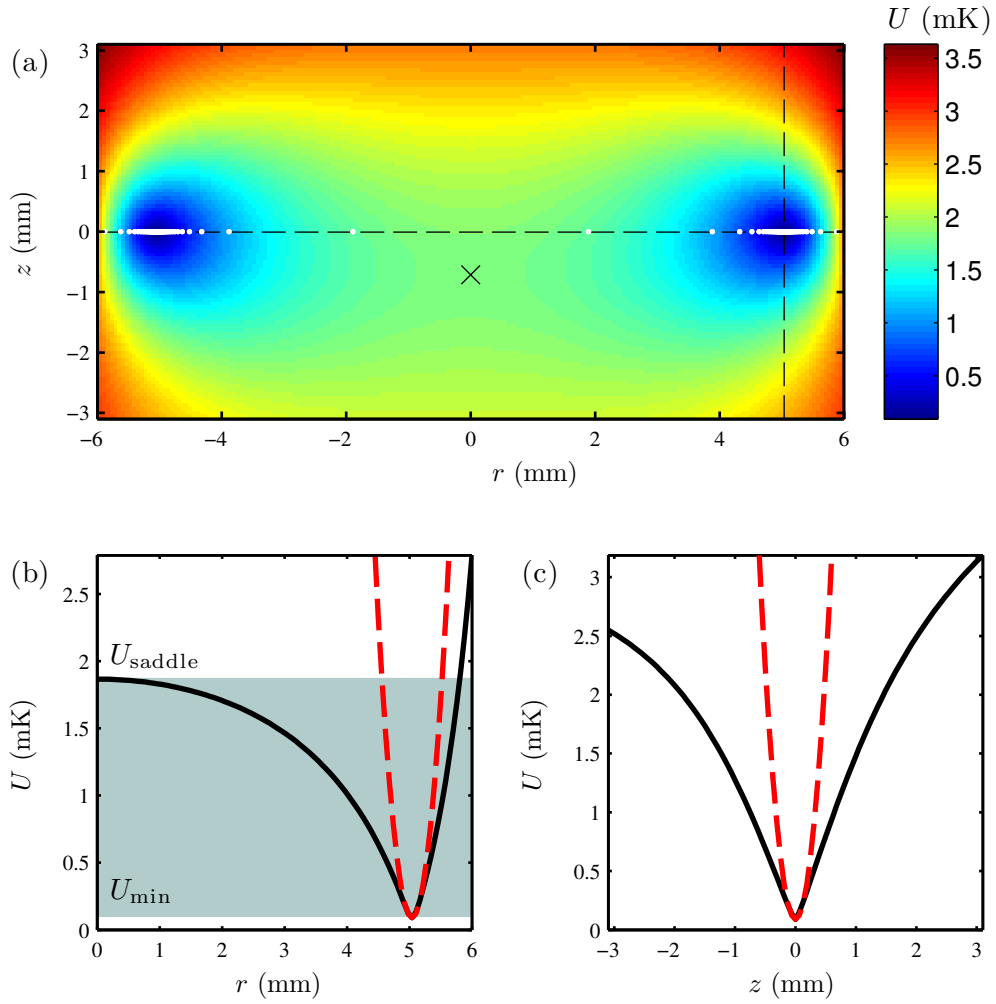

Figure 2.8: Trapping potential: (a) the time-averaged potential across r and z, the black lines mark the r and z position of the trap minimum, the black cross mark the saddle point, the white dots indicate instantaneous positions of the magnetic zeroes. The time-averaged potential along r (b) and along z (c) at the trapping position. The saddle point (U_{saddle}) minus the potential minimum (U_{min}) determines the trap depth, as indicated in (b). The red dashed lines in (b) and (c) are harmonic trap fits, to obtain an approximate trap frequency for the bottom of the trap.

Although the shape of the trap is not harmonic everywhere, we can approximate the bottom of the trap with a harmonic potential by a Taylor expansion around r_0:

$$U_{\text{harm}}(r) = U_{\text{min}} + \frac{1}{2}\frac{M_{\text{Rb}}(2\pi\omega_r)^2(r-r_0)^2}{k_B} \ , \tag{2.25}$$

from which the trap frequency, ω_r, can be extracted. The same approximation can be applied to the z potential, to get ω_z from $U_{\text{harm}}(z)$. Figure 2.8 (a) and (b) show the fitted harmonic potentials at the trap minimum. It becomes clear from the fit that the harmonic approximation is only really valid around the bottom.

2.2.2 Offsetting the magnetic zeroes

From Figure 2.8 we can see that the magnetic zeroes pass through the time averaged trapping position for part of the cycle. This will be a leak in the trap and reduce the trap lifetime drastically, because the atoms can undergo Majorana spin-flips and be lost from the trap (see Section 2.1). To avoid atom loss at magnetic zero points, an additional DC field is applied. The magnetic field is then

$$\vec{B}_{\text{tot}}(r,z,t) = \vec{B}_{\text{drive}}(r,z,t) + \vec{B}_{\text{ind}}(r,z,t) + \vec{B}_{\text{DC}} \ , \tag{2.26}$$

where $\vec{B}_{\text{DC}}$ is the bias field, constant in z, r and t over the trap region. If we apply $\vec{B}_{\text{DC}}$ along z, then there will never be a magnetic zero around the trap minimum, if $\vec{B}_{\text{DC}} - (\vec{B}_{\text{drive}}(r,z,t) + \vec{B}_{\text{ind}}(r,z,t)) > 0$ at all times. The DC field must always be larger than the magnetic field in Figure 2.6 (b). We can see in Figure 2.9 that this creates a safe region at the very minimum of the time averaged potential, as the magnetic zeroes are pushed out. In this example, we apply a bias field along z with $B_z \approx 8$ G, which is comparable to our experiment parameters. The trap depth slightly decreases in the case of a DC offset (this is usually the case for Majorana offset fields), and the trap bottom gets flatter, as shown in Figure 2.10. As in the TORT trap (compare Section 2.1.1), we still have the "circle of death" cycling through the potential: although the magnetic zeroes are pushed away from the immediate time averaged trap minimum, high energy atoms will still encounter them while orbiting around the minimum and be expelled. This leads to a velocity-dependent truncation of the atoms. Ignoring the complexity of the

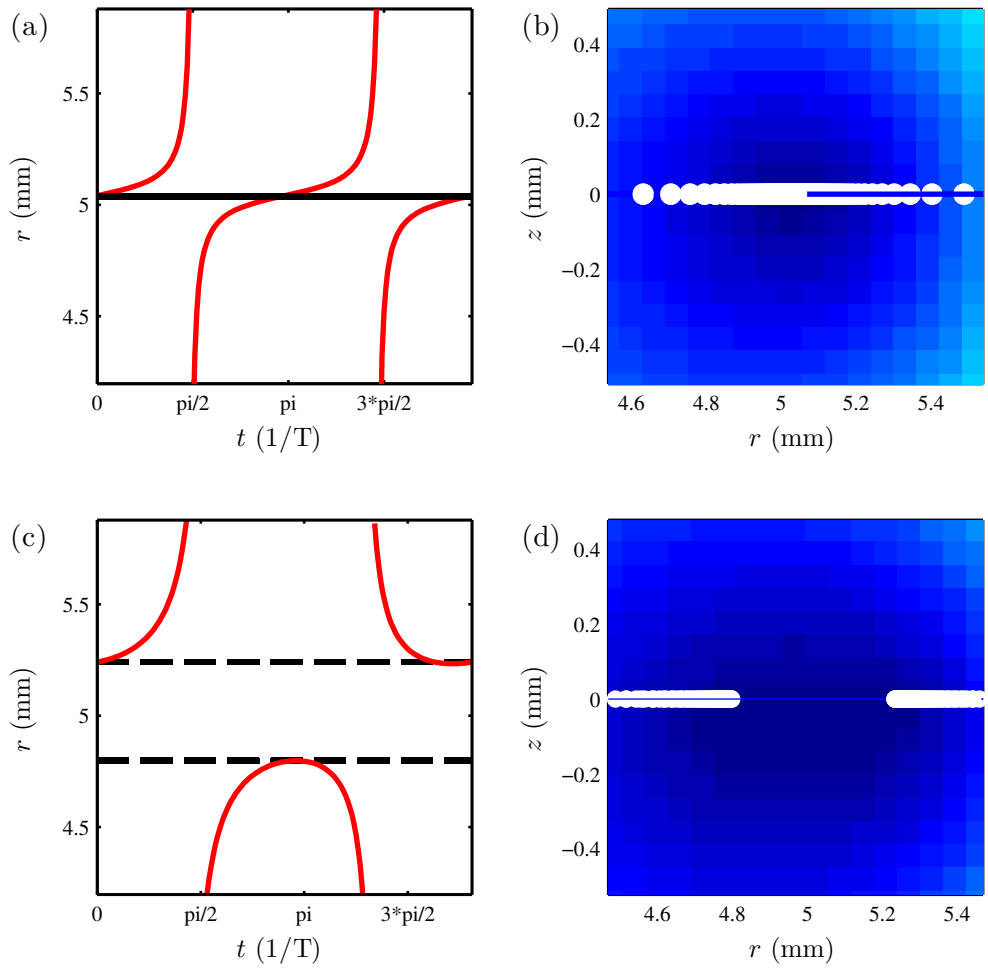

Figure 2.9: The radial position of the zeroes without (a),(b) and with a magnetic bias field (c),(d) is shown. The zero-free region is visible.

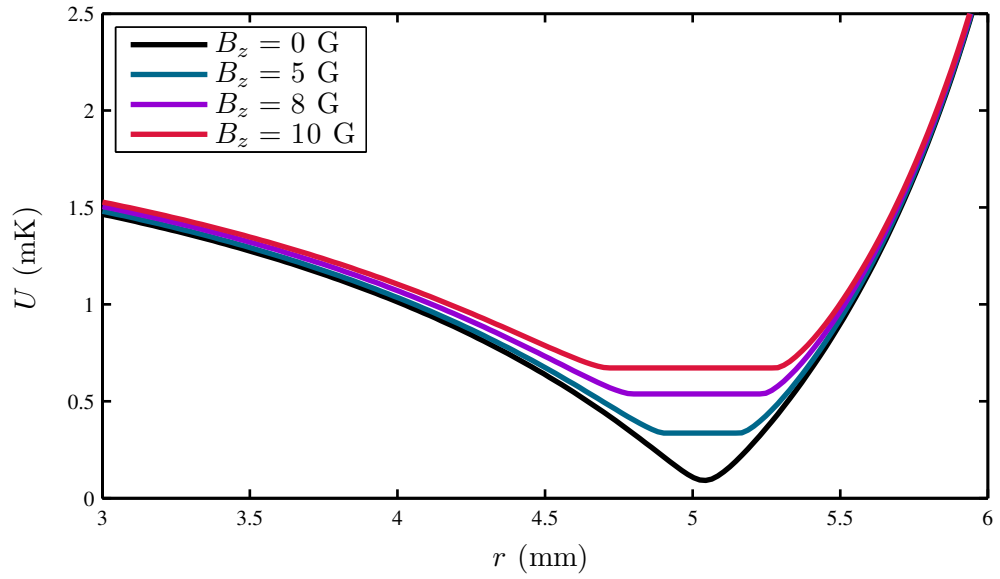

Figure 2.10: (a) With added bias field, B_z, the zeroes are pushed out, and the trap flattens at the bottom. Shown are curves for $B_0 = 100$ G, for different B_z.

problem (i.e. coupling between kinetic energy and position, duration of magnetic zeroes at a certain position), we can regard the truncation as having a sharp edge, removing atoms with energies above a certain threshold from the cloud. This is depicted in Figure 2.11 (a), where a cloud of 45 μK is assumed to have a Maxwell-Boltzmann distribution of velocities in all directions, $f(v_x), f(v_y), f(v_z)$. The distribution $f(v_x)$ is shown before (dashed) and after (solid) truncation. Here, the truncation temperature is set to 100 μK. The distribution of the speed $v_s = 4\pi v^2(f(v_x)f(v_y)f(v_z))$ is shown in Figure 2.11 (b). This shows how even a truncation at relatively high temperatures compared to the temperature of the cloud (100 μK compared to 45 μK), has a severe effect on the velocity distribution. In reality, this edge is not expected to be as sharp, but it will nevertheless influence the temperature of the atomic cloud. As the atoms are not dense enough to re-thermalise on the timescale of the experiment, the truncation will not lead to a colder cloud, as happens for for evaporation. Instead, it will stay in this truncated state. This introduces some problems for our temperature analysis for atoms in the ring trap, because the temperature is now not well defined, see Section 4.4.

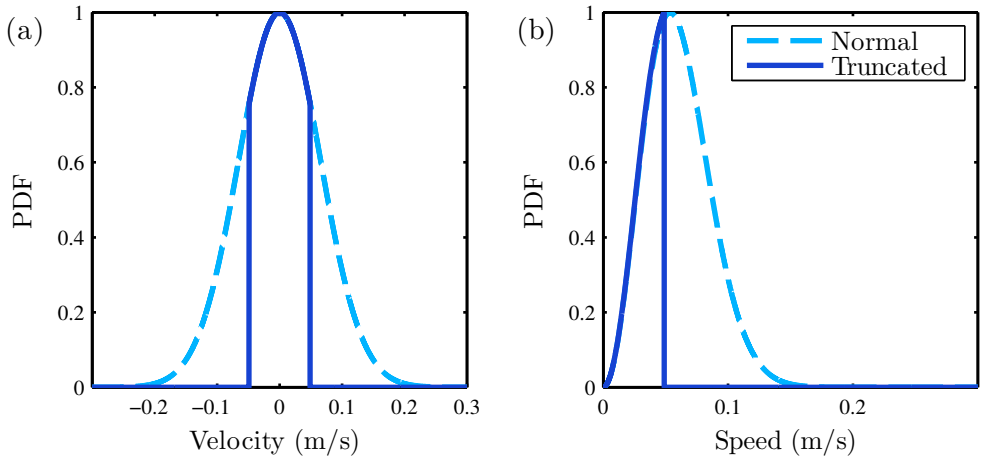

Figure 2.11: Normalised Maxwell-Boltzmann probability distribution function (PDF) of atoms at velocity v (a) and speed v_s (b) for $T = 45$ μK, with (solid) and without (dashed) velocity truncation, corresponding to magnetic zeroes spilling atoms with high kinetic energy. Here, the velocity was truncated at $v_{\mathrm{trunc}} = 1/2\sqrt{k_B T_{\mathrm{trunc}}/M_{\mathrm{Rb}}}$, with $T_{\mathrm{trunc}} = 100$ μK.

2.2.3 Induced current in finite sized ring

The parameters of the copper rings used in the experiment differ from those proposed in [2]. Most importantly, we use a ring of rectangular (ring 1) and tapered (ring 2), rather than circular cross-section. With a width and a thickness of several mm, this geometry decreases the resistance of the ring and increases the radiative cooling compared to the previously proposed wire of 1 mm thickness.

In reality, the finite size of the ring – as opposed to an infinitely small conducting loop – has several implications, which complicate the calculation of the current and the secondary magnetic field: Firstly, the magnetic flux through the ring depends on the area, which increases quadratically with r. Secondly, the resistance increases with r, because the length of one loop around the ring increases, and the resistance is calculated from the resistivity, ρ_{Cu}, as $R = \rho_{\mathrm{Cu}} \cdot l/A$, where l is the length and A is the area of the resistor, implying that charges mainly flow towards the inner edge of the ring. Thirdly, using AC fields to generate a current in a conductor leads to the skin effect, i.e. less current in the inside than at the edges [104].

	Ring 1	Ring 2
Inner radius r_{inner} (mm)	7	2
Outer radius r_{outer} (mm)	12	5
Thickness th_{ring} (mm)	2	2
Inductance L_{ring}(nH)	25 (DC)/43 (30kHz)	6 (DC)/5 (50kHz)
Resistance $R_{\text{ring}}(\mu\Omega)$	98 (DC)/440 (30kHz)	81 (DC)/236 (50kHz)

Table 2.1: Copper ring properties

To have a better idea as to where in the copper ring the charges are flowing, an option is to use finite element analysis: a ring of rectangular cross-section is divided into N small divisions with index j (the small ring divisions are $\leq$ the skin depth in thickness and width), each with its own resistance, R_j and partial inductance, L_{pj}. The current along each division with a given voltage can be calculated using the complex impedance, Z, which is the sum of the self impedance of an isolated ring section (calculated from its self-partial inductance, L_{pj}, and its resistance, R_j) and the mutual impedance, arising from the dependence on the surrounding ring divisions (calculated from the mutual partial inductance, M_{pjk}, and the current, I_k, in the surrounding ring divisions). The voltage-current relation across each ring division j becomes [104, Equation 6.65(a)]:

$$V_j = (R_j + i\omega L_{pj})I_j + i\omega \sum_{k=1,k\neq j}^{N} M_{pjk} I_k \ . \tag{2.27}$$

One can then follow the matrix method in [104] to find the inductances and the currents to calculate the overall current. We can distinguish between different current distributions, depending on the type of conductor and the voltage distribution:

1. Straight conductor with rectangular cross-section and uniform applied voltage: the current is uniform for DC voltage and evenly distributed in the four corners for AC voltage.

2. Looped conductor with rectangular cross-section and uniform applied voltage: the current is mainly at the inner edge for DC voltage and mainly in the two inner corners for AC voltage.

3. Looped conductor with rectangular coss-section and induced AC voltage (i.e. non-uniform, r^2-dependence): the current is mainly in the two outer corners.

The current distribution for above cases are shown in Figure 2.12, with input values as in our experiment (1^{st} generation ring) where appropriate. The mutual inductances for the wires were calculated using [104, 105]. For our ring (looped conductor with rectangular cross-section in induced voltage), the analysis shows that most of the charges flow close to the outside edge of the copper ring, mainly in the corners (see Figure 2.12 (e)). At the frequency of 30 kHz, the skin depth for the copper is ~ 0.4 mm. For a more appropriate simulation of the trapping potential, this calculation of the induced current is implemented in the simulation [106] from which the trapping potentials are obtained.

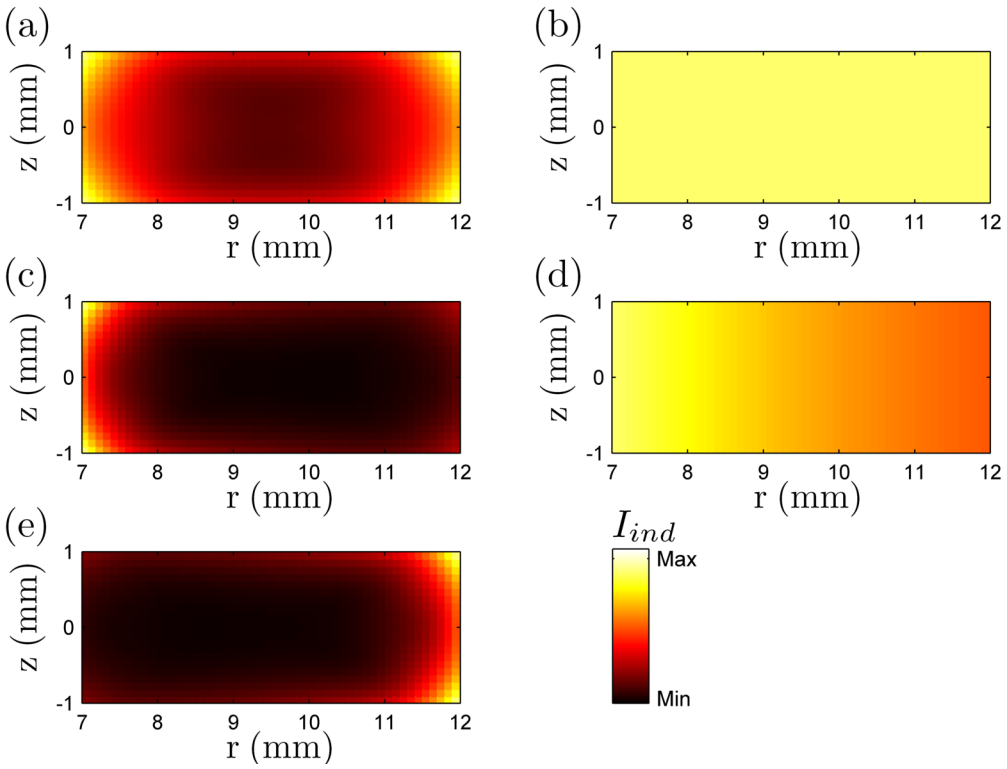

Figure 2.12: Current distribution for different conductors and voltages: straight wire with uniform AC (a) and DC (b) voltage, looped wire (radius dependent resistance) with uniform AC (c) and DC (d) voltage and looped wire (radius dependent resistance) with induced AC voltage, with EMF $\propto r^2$ (e).

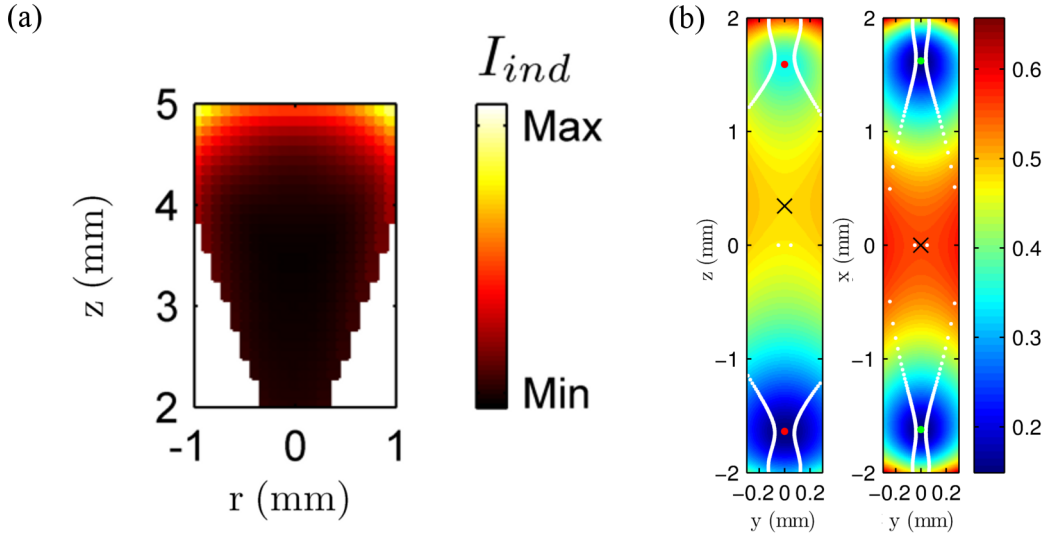

Figure 2.13: (a) Current distribution in the tapered ring of the second generation experiment. (b) Calculated potential in x-z and x-y, the white dots indicate the magnetic zeroes that are displaced by the QP field. Gravity shifts the saddle point from the centre of the ring in z.

2.2.4 Trap simulations from finite element ring models

We can calculate the expected trapping potential with the improved calculations for the current in the ring. From the simulations, we can estimate the trap parameters: without any offset bias, the trap depth is of the order of 1 mK for a drive field of $B_0 = 110$ G and of the order of 0.5 mK for a drive field of $B_0 = 55$ G. The simulations show that the trap depth decreases linearly with added bias field, with a gradient of $\mathrm{dU_{trap}/dB_z} = -50\ \mu\mathrm{K/G}$.

We find the trap minimum at 5.3 mm for low bias fields, which moves towards the ring centre when the trap flattens. At the trap minimum, the adiabaticity is maintained: we find that $\frac{\mathrm{d}\Theta}{\mathrm{dt}}/\omega_L \approx 10^{-2}$, but at the points of the magnetic zeroes, the trap becomes non-adiabatic. Without bias fields, a radial trap frequency of ~ 10 Hz is expected, and the trap frequency in z is of the order of 40 Hz.

The trap for the second generation experiment can be calculated in a similar way. At a drive frequency of 50 kHz, most of the current flows at the outside edge of the copper ring, as shown in Figure 2.13 (a). For a drive field amplitude of

100 G, we calculate a trap depth of the order of 300 μK. Note that in the second generation ring experiment, we use a QP field instead of a bias field to offset the magnetic zeroes (here, $\mathrm{d}B/\mathrm{d}z = 10$ G/cm). The trapping potential with the magnetic zeroes is shown in Figure 2.13 (b).

2.2.5 Scalability

The inductively coupled magnetic ring trap has several advantages regarding the scalability, e.g. for applications on atom chips. The most important feature is that there are no end effects from wires to the conductor, because we induce the current with the AC drive field. Even when the trap is scaled down to micro-chip size, the potential is symmetric over the trap region. The other main advantage and a big difference to many wire chip traps, is that the potential is created with AC fields. Small traps which are created with DC magnetic fields can be subject to potential roughness, when current fragmentation in the conductors occurs (see e.g. [107, 108]). Those trap imperfections are reduced when using AC fields [109]. Scaling of the ring trap will enable a small, smooth, symmetric trapping potential for atom chip applications.

Because the frequencies involved in trapping atoms in time-averaged fields have to keep a certain relationship to each other (the Larmor frequency must be larger than the changing magnetic field, which must change faster than the atoms can move: $\omega_L > \omega_F > \omega_A$), we need to observe the frequency scaling laws. The frequencies scale differently with ring radius [2]:

$$\omega_L \propto r_{\mathrm{ring}} \tag{2.28}$$

$$\omega_F \propto \frac{1}{r_{\mathrm{ring}}^2} \tag{2.29}$$

$$\omega_A \propto \frac{\sqrt{B_0}}{r_{\mathrm{ring}}} \,. \tag{2.30}$$

By reducing the ring size, the condition that the Larmor frequency must be much larger than the AC field frequency is less and less fulfilled as the ratio decreases. This limits the scaling of the trap radius to $\sim$ 1 mm [110] with the methods currently applied. Alternatives that include RF-dressed states to reduce the trap

size further are discussed in a related thesis [110], but those are not scope of this experiment. The scaling limit influences the decision for the ring design of the smaller ring for the second generation experiment.

Chapter 3

Experimental setup

We build the first generation of the inductively coupled ring trap experiment to test if and how the idea is working. In this experiment, laser cooled, thermal rubidium atoms are trapped in the ring. For the setup, we use a single chamber vacuum system with built in rubidium dispensers and an octagonal glass cell (for optical access) with the copper ring, as shown in Figure 3.1. The chamber itself is set up on the optical table which also contains the lasers and the optics for feedback, isolation, frequency shifts and guidance of the light. The heart of the experiment is the copper ring (see Table 2.1 for details), together with the surrounding coils that produce the external and induced AC magnetic field, as well as the DC magnetic field necessary to create the trapping potential. In the next Sections, the main parts of the setup are described separately, followed by the experimental sequence.

3.1 Vacuum system

We use a comparably small vacuum system (the total volume is ~ 1 litre), pumped to ultrahigh vacuum (UHV) by a $S = 20\ \ell/\mathrm{s}$ Varian StarCell ion pump. The chamber consists of a 5-way DIN40 conflat cross with connections to the all-metal valve, the ion pump, the dispensers, a viewport for optical access, and the glass cell, as shown in Figure 3.2. The glass cell ends in an octagonal prism, where

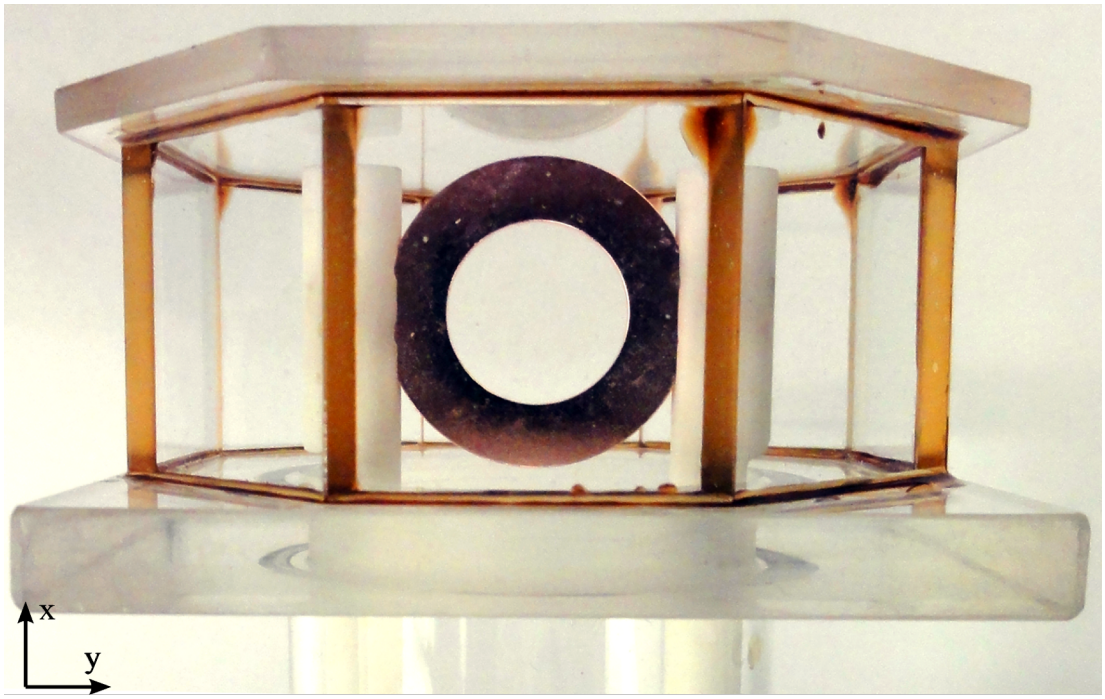

Figure 3.1: The copper ring inside the octagon glass cell, held by ceramic bars.

the copper ring is positioned, held in place by Macor ceramic bars. After several years of operation, the pressure reading from the ion pump is $p < 10^{-8}$ mbar.

3.2 Glass cell

The glass cell is an octagon, with flat front and back, see Figure 3.1. It is homemade, with custom-cut, double anti-reflection coated glass plates from Edmunds Optics. To form the octagon body, the glass plates with dimensions of 2.5 × 2.5 cm have angled edges (22.5 °), which are glued together using an epoxy (EPO-TEK 353ND). The body is shown in Figure 3.3 (a). It is then glued to the flat front and back plate, the latter connects to the vacuum chamber via a glass-to-metal joint. The glue is cured by heating the whole cell to 250 °C. Figure 3.3 (b) shows the finished cell.

The octagon shape was chosen so that the beams can enter the glass cell normal to the glass surface (i.e. the angle of the glass face matches the incident

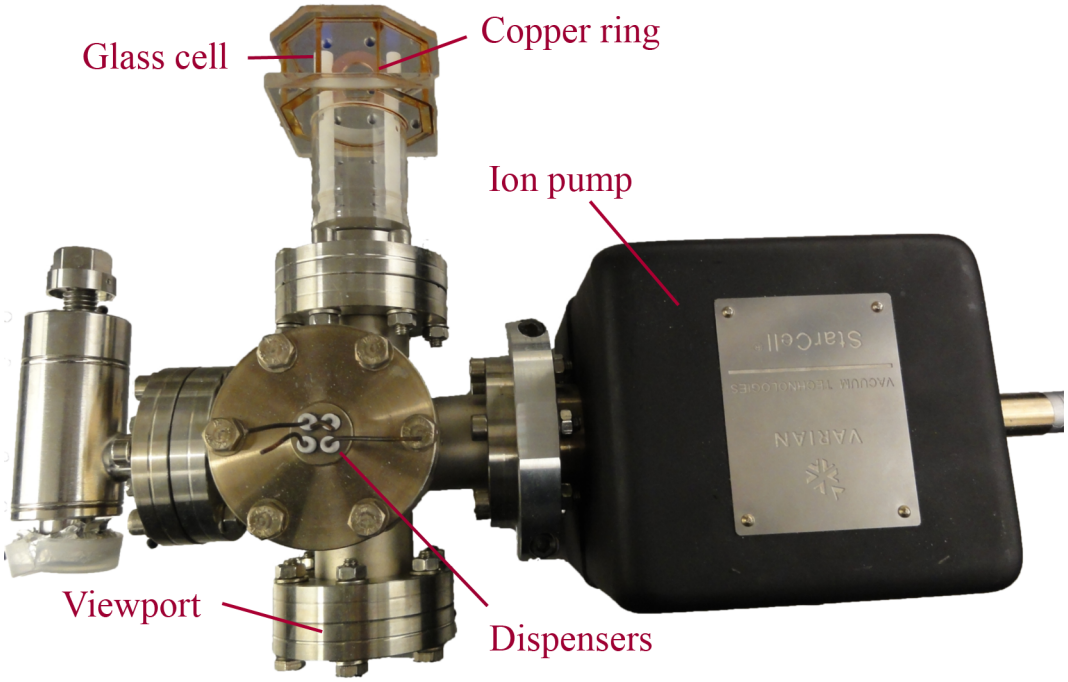

Figure 3.2: Our first generation vacuum system viewed from above. The vacuum is maintained by the Varian Star Cell pump, the glass cell holds the copper ring.

angle of the light) in case of off-axis light. We have not used this feature, as all beams enter the cell along the x, y and z axes.

3.3 Atom source

The rubidium atoms are released from four separate atomic dispensers (SAES Getters Alkali Metal Dispensers) that are built into the vacuum system. Each dispenser is attached to one of the four pins of a feedthrough; all of the dispensers are grounded through the chamber. This allows us to use each dispenser individually, by running a current through it to heat the metal, which causes a chemical reaction and releases the atoms as vapour into the vacuum chamber. To release sufficient rubidium for our experiment, a current of $I_{\mathrm{Rb}} = 2.8 - 3.2$ A is required. Running one dispenser at a time at I_{Rb} for several hours a day, we find the lifetime of a dispensers to be longer than a year.

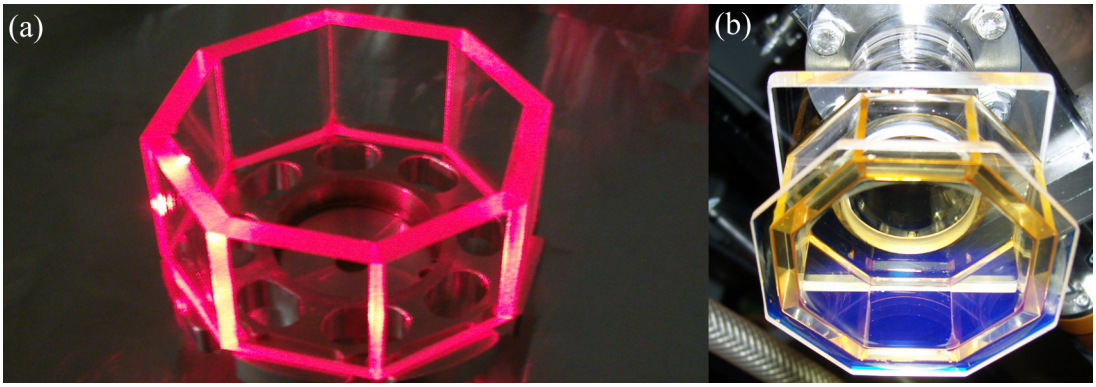

Figure 3.3: The homemade glass cell: (a) The octagon cell is glued together from individual glass plates with angled edges. (b) Once the body is complete, it is glued to flat front and back plates. A glass-to-metal joint connects the cell to the chamber.

3.4 Magnetic field producing coils

Different sets of coils are built around the glass cell to produce the desired magnetic fields:

1. Magneto-optical trap (MOT) coils which provide the magnetic quadrupole (QP) field for the trap

2. Shim coils, which provide a magnetic field that counteracts the Earth's magnetic field and reduces it to zero at the position of the MOT. These coils are also used for the bias field, B_z, see below.

3. Single pulse coil to position the atoms at the optimum loading position for the ring.

4. AC drive coils in Helmholtz configuration that provide the AC magnetic field and induce a current in the copper ring.

The dimensions of the coils can be found in table 3.1.

MOT coils The MOT coils are designed to produce both the QP field for the MOT as well the stronger QP field for a purely magnetic trap. Large currents up to 130 A are needed to produce the required magnetic fields and are provided

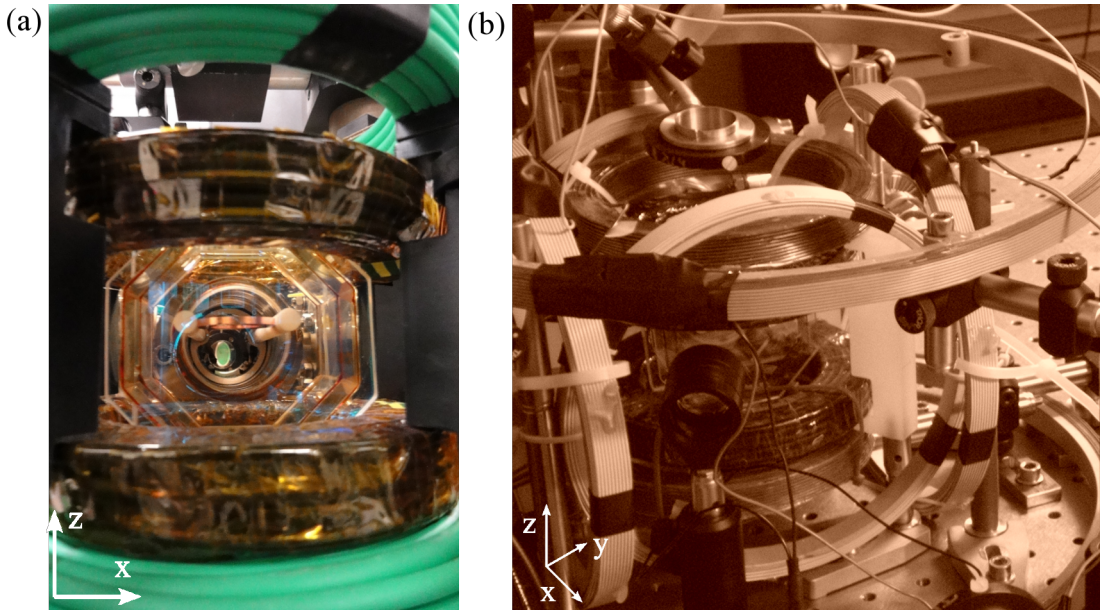

Figure 3.4: (a) MOT coils (green) and AC drive coils (brown) around the glass cell, with the copper ring in the centre. (b) The shim coils in x (NS), y (EW) and z (UD) are visible around the chamber.

by an Agilent power supply (N8733A). The large currents make water cooling necessary, which is why the coils are made of hollow copper pipe. The coils around the glass cell are shown in Figure 3.4 (a).

For optical access, the MOT must be made below the ring, where the atoms are also transferred into a QP trap. But the atoms need to be loaded into the ring trap, which is in the plane of the ring. To bridge this gap, we move the atoms in a QP trap from the MOT position ($z \approx -15$ mm) the ring trap position ($z = 0$ mm) by shifting the position of the magnetic minimum. This is achieved by running asymmetric currents in the QP coils, which displaces the magnetic minimum from the centre. For a smooth transport, we use a FET circuit, which channels the current difference between top and bottom coil through a bypass. The coils are centred on the ring, so that we need a symmetric current when the ring loading position is reached, but a higher current in the top coil for the MOT. The MOT position relative to the ring and the bypass circuit are shown in Figure 3.5. We have designed a FET circuit that is regulated with two input values: V_1, which controls the magnetic field gradient, and V_2, which controls

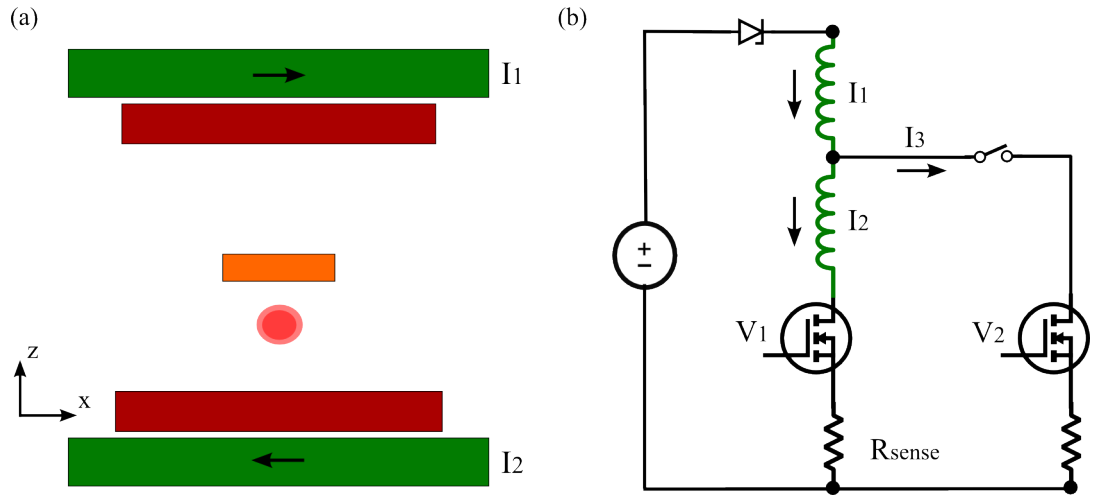

Figure 3.5: (a) The MOT is created underneath the copper ring for optical access. The atoms need to be moved along z in a QP trap, which is shifted by changing the current ratio, I_1/I_2, between the coils. (b) The currents are adjusted with a two-part FET circuit, which channels the appropriate current through a bypass. The circuit shows the coils, the FETs and the sense resistors for the feedback circuit.

the position of the magnetic minimum to shift the atom cloud. The currents are therefore adjusted to keep the desired ratio constant, even if the gradient changes: $\frac{I_1}{I_2} = \text{const.}$, where $I_2 = I_1 - I_3$, see also Figure 3.5 (b). Current feedback comes from the sense resistors.

To counteract Majorana losses, it was originally thought to use the MOT coils to produce a QP field while the AC drive field is on. This would push the magnetic zeroes out of the ring trap region, as explained in [2]. Unfortunately, we had to dismiss this idea: the AC field of the drive coils induces a large voltage in the other coils. A Zener diode and a relay are therefore installed, to avoid current flow through the MOT coils and to electrically disconnect the circuit, shortly before the AC field switches on, as shown in Figure 3.5 (b). To reduce Majorana losses in the ring trap, a bias field from the shim coils is used instead.

Shim coils There are three sets of shim coils that produce independent bias fields in north–south (NS), east–west (EW) and up–down (Z) direction. We use the directions as labels to distinguish the fields. The shim coils have two main

Coils	N	r (cm)	s (cm)	B field at centre
AC	30	5	6	4.9 G/A
MOT	20	6	11	0.4 G/cm/A
Shim EW	60	10	19	2.7 G/A
Shim NS	50	8	18	2.5 G/A
Shim UD	70	15	17	3.9 G/A
Pulse	94	5	single coil	3.7 G/A

Table 3.1: Coil properties: N is the number of turns, r is the mean radius, s is the mean separation and the last column is either the magnetic field, B, or the magnetic field gradient, dB/dz, at the centre of the coils (ring position) in G/A, or G/cm/A, respectively.

functions: firstly, they are used to cancel stray magnetic fields and the Earth magnetic field, which is very important for the molasses phase. The cancelling field is adjusted by hand, using the visual appearance of the molasses cloud. The current in the coils is controlled by a FET circuit, where the cancelling field is adjusted locally. Secondly, the shim coils are used to create bias fields during the experiment, e.g. for optical pumping, imaging and as a DC bias for the ring trap. The experimental bias fields are controlled remotely via LabVIEW. Heating of the coils limits the available magnetic fields, which mainly affects the bias field, B_z, that is necessary for creating the ring trap. The shim coils around the chamber are shown in Figure 3.4 (b).

Pulse coil Once the atoms in the QP trap are shifted along z into the plane of the ring, they also need to move radially, away from the centre of the ring (the MOT coils and the ring are on the same axis), to overlap the QP trap with the ring trap. The shim coils can not provide enough bias to do so, and a single coil is installed to push the atoms outwards. The pulse coil acts along the EW-direction, to load the atoms at the left side of the ring. The magnetic field from the pulse coil allows us to optimise the loading position of the atoms for differently shaped ring traps.

AC drive coils The AC drive coils are a main part of the experiment, and we want them to provide a large magnetic field. They are wound from hollow copper

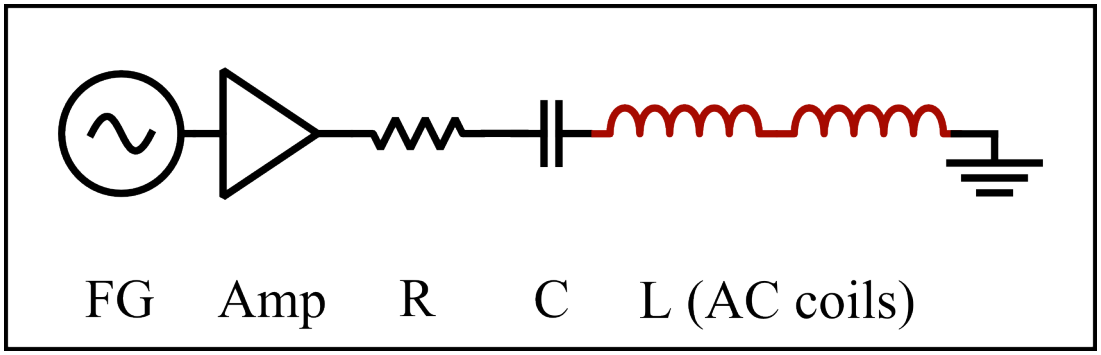

Figure 3.6: Resonant circuit including the function generator (FG), the audio amplifier (Amp), a bank of resistors in parallel (R), a number of capacitors in parallel (C) and the two AC drive coils in series (L). R and C are chosen to produce the desired output load and resonance frequency.

pipe, so that they can be water cooled. The coils around the glass cell are shown in Figure 3.4 (a). To drive the required current in the coils, the output from a function generator is fed into a audio amplifier (Behringer Eurorack EP1500), which is connected to a resonant circuit that includes a bank of resistors, a set of capacitors and the AC drive coils, as shown in Figure 3.6. The amplifier needs a 2 Ω load, for which the resistance is adjusted (we add a total of 15×10 Ω resistors in parallel, to give a value of $R \approx 0.67$ Ω). The amplifier with the bank of resistors and their water cooling pipes are shown in Figure 3.7.

For the copper ring to produce the required magnetic field, we want a drive frequency of 30 kHz. The resonant frequency needs to be matched, and with a capacitance of $C = 155$ nF, we get a resonant frequency of $f_0 = 30.5$ kHz. The resonant circuit is changed for the second generation experiment to obtain a different drive frequency, and more information on the procedure can be found in Section 6.2.7.7.

3.5 Lasers

Diode lasers, particularly in tunable configurations such as the external cavity diode laser (ECDL), are widely used in atomic physics experiments due to their compactness, ease of operation and highly controllable properties [111]. We use

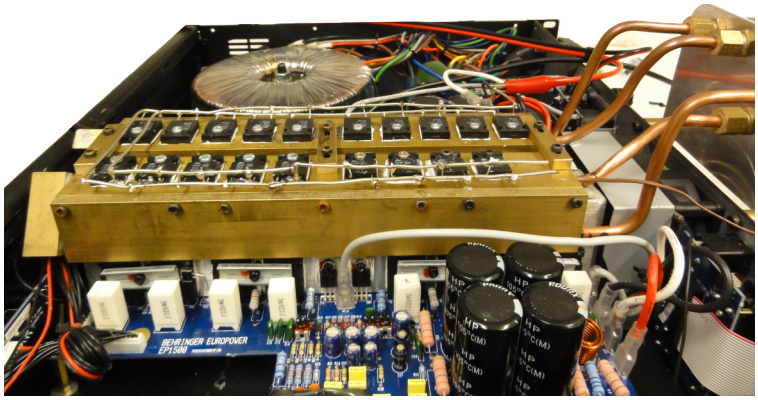

Figure 3.7: Audio amplifier to produce AC drive field, shown is the large bank of resistors and the water cooling pipes.

two ECDLs, one mainly for cooling ("cooling laser") and one for repumping ("repump laser") during the radiative cooling phase, both lasers use diodes for operation at 780 nm. For design and use of ECDLs in atomic physics, see [111, 112, 113, 114].

We have developed a quasi–monoblock Littrow design, where the main body of the laser is machined out of a single piece of aluminium, for optimized thermal stability [115] and protection from air turbulence. The laser consists of three main parts: a main body, a feedback mount and a front plate, a schematic is shown in Figure 3.8. The main body holds the laser diode and the collimating lens, and it is temperature stabilized with a thermoelectric cooler (TEC). A 1800 lines/mm gold coated holographic grating is attached to the feedback mount, which reaches into the hollow core of the main body. The zeroth order reflection from the grating forming the laser output is reflected off a mirror positioned parallel to the grating, such that angular deviations of the output beam are cancelled when the grating angle is changed [116]. The feedback mount is attached by stiff springs to the front plate and can be adjusted vertically (the direction of the grating grooves) by pivoting on a pair of horizontal bars that define the horizontal axis (see Figure 3.8). Similarly, the front plate is mounted in tension to the main body and can pivot about a line that defines the vertical axis. Feedback is optimised by minimising the threshold current, I_{th}. The wavelength of the laser can be adjusted by horizontal control of the angle of the front plate relative to the main body.

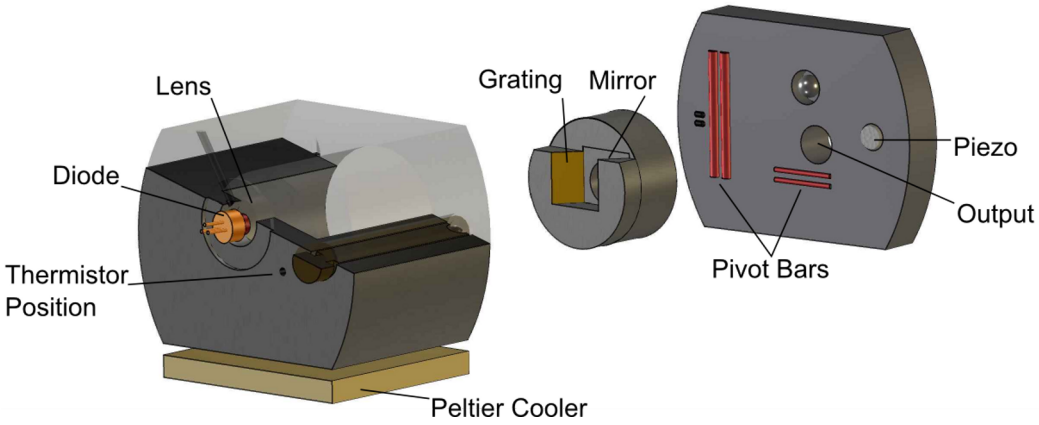

Figure 3.8: Cross–sectional views of the ECDL design showing the back view. The middle part is the feedback mount that holds the grating (gold) and the mirror. On the front plate the main pivot bars are shown in red. Fine screws on the back and the front of the laser adjust the horizontal and vertical alignment. The main body is mounted upon a larger block, as a thermal mass. This design is used to built the cooling and the repump laser.

Coarse control is provided by a fine-pitch screw while fine control is achieved by a piezo-electric transducer. The pivot lines for both angular adjustments are defined by three ground and hardened metal bars - the outer two are embedded in the fixed part of the mount while the third one rests between them and is attached to the moving part. This setup provides independent control of the two grating angles and has in practical use proved to have good stability, needing only slight adjustment of feedback on a less than monthly basis.

All electric and thermal control of the laser is provided by a MOGLabs commercial laser diode controller (MOGbox DLC-202). A saturated absorption signal is recorded with a photodiode and transmitted to the controller and to an oscilloscope. The laser is stabilized to one of the saturated absorption features by applying a 250 kHz modulation to the drive current resulting in a frequency modulation depth of ~ 1 MHz, the laser is then locked to the zero transition of the absorption error signal, locking it to a hyperfine transition. The laser diode controller provides the necessary locking electronics. Slow and fast feedback are applied to the piezoelectric transducer and the diode current, respectively.

With a 780 nm Sanyo laser diode, we have a threshold current of 34 mA and

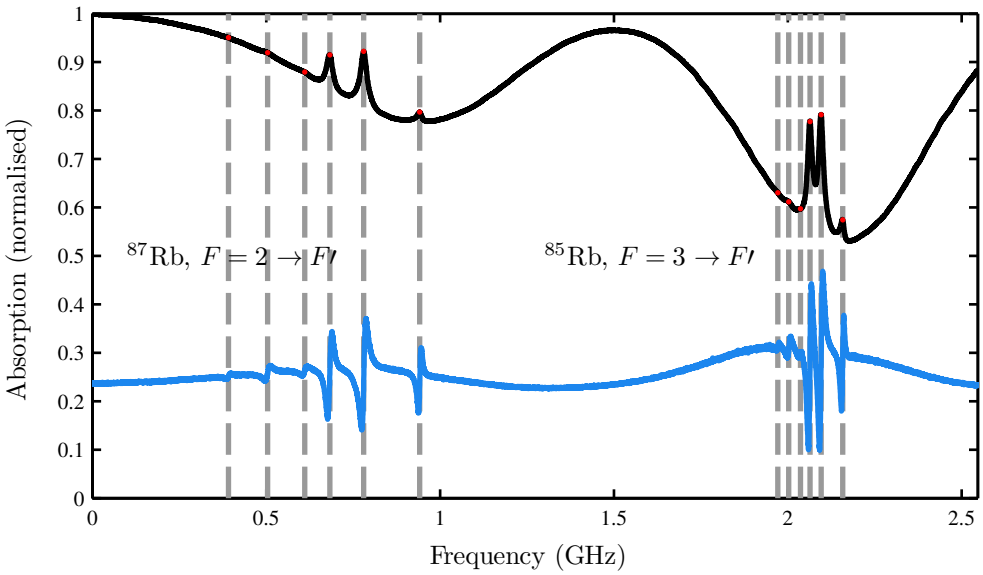

Figure 3.9: Rb absorption signal (black, normalised to undisturbed transmission) and the error signal (blue, normalised, scaled and offset to fit) used for locking the laser to the centre of a transition (zero of the error signal). Left in the spectrum is the cooling transition for ^{87}Rb. The Doppler broadened background is visible, the absorption spectroscopy reveals the hyperfine lines ($F = 2 \rightarrow F'$ and their crossovers, grey dashed lines). From left to right, the transitions are $F' = 1, 1/2, 2, 1/3, 2/3, 3$. On the right side is a ^{85}Rb absorption.

a mode-hop free range of more than 2.5 GHz. The transmitted signal through the cell around the cooling transition (normalised to undisturbed transmission) together with the error signal used for locking the laser (not to scale) are shown in Figure 3.9. The transition lines are indicated, reference values for the frequencies can be found in [41]. The shape of the rubidium absorption spectrum and the position of the transition lines is studied in [117].

3.5.1 Laser stability

We can characterise the laser in terms of its noise, its linewidth and its frequency drift. The absorption error signal from the photodiode is analysed for noise by applying a fast Fourier transform (FFT) using a SR785 signal analyser. Figure 3.10 shows the single sided FFT spectrum of the error signal for an free running and a

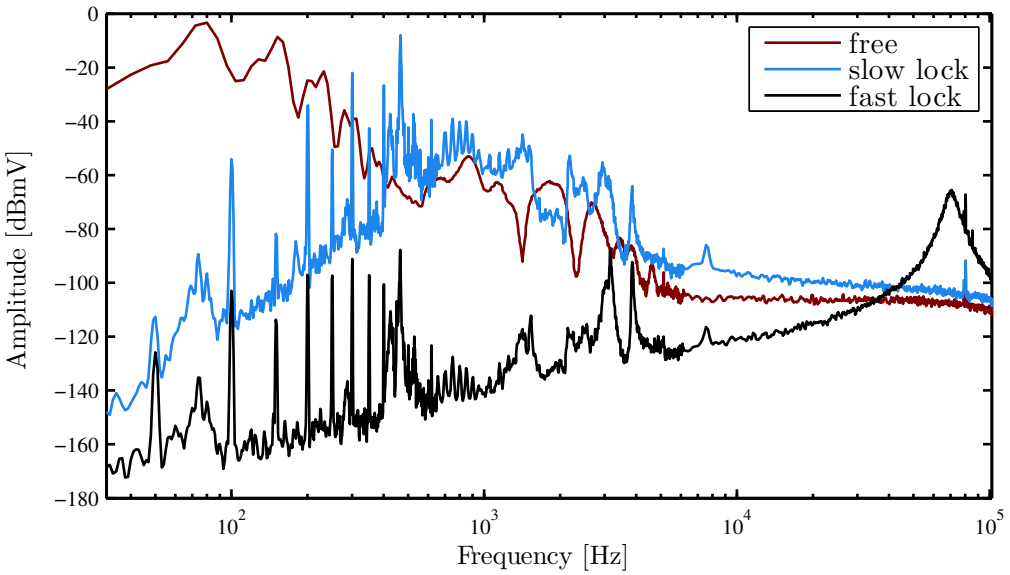

Figure 3.10: The frequency spectrum of the 780 laser absorption error signal at the cooling transition. The frequency components shift from low frequencies to high frequencies when comparing the free running (red), slow locked (blue) and slow and fast locked laser (black). Frequency noise up to several kHz in the unlocked laser is suppressed when the laser is locked, the frequency noise is shifted towards higher frequencies when the fast lock is switched on.

locked laser (slow and slow plus fast lock), both tuned to the cooling transition of the $F = 2 \rightarrow F' = 1/3$ crossover. We see a difference between the three signals: the frequency noise in the low frequency range up to several kHz is suppressed for the locked laser compared to the unlocked laser, shifting further towards high frequencies when the fast lock is added.

The spectrum in Figure 3.10 is the result of three spectra with increasing frequency range (800 Hz, 6.4 kHz, 100 kHz) and decreasing resolution (1 Hz, 8 Hz, 126 Hz bandwidth, respectively), taken of the same signal and then combined (exception: low resolution spectrum was not replaced with high resolution spectrum for the free running laser below 600 Hz). An analysis of frequency spectra for a similar diode laser and the respective noise sources can be found in [117].

From the amplitude noise in the signal we can also estimate the linewidth of the laser: To get a conversion between photodiode signal and frequency, we firstly

scan the laser frequency over the $F = 2 \rightarrow F' = 3$ transition. The frequency axis is calibrated using the known frequency difference between two transitions. The error signal peak-to-peak voltage is related to the (power broadened) linewidth of the transition, and the conversion factor (V/MHz) is calculated. From the error signal of the laser with minimum scanning width the standard deviation of the amplitude is obtained and converted into the linewidth. This shows that the linewidth reduces from 840 kHz for a modulated, unlocked laser to 380 kHz for a locked laser.

The laser is also tested for phase stability in a master–slave setup with and without a tapered amplifier (TA). This becomes important for the second generation ring experiment and for future work including ^{40}K , for which we need to operate at a different frequency. The results (Allan variance and correlation function) are summarised in Appendix B.

3.6 Optical setup

The output of each of the two lasers (cooling and repump laser) is divided by polarising beamsplitters (PBS) into the experimental setup beam and a beam going to the saturated absorption spectroscopy setup in order to lock the lasers to the appropriate wavelength (for saturated absorption, see e.g. [118]). At the laser output, the power in the beam is ~ 50 mW (cooling laser) and ~ 40 mW (repump laser). The cooling laser is then split into multiple beams: the optical pumping beam, the probe beam and the MOT beam, all at different, independently tunable frequencies. The repump beam and the MOT beam are overlapped shortly before the vacuum chamber and then guided such that they enter the glass chamber from three directions. The beams are reflected back onto the chamber, to form a retro–MOT ~ 1.5 cm below the copper ring. The details of the beam setup are explained in the following Sections, a schematic of the layout can be found in Figure 3.11, or the more detailed version in Figure 3.13.

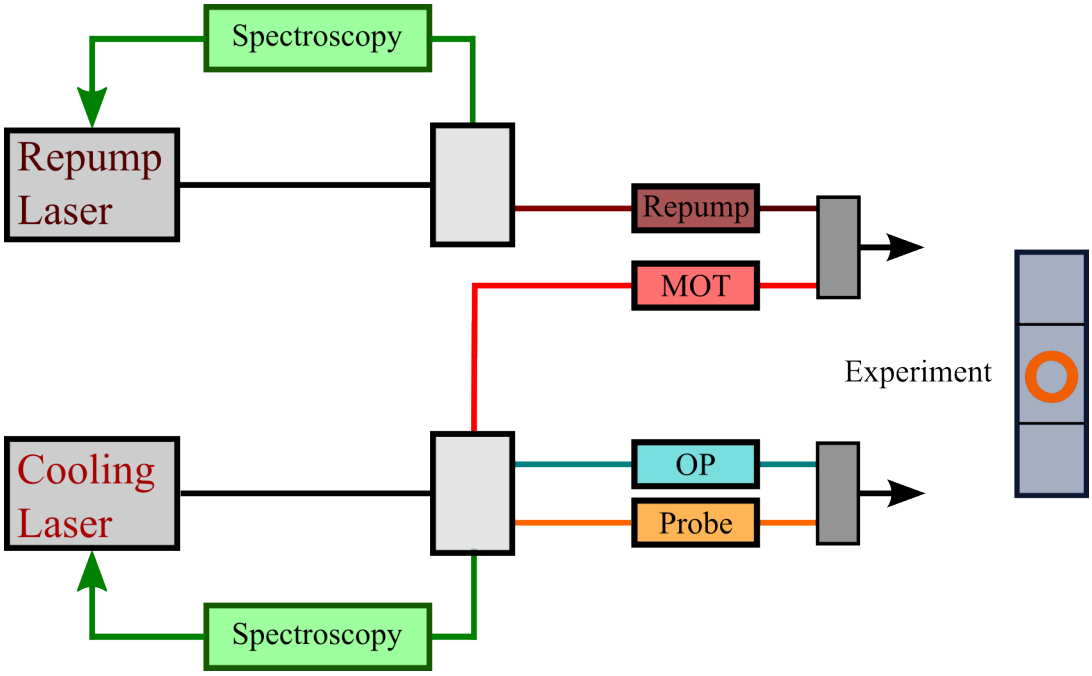

Figure 3.11: Layout of the main optics in diagram form, shown are the different beams and how they are split and combined.

3.6.1 Spectroscopy

Saturated absorption spectroscopy is used for locking the cooling and the repump laser. We also use an acousto-optic modulator (AOM) to shift the frequency of the cooling spectroscopy light (see below for details). For each of the two lasers, the spectroscopy light (~ 0.5 mW) travels from the reflected port of a PBS into a Rb cell. The beam is retro-reflected off a mirror, thereby double passing a $\lambda/4$ waveplate. It travels back through the Rb cell and transmits through the PBS onto a photodiode. The signal is transmitted to the MOGBox laser diode controller to provide the locking spectrum (as in Figure 3.9).

Figure 3.12(a) shows the corresponding level-diagram for ^{87}Rb , with the $5^2S_{1/2} \rightarrow 5^2P_{3/2}$ transition (D_2 line) and the different hyperfine (F, F') levels. The laser frequencies for MOT, probe and OP beam are indicated. For cooling of ^{87}Rb in the MOT, the $F = 2 \rightarrow F' = 3$ hyperfine-transition is used. The cooling laser is locked in the spectroscopy setup to the $F = 2 \rightarrow F' = 1/3$ crossover, but the MOT light is frequency shifted with respect to that, so that it is close to the

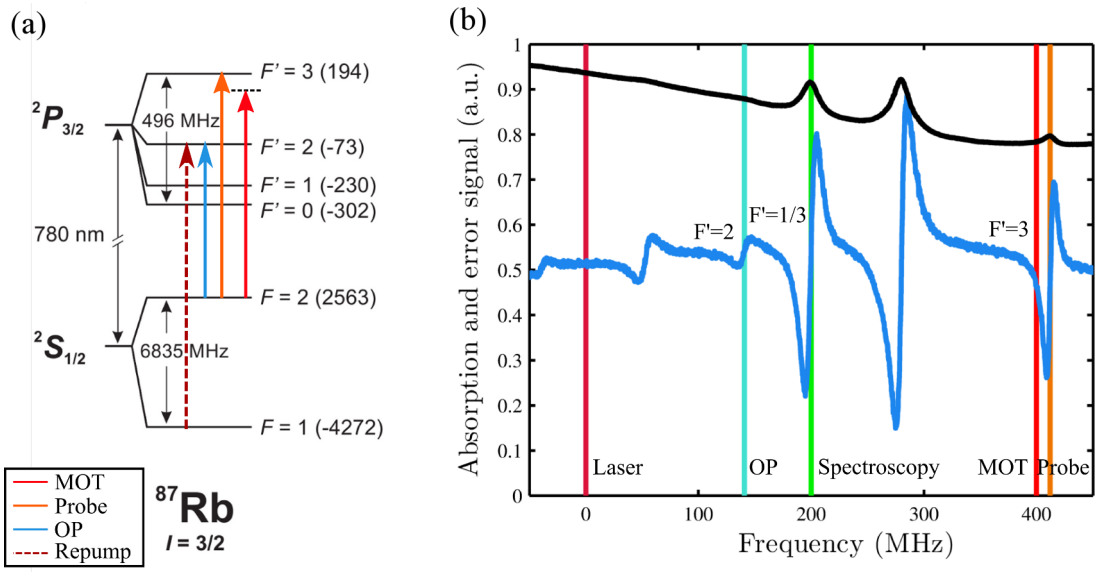

Figure 3.12: (a) Hyperfine splitting of ^{87}Rb. Transitions used for laser cooling (MOT), OP, probe and repumping are indicated (hyperfine splitting diagram taken from [119]). (b) Frequencies of the different beams drawn into the ^{87}Rb spectrum: the unshifted laser frequency ("Laser", dark red) is frequency shifted and locked onto the $F' = 1/3$ crossover transition ("Spectroscopy", green). The OP beam is frequency shifted to be on resonance with the $F' = 2$ transition ("OP", blue), the cooling beam ("MOT", red) is shifted to be red-detuned to the $F' = 3$ transition, and the probe beam ("Probe", orange) matches the $F' = 3$ transition when the atoms are imaged on resonance. The repump transition is not in the picture, because the $F = 1 \rightarrow F'$ transitions are over 6 GHz away from the cooling transition.

$F = 2 \rightarrow F' = 3$ transition (the frequency shifts are shown in Figure 3.12(b)). The cooling cycle is not completely closed: atoms that decay into the $F = 1$ state are lost from the cooling cycle. A repump laser on resonance with the $F = 1 \rightarrow F' = 2$ transition excites the lost atoms to $F' = 2$, from where they can decay back into the $F = 2$ state.

3.6.2 Cooling laser beam setup

The cooling laser outputs an elliptical beam of 48 mW for a drive-current of 98 mA. Two mirrors close to the laser output are used to make the beam as

horizontal as possible and steer it through a set of anamorphic prisms (to make the beam round), followed by a Faraday isolator (to avoid feedback). The beam is then divided into four different arms by four sets of $\lambda/2$ waveplates and PBS-cubes.

Frequency Shifts Independent frequency shifts for the different beams are important, to be able to control the detuning from the cooling transition – one of the important MOT parameters – and the probe beam detuning, e.g. to be able to match the transitions of Zeeman shifted sub-levels. AOMs in each arm allow for independent frequency and intensity control of the four beams (probe beam, optical pumping (OP) beam, spectroscopy beam and MOT beam). An AOM uses RF-induced Bragg-reflections in a crystal to create additional frequency components: $k' = k + nf$, where n is the order. The order can be a positive or negative integer, and double-passing an AOM will lead to twice the frequency shift. To feed only the beam with the correct frequency shift back into the setup (here: $n = +1$), all other outgoing beams are blocked with an aperture. The resulting frequencies for each beam are shown in Figure 3.12.

The AOMs are frequency controlled with a voltage controlled oscillator (VCO). We use Crystal Technology AOMs (models 3200-124 and 3080-122, for frequency shifts around 200 MHz and 80 MHz, respectively) in combination with Mini – Circuits VCOs (ZX95-310A-S+ ($160 - 360$ MHz) or ZX95-100-S+ ($50 - 100$ MHz)). The amplitude is controlled with a frequency mixer (ZP-3LH), which is used in a reversed mode: we apply the VCO output to the LO port, a DC signal to the IF port and take the resulting frequency from the RF port. In this way, we combine the VCO AC output with a DC voltage to get an AC output with controllable amplitude. The signal is amplified (Mini – Circuits ZHL-1-2WX-S) to match the highest efficiency input power of the AOM (34dBm).

The probe beam, OP beam and MOT beam each double pass an AOM. Double passing an AOM has the advantage that the beam alignment does not change when the frequency is changed. However, it also means a substantial power loss, as typically a single pass transmits around 80% of the power.

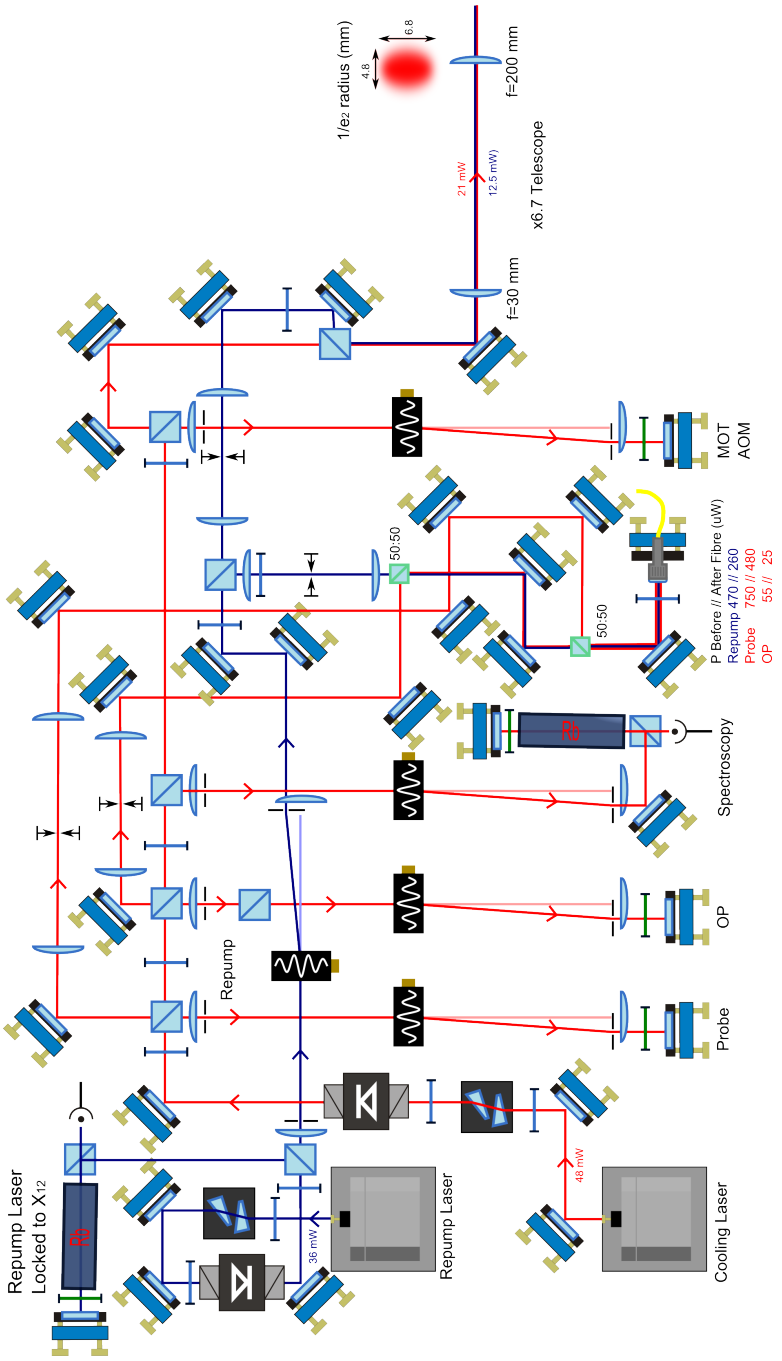

Figure 3.13: Optical setup for the first generation experiment. The cooling laser light is red, the repump laser light is blue. Focal lengths are given next to the lenses, beamsplitters are blue when PBS and green when NPBS, waveplates are blue when $\lambda/2$ and green when $\lambda/4$.

MOT beam The MOT beam is frequency shifted and then combined with the repump light in a PBS. Both beams are magnified by a telescope ($f_1 = 30$mm, $f_2 = 200$mm) to increase the cooling volume of the MOT. The beams now have a $1/e^2$ radius of 4.8 mm in the horizontal and 6.8 mm in the vertical direction (beam still elliptic, despite anamorphic prisms). A shutter (Uniblitz) is placed at the focus of the telescope to avoid residual light through the AOM. The magnified beam is then split into 3 parts, using $\lambda/2$ waveplates and PBS, to provide the MOT cooling beams in 3 dimensions with even power. The total power at this point is ~ 15 mW in the cooling beam and ~ 10 mW in the repump beam. While the vertical cooling light is guided to the top of the chamber via a periscope, the horizontal beams enter the chamber through the side of the octagon and through the viewport of the vacuum chamber. We use a retro-MOT, and the three beams are reflected off a mirror on the other side of the chamber and aligned to overlap with the incoming beam. The beams are circularly polarised according to the MOT requirements described in Section 1.3.1.2, during the reflection each beam also double-passes a $\lambda/4$ waveplate, which changes its circular polarisation. All six beams are overlapped at the position of the magnetic minimum from the QP field for an optimum MOT.

Optical pumping beam The optical pumping beam brings a large fraction of the atoms into the desired hyperfine state. Because we have a magnetic trap, we want to populate the trappable $|F = 2, m_F = +2\rangle$ state, which is achieved by optical pumping (OP). With σ^+ light resonant to $|F = 2\rangle \rightarrow |F' = 2\rangle$, each photon absorption drives a $|F = 2, m_F\rangle \rightarrow |F' = 2, m_F + 1\rangle$ transition, followed by spontaneous emission. After ~ 9 absorption–emission cycles, the atoms will end up in the dark state $|2, +2\rangle$. A schematic is shown in Figure 3.14.

The OP light is frequency shifted into resonance with the OP transition and then fibre coupled and guided to the vacuum chamber. After the fibre, the beam is expanded to ~ 12 mm. It enters the chamber from the bottom, through the reflected port of a PBS. It is centred on the copper ring, to optically pump the atoms along z. Only little light is needed, and the power in the beam after the fibre is ~ 25 μW.

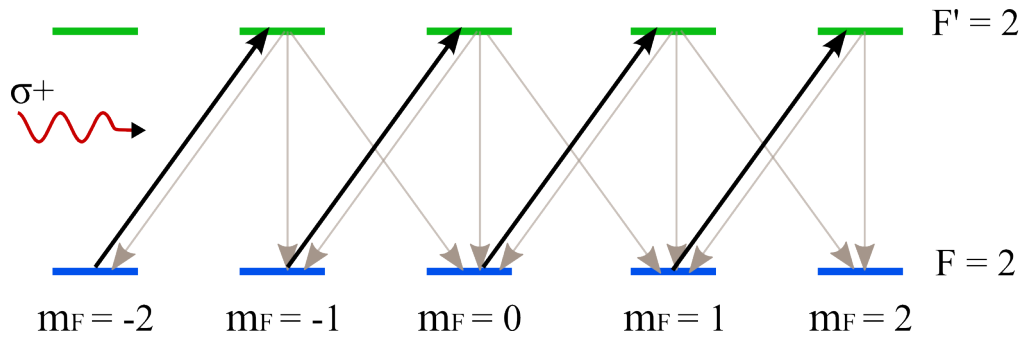

Figure 3.14: Optical pumping scheme. The $\Delta m_F = 1$ transitions that lead to the dark state are indicated in black.

Probe beam The probe beam is used for absorption imaging of the atoms. Because of the magnetic bias field during the experiment, the probe beam has a variable frequency to take the Zeeman shifted atom resonance into account for optimised imaging, but it is centred on the $|F = 2\rangle \rightarrow |F' = 3\rangle$ transition. After frequency shifting the light, it is combined with the OP beam in a 50/50 beamsplitter before the fibre and follows the same path through the bottom of the glass cell. The atoms are imaged along z, with the σ^+ light illuminating the whole region inside the copper ring. On its path through the chamber, it passes two $\lambda/4$ waveplates from the MOT setup (one below and one above the glass chamber) and is then transmitted through a PBS above the chamber into the camera.

3.7 Absorption imaging

The probe beam along the vertical axis is used for absorption imaging. An absorption image is built from 3 separate images that are taken in very short succession: the probe image with the atoms (the atoms are recognisable as a shadow in the probe beam), the reference image (no atoms, but the probe beam is on) and the dark image (no atoms and no probe beam). The images are combined to give the optical density via

$$OD = \ln\left(\frac{I_{\text{Ref}} - I_{\text{Dark}}}{I_{\text{Atom}} - I_{\text{Dark}}}\right). \tag{3.1}$$

A discussion of absorption imaging can be found in [60]. From the optical density, we can obtain the atom number (this will be discussed further in Section 4.2):

$$N = \frac{A}{\sigma_0} \cdot \sum OD, \tag{3.2}$$

with the pixel area A and the atomic resonant cross-section σ_0, and we sum over all pixels. The images are recorded with a Luca Andor CCD camera (Luca R - number of pixels: 1004×1002, pixel size: 8 μm, bit depth: 14 bit). The camera is placed at a distance of 20 cm from the copper ring, and we image with a $f = 75$ mm lens, to get a magnification of $M = 0.46$ (i.e. we make the image smaller than the object). We implement to record the three images in the experimental sequence, and the resulting absorption image is created in LabVIEW after each run. The image can be saved and used for further analysis.

3.8 Copper ring properties

The ring itself is made from oxygen free copper (OFHC), with an inner radius of 7 mm, an outer radius of 12 mm and a thickness of 2 mm, the dimensions are summarised in Table 2.1. We are interested in the inductance and the resistance of the ring, both parameters are crucial for the calculation of the induced magnetic field to calculate the trapping potentials. The resistance also determines the heating of the ring. The ring dimensions are kept large, so that a large thermal mass is provided. With the resistance of the ring known, we can estimate the power in the ring during the induced current.

3.8.1 Inductance and resistance

A replica of ring 1 is used to determine the DC values of R and L. We start by measuring L/R, following the experiment described in [120]: an antenna produces an AC magnetic field of frequency f, which induces an EMF in a probe coil. The response of the probe coil to the antenna over the desired frequency range is measured with and without the inductor under test (ring 1) placed on top of the probe (electrically isolated). The ratio of the measured voltage with ring 1, V_{Ring},

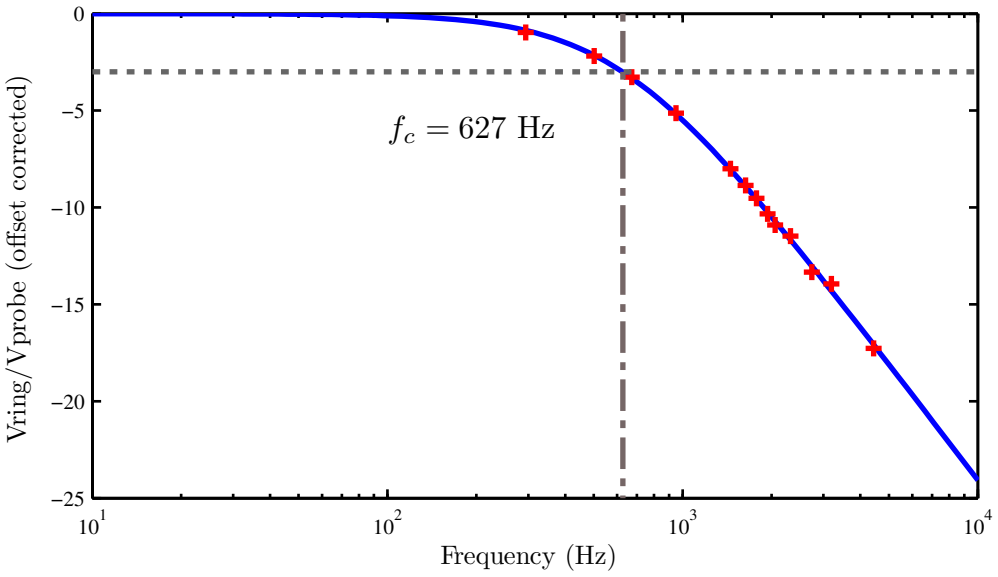

Figure 3.15: The frequency response (red crosses) of a probe coil subject to a AC magnetic field with frequency f is measured with and without the copper ring (ring 1) placed on top of the probe. The copper ring inductance is extracted from the cut-off frequency, f_c, obtained by fitting the transfer function (blue line).

to the probe voltage without ring 1, V_{Probe}, is then used to determine L/R by fitting the transfer function:

$$\frac{V_{\text{Ring}}}{V_{\text{Probe}}} = \frac{1}{\sqrt{1+(\frac{\omega L}{R})^2}} \tag{3.3}$$

$$= \frac{1}{\sqrt{1+(\frac{f}{f_c})^2}}\ , \tag{3.4}$$

with f_c being the cut-off frequency, which is extracted from the fit ($f_c = 627$ Hz), see Figure 3.15. The copper ring is then cut and R is obtained from a four-point resistance measurement to be 100 $\mu\Omega$. With R determined, the inductance is calculated from the cut-off frequency to be $L = 25$ nH. The AC values are estimated from finite element modelling, $R_{\text{AC}} = 440$ $\mu\Omega$ and $L_{\text{AC}} = 42.5$ nH.

3.8.2 Ring heating

With the given resistance, we can estimate the power dropped in the copper ring due to resistive heating. At the maximum induced current of 140 A – at $B_0 = 110$ G – we estimate that a power of 4.3 W is dropped in the ring. In fact, with an identical copper ring that is placed in the magnetic field of the AC coils (resting in air, not in vacuum), we measure temperatures of up to 100 °C within several seconds for the same AC drive field. This resistive heating leads to problems in the experiment: the constant exposure of the copper ring to large amounts of rubidium atoms leads to the formation of a rubidium layer on the copper ring. Heating the ring releases those rubidium atoms. As a result, higher atom numbers are counted in the ring trap after several runs with high AC drive fields.

In order to find "safe" parameters for the AC drive field, we test the impact of the heating, by measuring the MOT fluorescence with a photodiode after different AC drive field amplitudes, ring trapping times and number of runs.

From the fluorescence, we see that the high AC drive fields lead to higher rubidium pressure, even if several seconds of cooling time are added between runs. An example is shown in Figure 3.16, where we record the MOT fluorescence as a function of time while continuously running a cycle of 4 s AC field ($B_0 = 110$ G), followed by 4 s MOT load. With the dispensers off, we fill the MOT only with the released atoms from the copper ring, up to $N \approx 2.4 \times 10^8$. However, we find that a low amplitude magnetic field of $B_0 = 55$ G does not heat the ring enough to release atoms, and ring traps with this amplitude can safely be used. This influences our choice of parameters for the experiment, especially regarding analysis involving the atom number.

As additional safety measures against varying atom numbers in the experiment, the MOT loading time is increased to 8 s, after which it is saturated and less susceptible to a change in background atoms. The images are also normalised and the order of datapoints is randomised (e.g. for the lifetime measurement, where the atom number is measured as a function of trapping time) to prevent systematic errors where necessary (see also Section 4.2).

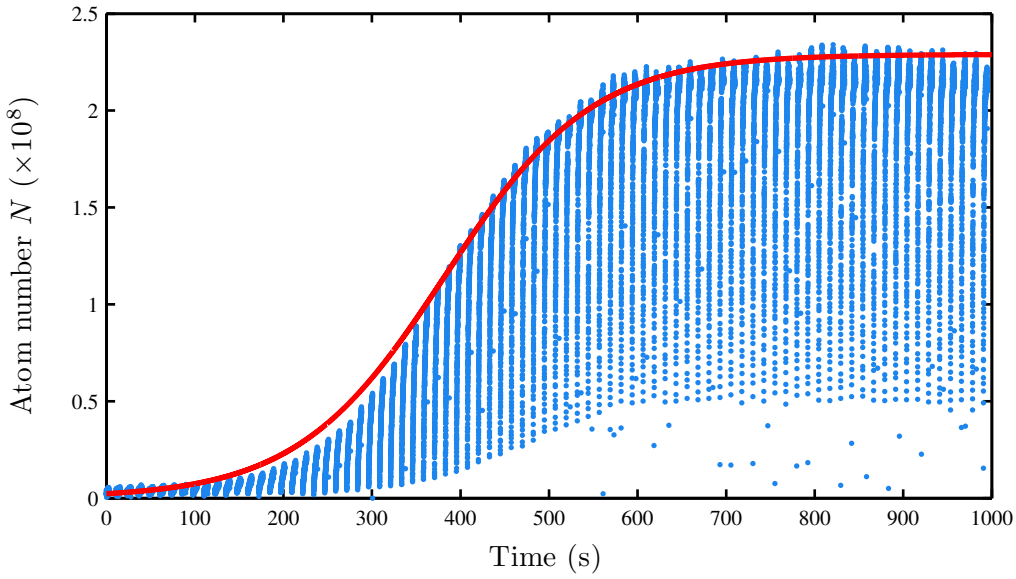

Figure 3.16: During the AC drive field, the induced current leads to resistive heating of the copper ring. This releases rubidium from the surface, enough to fill a MOT with $N \approx 2.5 \times 10^8$ atoms. Here, we cycle through 4 s AC field ($B_0 = 110$ G) followed by 4 s MOT load. A sigmoidal envelope function (red) is overlayed for clarity.

3.9 Remote control of the experiment

The software used for controlling the instruments is LabVIEW. One digital and one analog card are used to produce the desired output signals. These are distributed with a homemade breakout box. Each port has a BNC connections, which is used for applications (e.g. regulating current in the coils), some instruments have a built-in USB connection (e.g. Luca Andor camera).

3.10 Experiment sequence

In the different stages of the experiment, the cold atoms are transferred into the ring trap and then imaged. This can be divided into the following steps:

1. MOT

2. Molasses
3. Optical pumping
4. QP
5. Move QP
6. Ring trap
7. TOF
8. Imaging

In the next Sections, the individual steps – including typical settings – are described in more detail.

3.10.1 Step 1 - MOT

We begin the experimental sequence by capturing atoms from the background gas in a MOT, over a loading duration of 8 s. We optimise the MOT by adjusting the gradient, dB/dz, to $\sim$ 15 G/cm, which gives the highest atom number for the lowest current, see Figure 3.17 (a). The atom number also depends on the detuning, Δ, and we find the optimum at -18 MHz, see Figure 3.17 (b). Additionally, we adjust the power in the beams, by regulating the AOMs. As shown in Figure 3.18, we find a nearly linear increase of atom number with cooling light power, while it plateaus for repump light power. For highest atom number results, we use the 100 % of power available for the cooling and the repump light ($\sim$ 15 mW and $\sim$ 10 mW in total before the chamber, respectively). We measure the temperature of the atoms in the MOT to be 220 μK.

3.10.2 Step 2 - Molasses

From the MOT, the pre-cooled atoms are released into the optical molasses by switching off the QP field. During the 10 ms long molasses phase, the cooling and repump light power are ramped down exponentially to 40 % of their maximum value. At the same time, the detuning is increased to $\sim$ 50 MHz. With these

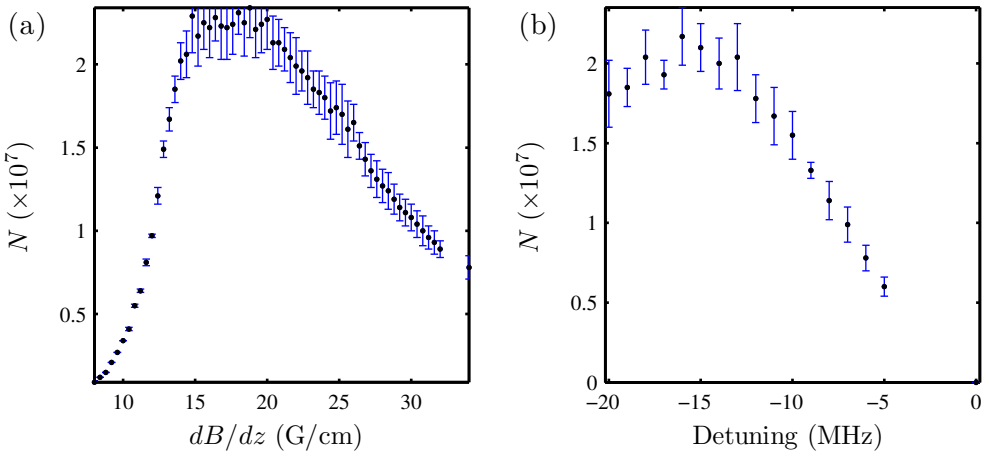

Figure 3.17: The MOT atom number is maximised for the MOT gradient (a) and the cooling light detuning (b).

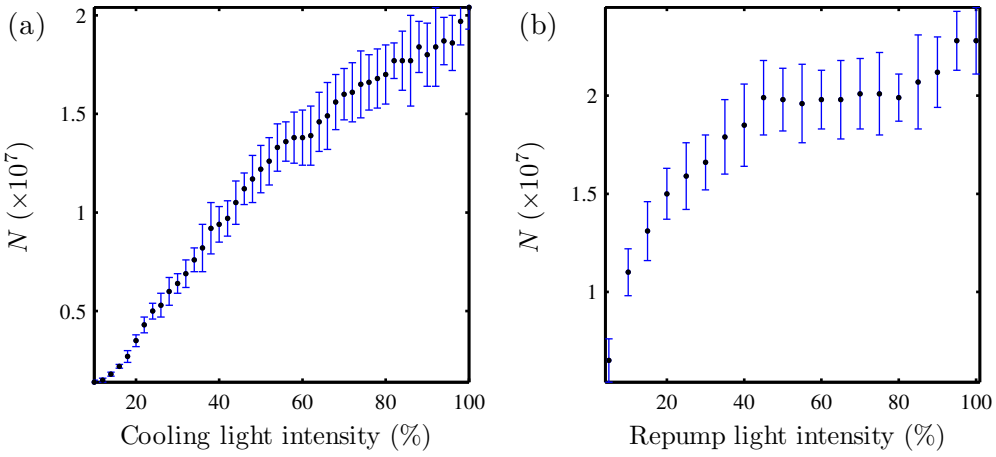

Figure 3.18: The MOT atom number is optimised by changing the laser power of the cooling laser (a) and the repump laser (b). At 100%, the total power in the beams before the chamber (before being split in the horizontal and vertical beams) is ~ 15 mW for the cooling light and ~ 10 mW for the repump light.

settings, we transfer basically all atoms into the molasses and sub-Doppler cool them to ~ 20 μK.

3.10.3 Step 3 - Optical pumping

For the optical pumping to work, we add a bias field of 3.4 G along the propagation direction of the optical pumping light (z) and $\sim$ 5 mW of repump light. A duration of 1 ms with $\sim$ 25 μK of OP light is sufficient to populate the $|F' = 2, m_F = 2\rangle$ state for magnetic trapping.

3.10.4 Step 4 - Load QP in MOT region

After the optical pumping, the atoms are captured in a QP trap, for which the gradient is increased to 32 G/cm over a duration of 10 ms. We transfer $\sim 85\%$ of the atoms from the MOT into the QP.

3.10.5 Step 5 - Move QP to ring region

While keeping the gradient constant, the QP trap is moved to the plane of the ring by changing the current in the MOT coils. The ratio is changed from $I_1/I_2 = 1.75$ to a $1:1$ ratio, thereby moving the magnetic minimum along z over a distance of 15 mm. The QP is moved slowly within 200 ms, followed by a waiting time of 20 ms, in which the QP trap is held still to damp residual oscillations induced by the transport. During the movement of the QP trap along z, we also apply a push field from the single coil along the EW direction, which shifts the QP to the side, towards the position of the ring trap, rather than the centre of the ring.

Quadrupole trap as reference for ring trap When characterising the ring trap it is useful to relate it to the characteristics of the QP trap. The QP provides a reference point and is useful for optimisation of the ring trap parameters. Seeing the differences of properties such as temperature or lifetime between the ring trap and the QP trap also provides the means to identify additional loss or heating mechanisms (e.g. by comparing the ring lifetime to the vacuum limited lifetime of the QP trap). We trap $\sim 5 \times 10^6$ atoms in the QP, but the atom number

varies with Rb vapour pressure in the cell. The QP temperature is 42 ± 3 μK (statistical uncertainty), and we measure a lifetime of $\tau_{QP} = 1.3 \pm 0.3$ s. An absorption image of atoms in the QP trap at the ring loading position is shown in Figure 3.19, together with an example of QP profiles for different times of flight and their Gaussian fits.

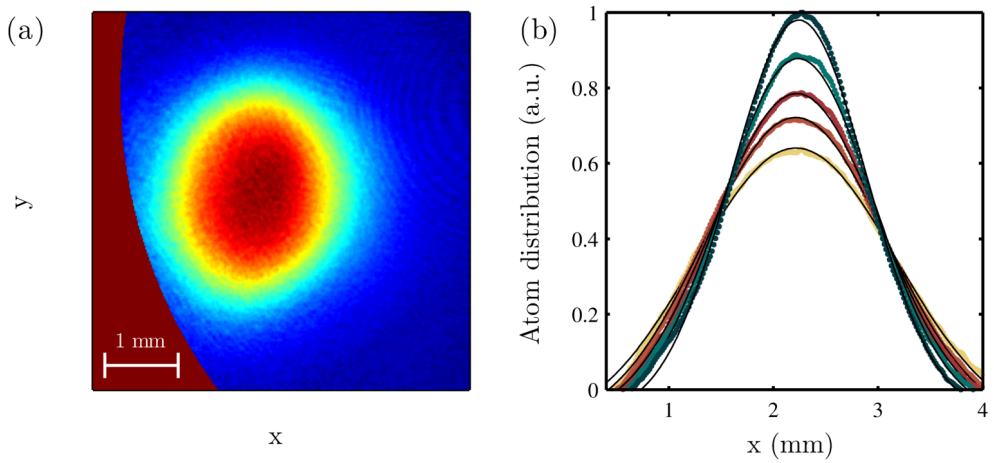

Figure 3.19: (a) Absorption image of atoms in the quadrupole trap at the ring loading position. The red region on the left is a mask we apply to discard scatter from the copper ring, see Section 4.1. (b) The corresponding atom distributions along the x-axis for different time of flights after being released from the QP trap. The x-axis corresponds to the axis of the image in (a), and the atom distribution is normalised to the maximum column density in the shortest time of flight.

3.10.6 Step 6 - Ring trap

After 0.5 ms of waiting time for the QP coils to switch off, we apply the two magnetic fields that create the ring trap: the AC drive field and the bias field. We can see atoms filling the ring, an image is shown for the ring trap after 150 ms in Figure 3.20 (a). The ring trap duration, t_r, can be varied, to study the lifetime and the evolution of atoms in the trap. A measurement of the atom number with increasing ring trapping time is shown in Figure 3.20 (b), where we can see atoms in the ring after more than 1 s (the lifetime is discussed in greater detail in Section 5.2.3).

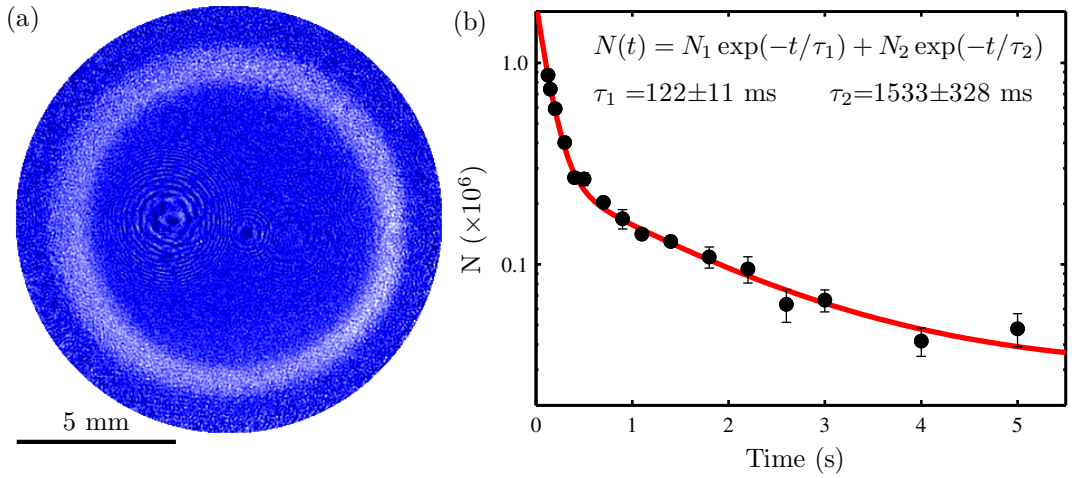

Figure 3.20: (a) Atoms are successfully trapped in the ring. (b) We measure the atom number as a function of the ring trapping time, and find that we can trap atoms for over 1 s.

3.10.7 Step 7 - TOF

To image the atoms and to gain information about their temperature, we adjust the time of flight (the time in which the atoms are unconfined and free falling after the trap has been switched off). Due to the AC magnetic fields, we have to implement a minimum waiting time ($\sim$ 3 ms) to let the AC magnetic fields ring off, otherwise the imaging light is be out of resonance.

3.10.8 Step 8 - Imaging

The absorption image is the result of a sequence of three images, each of which has a duration of 50 μs, with a dark phase of 10 ms inbetween. We need low power in the probe beam to not saturate the camera, $P_{\text{Probe}} \approx 30$ μW. To image the atoms along their projection axis, we apply the same magnetic bias as during the ring trap and adjust the probe beam detuning to be in resonance with the Zeeman shifted imaging transition.

Chapter 4

Methods of analysis

Each run of the experiment ends with an absorption image of the atoms, and we have to extract the relevant information from it to be able to characterise the ring trap. This short Chapter explains how we perform the data analysis. We record images with a size of 1000×1000 pixels, corresponding to an imaging region of about 1.7×1.7 cm, thus imaging the whole region enclosed by the copper ring. For the ring trap characterisation, for which we use quantities such as atom number, temperature and trap lifetime, we mainly monitor the atom number and the spatial distribution of the atom cloud. This information is accessible with the optical density (OD) in the absorption images, spatially resolved in the x and y-dimension.

4.1 Region of interest

Not all areas of the image are important for the analysis – on the contrary, including atom-free regions in the analysis can increase statistical errors due to imaging imperfections. Restricting the analysis to the relevant region will therefore help to reduce errors. Noise or scatter in the image can also disguise information about the atoms or influence the image scaling. We therefore create a "region of interest" on which to apply our analysis, which is defined by different masks applied to the image, as shown in Figure 4.1. As an example, imaging light is scattered by the copper ring during absorption imaging, which produces unwanted bright

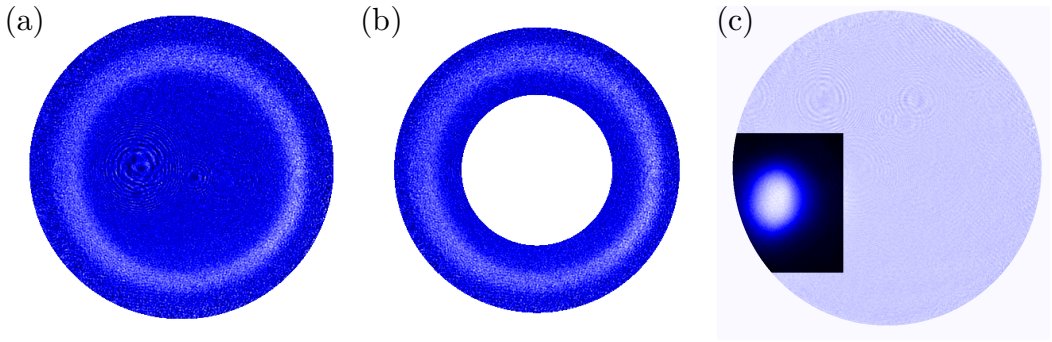

Figure 4.1: Different masks are applied to the image to define the region of interest on which the data analysis is performed. (a) The first, circular mask (Mask 1) removes the scattered light of the copper ring. (b) The second mask (Mask 2) is smaller, it restricts the region of interest to approximately the width of the ring trap. The white region in the ring centre is used for background corrections. (c) When the QP trap images are analysed, the second mask is rectangular around the QP. The region outside the rectangle is used for background correction, here shown in pale blue.

spots on the images. To get rid of the scatter on the images, a mask is applied (Mask 1) that discards the pixels affected by it, so that only the region inside the copper ring is shown. This region is a circle with a radius corresponding to slightly less than the inner radius of the copper ring. It is applied for the ring trap images, as well as the QP trap images. For the ring trap images, we restrict the region of interest further: an additional mask (Mask 2) removes all pixels in the centre of the image. The radius of this circular region can be adjusted for different ring traps, to always have a radius small enough to lie outside the the ring trap. This circular region in the centre is the "background region" and it is used for background correction when calculating the atom number. For the QP trap images, a rectangular mask enclosing the atoms in the QP cloud is applied, everything outside that rectangle (not counting the region already discarded by Mask 1) is used for background correction. By using these masks, imaging imperfections, such as the circular pattern due to optical imperfections in Figure 4.1 (a), can be excluded from the analysis.

4.2 Atom number

One of the most important pieces of information is the atom number, N: it tells us how well we can transfer the atoms into the trap, and we can extract the lifetime, τ, by measuring the atom number as a function of time. The number of atoms in the image is proportional to the optical density (OD), which is stored as the brightness of the absorption image (see Section 3.7), and can be calculated via [60]:

$$N = \frac{A}{\sigma_0} \cdot \sum OD \ , \tag{4.1}$$

where A is the area per pixel and $\sigma_0 = \frac{3\lambda^2}{2\pi}$ is the resonant cross-section for a two-level atom [60]. With our imaging system, we have a pixel area of $A =$ (pixel size/magnification)^2 = (8 μm/0.46)$^2 \approx 3 \times 10^{-10}$ m^2 and a cross-section of $\sigma_0 = \frac{3\times(780\ \text{nm})^2}{2\pi} \approx 3 \times 10^{-13}$ m^2 which leaves us with the conversion

$$N \approx 10^3 \cdot \sum OD \tag{4.2}$$

for the total number of atoms in the image. The sum of the OD is obtained by adding the brightness of all pixels within the relevant region of the image (within Mask 2) and then background correcting it, using the information from the background region (the average background brightness per background pixel is calculated, scaled by the region of interest and subtracted from the OD).

Although the total atom number is calculated in LabVIEW and can be read off after each shot, most data is post-analysed. This has the advantage of first recording and then analysing large sets of data at once (e.g. for a lifetime measurement). We generally use average images of $5-10$ single shots to improve the signal-to-noise ratio and to obtain the atom number uncertainty from the standard deviation. For measurements where the atom number is important, we also record normalisation data to be able to dismiss obviously faulty data (e.g. due to unlocked lasers) and to check for systematic errors (e.g. increasing atom numbers due to ring heating): for each single data shot, one normalisation shot is taken immediately afterwards. In most cases, an image of the QP trap is used for normalisation, as it provides a stable measurement of the atom number independent of ring trapping parameters.

4.3 Lifetime

The lifetime of a trap, τ, is a very important property, which tells us how well we can trap the atoms. The main cause for atom losses are collisions with the background gas, expelling the atom from the trap through momentum kicks and spin-flips, which cause an exponential decay of the measured atom number:

$$N(t) = N_1 \exp(\frac{-t}{\tau_1}) \ , \tag{4.3}$$

where N_1 is the initial atom number and the time constant τ_1 is the lifetime of the trap. The background loss rate is expected to be the same for all traps (QP and ring trap) in the same vacuum setup with constant background pressure.

In our ring trap, we have to account for another loss mechanism: the magnetic zeroes move into the outer regions of the ring trap and cause the highest energy atoms to spin-flip, those Majorana losses decrease the atom number further. Because the timescale of Majorana losses is much faster than the timescale of collisional losses, we need a two-part decay for the ring trap atom number when measuring the lifetime:

$$N(t) = N_1 \exp(\frac{-t}{\tau_1}) + N_2 \exp(\frac{-t}{\tau_2}) \ , \tag{4.4}$$

where N_1, N_2 are the atom number scaling factors for the different loss mechanisms, and τ_1, τ_2 are their respective lifetimes.

For the QP trap on the other hand, it is the atoms at low energies that are most affected by Majorana losses (compare Section 2.1). The temperature of the atoms in the QP is too high for Majorana losses to be significant, and we find the single exponential decay to be a good fit to extract the lifetime.

4.4 Temperature and trap frequency

The temperature and the trap frequency can both be obtained from a time of flight measurement [20, 43, 44], where an image of the cloud is taken for different times of flight, t_{tof}, (the time between being released from the trap and the image) and the width of the cloud is measured. The velocity distribution of the atoms

will lead to expansion of the cloud with time of flight, which is measured as an increase in cloud width, σ, thereby giving us information about the cloud temperature, T. If we assume a harmonic trap potential near the trap bottom, we can also infer the trap frequency, ω, from this measurement.

It is important to mention that we use a time of flight method which makes three assumptions:

1. We assume a Boltzmann distribution of the atoms' velocity.

2. We approximate the potential with a harmonic potential (in 1D):

$$U = \frac{1}{2} M_{\mathrm{Rb}} \omega^2 x^2 \ , \tag{4.5}$$

   to get a Gaussian spatial distribution.

3. We assume a Boltzmann distribution of atoms in the potential (in 1D):

$$n = n_0 \exp(\frac{-U}{k_B T}) \ , \tag{4.6}$$

   where n is the atom number density, U is the potential, k_B is the Boltzmann constant and T is the temperature.

We are aware that these assumptions are not always fulfilled when regarding the ring trap: as discussed previously (Section 2.2.2), we do not have a Boltzmann distribution of velocity in the ring trap once the magnetic zeroes remove atoms with (radially) high velocity without re-thermalisation. This has important implications for the temperature: it means that we can only speak of an *effective radial temperature*, treating the atom cloud as if it was re-thermalised while being aware that it does not correspond to the actual cloud temperature. The second approximation holds problems as well: the harmonic approximation can be applied for the bottom of the ring trap potential with $B_z = 0$ (see Section 2.2.1), but is ceases to be appropriate for increasing bias fields, which flatten the bottom of the trap. This will cause problems primarily for the calculation of the trap frequency. Finally, the assumption for the Gaussian radial distribution of atoms in the trap starts to break down for increasing B_z, making it difficult to fit the

cloud appropriately with Gaussian functions. The reason why we are nevertheless using this method is that the information is easily accessible, and we don't need to know more than what we can gain from it. Additionally, the second generation ring trap will confine atoms in a BEC, which means that the atoms will be ~ 100 times colder, and they won't interact with the magnetic zeroes as much, meaning that we don't need to worry about a cut-off velocity distribution. However, even the effective temperature will depend on the position of the magnetic zeroes and therefore on B_z, and it will provide an interesting parameter when characterising the different ring trap configurations. The temperature analysis also helps us to compare our understanding of the trapping potential from simulations with experimental results.

With the given assumptions, we can measure the cloud's width as a function of time of flight and get the temperature from the expansion. The trap frequency together with the temperature determines the atom cloud's initial width, σ_0, which can be extrapolated from the time of flight data. We have a linear relationship between the square of the cloud width and the square of the time of flight for sufficiently large t_{tof}, from which we can find the slope

$$\frac{d\sigma^2}{dt_{\mathrm{tof}}^2} = \frac{k_B T}{M_{\mathrm{Rb}}} \ , \tag{4.7}$$

from which the temperature is extracted, and the intersection

$$\sigma_0^2 = \frac{k_B T}{M_{\mathrm{Rb}} \omega^2} \ , \tag{4.8}$$

which gives us the trap frequency (see Appendix C for more details).

Measuring the cloud width The width of the atom cloud is measured by fitting a Gaussian to the atom number profile along one axis, using the Gaussian width, σ, as the cloud width. To get the 1D-profile, the absorption image is integrated over one axis: for the QP trap the image is integrated over x to get the y-profile and calculate T_y, or integrated over the y-axis and the x-profile fitted with a Gaussian to get T_x. For a QP, T_x and T_y are approximately equal.

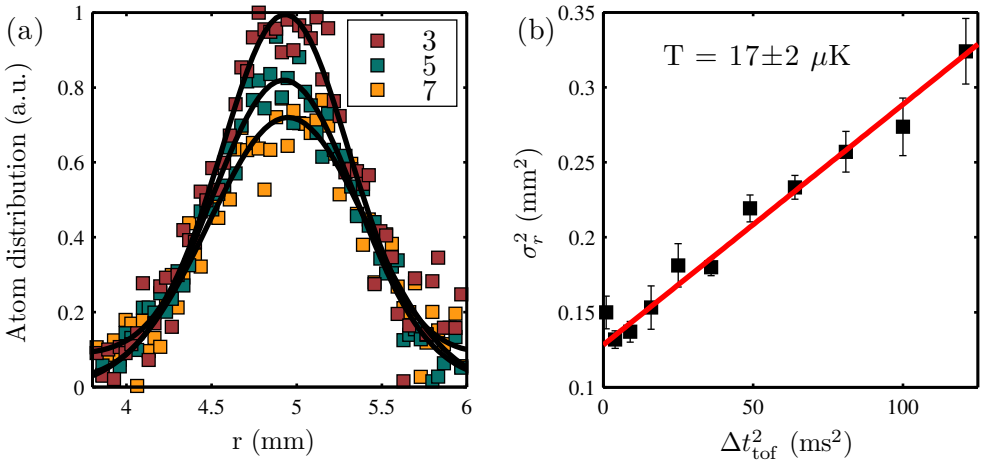

Figure 4.2: (a) Example of radial atom distribution at $B_0 = 55$ G, $B_z = 3.4$ G, for $t_{\rm tof} = 3, 5$ and 7 ms with their Gaussian fits and (b) the resulting temperature fit.

Regarding the ring trap, we are interested in the radial and the azimuthal temperatures and in the radial trap frequency (there is no azimuthal confinement). Therefore, the ring trap image can be binned azimuthally or radially, by transforming the image x-y–coordinates into a discrete set of polar coordinates (with N_ϕ triangular sections of width $d\phi$ and N_r circular sections of width dr), so that we obtain radial and azimuthal temperatures and trap frequencies. An example of radial atom distribution with the corresponding Gaussian fits and the resulting temperature fit is shown in Figure 4.2.

4.5 Trap geometry

The spatial resolution in x and y of the absorption images allows us to characterise the ring trap in terms of its geometry, namely the radius and the width of the trap. Because the atom distribution is greatly affected by the location of the magnetic zeroes and by the shape of the trapping potential at the trap bottom, the trap geometry changes with B_z, which pushes the zeroes out and flattens the trap bottom, and by B_0, which determines the trap strength and the effect of gravitational sag on the atoms. To map out the trap geometry as a function

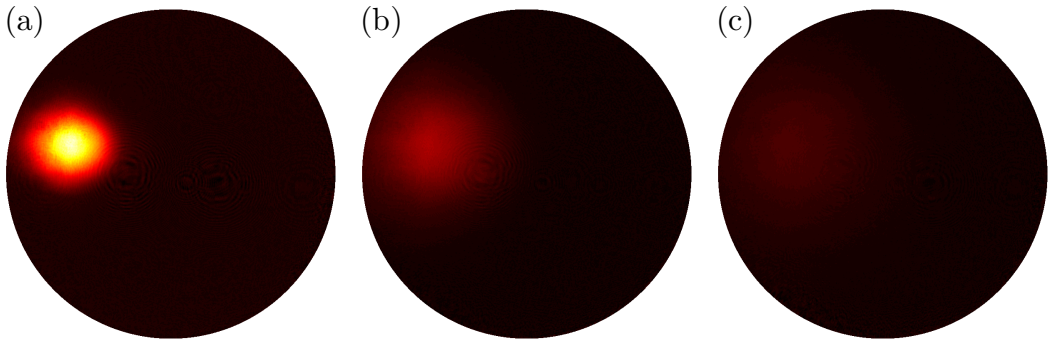

Figure 4.3: Cloud of atoms falling free under gravity after being released from the QP trap for t = 10 ms (a), 30 ms (b) and 50 ms (c). The atom cloud gets dimmer and finally vanishes from the imaging region for times t > 80 ms.

of B_0 and B_z, the mean trap radius and the trap width are determined from a Gaussian fit to the radial profile of a ring trap absorption image.

4.6 Additional information

There are a few additional things to consider when taking ring trap data:

1. We can see a cloud of untrapped atoms fall away within the first 80 ms and we take care to use trapping times long enough ($t_r \geq 100$ms) such that the image is clear of any of residual falling atoms. Figure 4.3 shows the cloud of atoms after being released from the QP, without switching on the ring trap.

2. To avoid systematic errors of the atom number (due to increasing Rb pressure) we take data in random order and use averages.

3. Because of the changing trap geometry, it is necessary to re-optimise the radial and z-position from which the atoms are loaded into the ring trap, whenever B_z is changed.

4. Despite the attempts to clean all optics as well as possible, fringes and spots appear in the images, adding to noise in the atom number calculation. While some of the fringes can be removed by applying a Fourier

transform to the image and deleting selected frequencies, we rely on averages and background correction to minimise the effect of the remaining image disturbances.

Chapter 5

Results

In this Chapter I describe how we have successfully created an inductively coupled magnetic ring trap for cold atoms, resulting from the superposition of different magnetic fields: an AC drive field and an induced magnetic field, which create a toroidal magnetic minimum, plus a bias field to offset magnetic zeroes at the potential minimum, which is crucial to avoid Majorana losses. We can shape the geometry of the ring trap with the bias, creating ring traps with different radii, width and trapping properties. A first attempt to apply a tangential bias field creates a semi-circular trap, which is unstable due to a high atom loss rate at the remaining regions of zero magnetic field. We briefly present the properties of the semi-circle in Section 5.1. We then focus on the properties of the stable ring trap for which an axial bias field is applied (perpendicular to the plane of the ring), the results for different traps, making use of the effect of the bias field strength, are presented in Section 5.2.

5.1 Tangential bias

Adding a magnetic bias along the plane of the ring offsets the magnetic zeroes in all but two regions, where the vector components of the induced field and the bias field are opposing. This produces two non-adiabatic regions with very low magnetic field at opposite points within the ring potential (along the bias field axis), allowing the atoms to spin-flip and escape. Although the potential

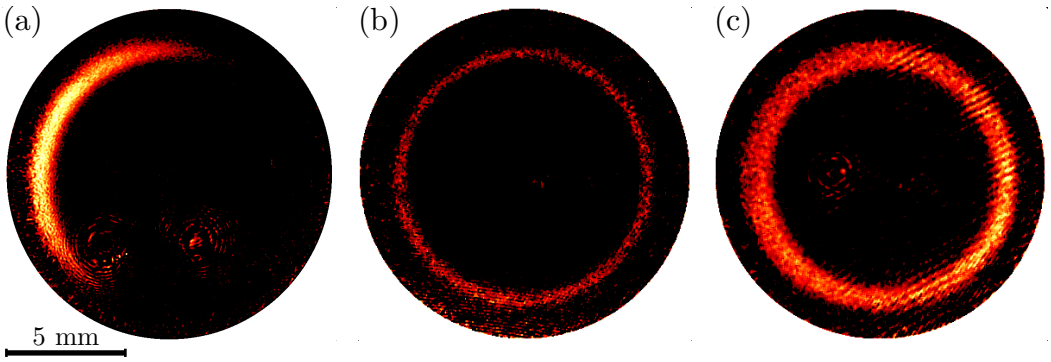

Figure 5.1: Three different traps: (a) semi-circular trap from tangential bias, (b) thin ring from low axial bias and (c) thick ring from high axial bias. The images are cut to the inner diameter of the copper ring.

does not confine the atoms at every point, we can still gain information about the ring trap. We apply a tangential bias $|B_t| \approx 1.1$ G to create a semi-circular ring trap, the result is shown in panel (a) of Figure 5.1. Depending on the direction of the magnetic field and the loading position of the atoms we can create the semi-circular trap at different positions within the ring. Here we have applied a magnetic field along the diagonal of the ring and loaded the atoms at the left hand side. An important property of the semi-circle is that the radial temperature is $T_t = 40 \pm 3$ μK, the same as the QP temperature within the uncertainties ($T_{\mathrm{QP}} = 42$ μK). This implies that neither the ring itself nor the transfer induce heating and the potential is adiabatic, apart from the positions around the magnetic minima. These "holes" make the trap unstable and short lived: the lifetime is 80 ms. Although we might expect a different behaviour of the atom number, (e.g. a linear decay) due to the zeroes, where the atoms could leak out at a different rate, the exponential decay agrees well with the data, see Figure 5.2. In order to study the trap further, we attempt to increase the lifetime by incorporating barriers for the atoms before they reach the trap holes. Using a strong, blue-detuned laser (215 mW at 771 nm) we form two elliptical beams that slice through the atoms, maximising the potential barrier by focussing the beams to a width of 9 μm and a corresponding Rayleigh length of 0.4 mm, while keeping the other axis long enough (250 μm) to go through the whole width of the ring

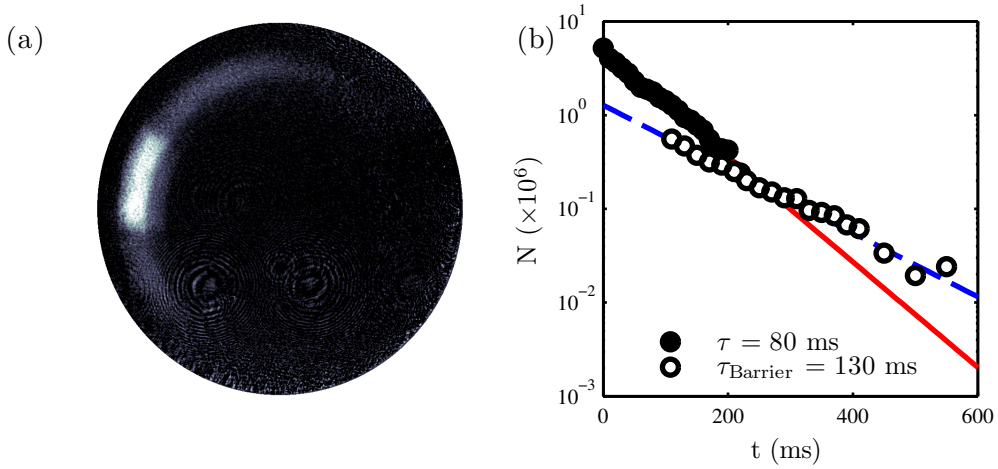

Figure 5.2: (a) Image of the semi-circular ring trap with tangential bias and dipole barriers. (b) The lifetime of the tangential bias ring trap with and without barriers. The lifetime, τ, is only slightly improved by the barriers.

trap. The barriers are clearly visible as dark stripes enclosing a bright area in Figure 5.2, and we observe a slight increase in atom number, indicating that the barriers do stop atoms from spilling out. But we can also see the (much fainter) tail of atoms that are not stopped by the barriers and that are filling the ring, and we do not have a perfectly sealed trapping region. This agrees with the lifetime we measure (by taking into account only at the atoms in the region enclosed by the barriers): compared to the lifetime of the semi-circle without barrier, the lifetime improves from 80 ms to 130 ms. Even with the barriers this ring is very short lived compared to the lifetime of the QP, and it is not sufficient for looking at inherent features of the ring trap or to use it for atomic physics experiments. We conclude that the dipole barriers do not work as well as we hoped, because the atoms find ways around the barriers due to insufficiently large barriers that do not cover the whole ring width and height (along y and z). Additionally, the atoms scatter light from the laser and might be expelled from the trap. Hence, we don't have a satisfying way to study the ring trap with a tangential bias any further and continue with characterising the ring trap with axial bias.

5.2 Axial bias

We create a stable ring trap with an axial instead of a tangential bias. The axial bias creates a region of non-zero magnetic field at the trap minimum, and we observe that the properties of the trap depend on the strength of the bias field. Under this aspect, we characterise the ring trap with regards to the following:

1. Trap geometry
2. Atom number
3. Lifetime
4. Temperature
5. Trap frequency
6. Dynamics (atom evolution)

The following Sections will present the results for each of the above points. In the experiment, we restrict ourselves to taking data for a magnetic drive field strength of $B_0 = 55$ G wherever possible (at the cost of slightly less signal amplitude), to avoid rubidium release from the copper ring due to resistive heating for high induced currents (see Section 3.8.2). For the analysis, we use the methods described in Chapter 4. We find that most trap characteristics are in agreement with our expectations from the calculated magnetic potential in Section 2.2, over the range we can explore them without being limited by signal-to-noise or invalid methods of analysis.

5.2.1 Trap geometry

By applying different bias fields B_z we change the geometry of the ring trap, which can be clearly seen in the pictures of Figure 5.1: we create a thin trap for low B_z, which widens when the bias field strength is increased. We also find that the mean trap radius changes with B_z. The ring trap is therefore tunable over a range of position and width. With our trap, we can tune the radius from 5.3 to 4.3 mm and the width from 0.3 to 0.8 mm (from low to high B_z), see

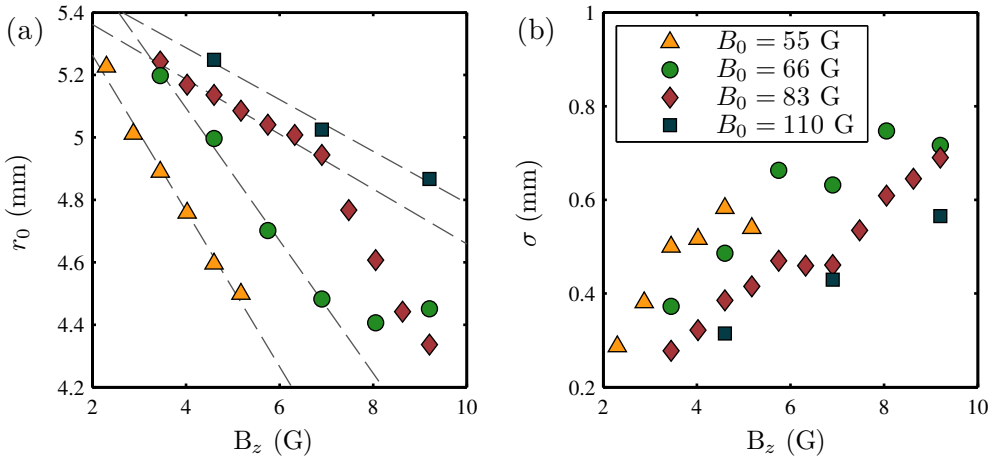

Figure 5.3: Mean radius (a) and Gaussian width (b) of the ring trap for different B_0 and B_z. The trap gets smaller and it widens for increasing bias field.

Figure 5.3. The change in geometry can be explained by two effects: firstly the spatially dependent removal of atoms due to the magnetic zeroes and secondly the shifting and flattening of the trap bottom. The magnetic zeroes affect the spatial distribution of atoms, because the trap is tightest at the bottom of the potential and looser at higher energies (which is shown in the potential simulations), leading to a thin trap when the magnetic zeroes come close to the magnetic minimum for low B_z. As the magnetic bias field pushes the zeroes out, the trap bottom is lifted, so that the atoms are trapped in a looser potential and the spatial atom distribution becomes wider. Additionally, the trap bottom is flattened, which is reflected in a flatter (non-Gaussian) atom distribution and the trap appears wider. Due to the wine bottle shape of the potential and its steep outer edge, the atom cloud extends more towards the (shallower) centre of the ring, leading to a smaller mean radius. The trap radius and the trap width as a function of B_z shown in Figure 5.3 are obtained from the width and the peak position of the Gaussian fits for traps with $B_0 = 55,\ 66,\ 83$ and 110 G. We observe that the trap radius changes linearly: there is one regime with a steep gradient (-0.2 mm/G) for weaker traps ($B_0 = 55$ and 66 G data) or stronger B_z (for $B_0 = 83$ G) and one regime with a lower gradient (-0.08 mm/G) for stronger traps ($B_0 = 83$, low B_z and 110 G data), shown as dashed lines for each B_0 dataset. The gradients

will depend on the exact potential shape and its change as function of position. Additionally, gravity will lead to sagging toward the ring centre, more so for weaker traps. There is no good fit to the trap width as a function of B_z, but we do see a stronger increase in trap width for weaker traps, which is expected from the looser potential towards the ring centre. Having control over the trap geometry makes it versatile and suitable for different applications. We will show the evolution of the atom cloud in two different geometries in Section 5.2.6.

5.2.2 Atom number

The fraction of atoms transferred from the QP trap into the ring trap depends on the mode matching between the two traps and, as we can see from the trap simulations, the trap changes with the two magnetic field parameters that are involved in creating the trap, B_0 and B_z. With increasing B_z the magnetic zeros are pushed further away from the trap minimum, at the same time the trap becomes flatter and less harmonic. When applying B_z above a threshold bias we therefore expect the atom number to increase due to a more adiabatic trap until it reaches a maximum atom number after which the trap becomes too shallow and atoms are increasingly lost. The balance between the two effects is what we see when map out the atom number for B_0 and B_z. We measure the atom number after a fixed trapping time of $t_r = 200$ ms for a given B_0 while varying the bias field B_z from 0.6 to 9.2 G in steps of ~ 0.6 G. We then change B_0 to get the same curve for different drive fields between 44 G and 110 G (both magnetic fields are limited mainly by heating: coil heating for B_z and amplifier heating for B_0). From the recorded atom number, which is shown in Figure 5.4, we observe the following behaviour:

- The atom number approximately follows a Gaussian curve with B_z, slightly plateauing in the decay.
- For each B_0 there is a B_z that results in maximum atom number. We ascribe this to the minimisation of atom losses due to zero crossings and trap flattening at those magnetic fields, this magnetic field combination produces a trap which is optimum mode matched with the QP trap.

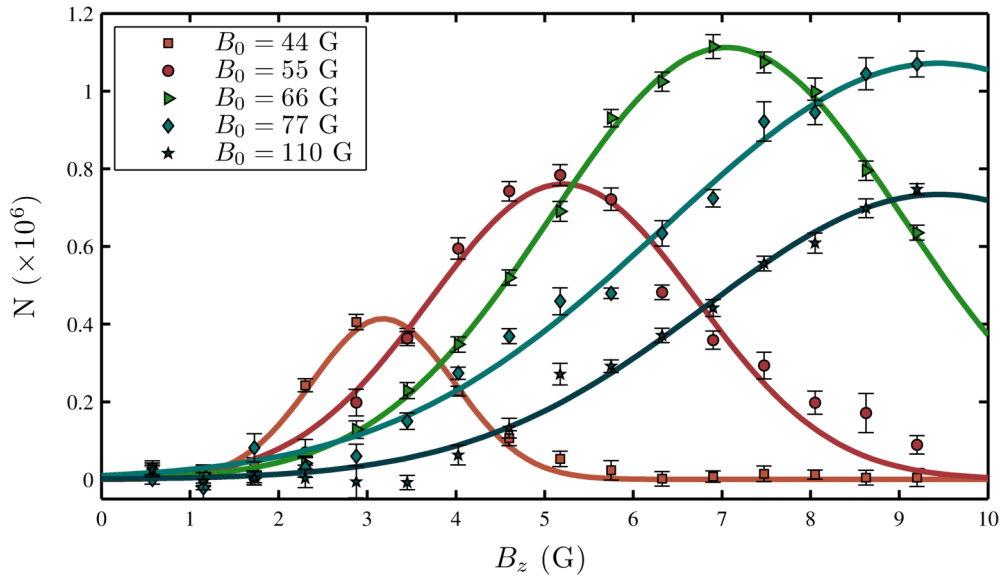

Figure 5.4: Atom number profile as a function of the bias field, for different magnetic AC drive fields. Each curve is fitted with a Gaussian. Error bars are one standard deviation from statistical uncertainties.

- The absolute atom number increases with B_0.
- The curves for $B_0 = 77$ G and 110 G are incomplete and convincing analysis of the Gaussian fits can not be made.

From the above observations we construct a phenomenological model of atom number as a function of the magnetic drive and bias fields. We introduce the parameter ξ:

$$\xi = (B_0 - c)/(m \cdot B_z) \ , \tag{5.1}$$

where $m = 5.6$ and $c = 26$ G are extracted from a linear fit of the bias field B_z that results in the maximum atom number for a given B_0, as shown in Figure 5.5 (a). We find that the normalised atom number, $N/N_{\max}$, scales universally with ξ. Figure 5.5 (b) shows the normalised atom number as a function of ξ, and we can see that the curves for different B_0 overlap (the curve for $B_0 = 110$ G is not included, because it lies outside our accessible range for B_z so that we can't get a good fit to the atom number distribution). Where $\xi = 1$, the atom number is

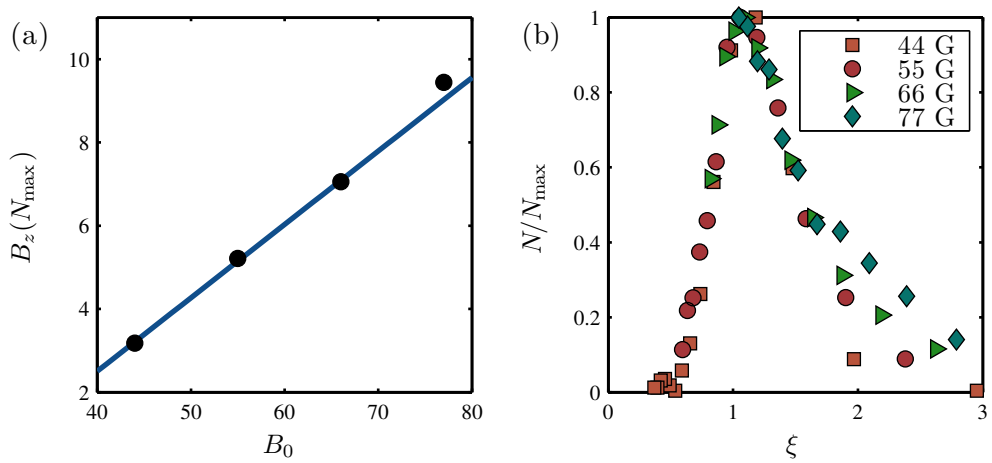

Figure 5.5: Constructing the scaling law: (a) the value of the bias, B_z, that gives the maximum atom number as a function of drive field strength, B_0. We obtain a linear fit, from which we infer the magnetic field scaling number, ξ (see text). (b) The normalised atom number, $N/N_{\max}$, is plotted as a function of ξ for different B_0 (see legend). The overlapping curves show the global scaling of atom number with B_0 and B_z.

highest, due to the magnetic fields producing optimum mode matching between the QP trap and the ring trap.

While at the moment we trap around 10^6 atoms, a denser cloud and higher magnetic fields could potentially increase the atom number.

5.2.3 Lifetime

Due to different loss mechanisms, the atom number in the trap decreases with a two-part decay to which Equation 4.4 is fitted, providing us with the two loss timescales, τ_1 and τ_2.

To characterise the different ring traps (thin and thick), we record data for $B_0 = 55$ G (low B_0 to avoid copper ring heating) while varying B_z. The results for τ_1 and τ_2 are summarised separately in Figure 5.6; we find τ_1 to be of the order of 200 ms and τ_2 to be around 1.3 s. The slow decay (τ_2) is of the same order as the QP lifetime and we therefore assume the same loss mechanism, i.e. atoms colliding with the background gas. We do not expect τ_2 to change with

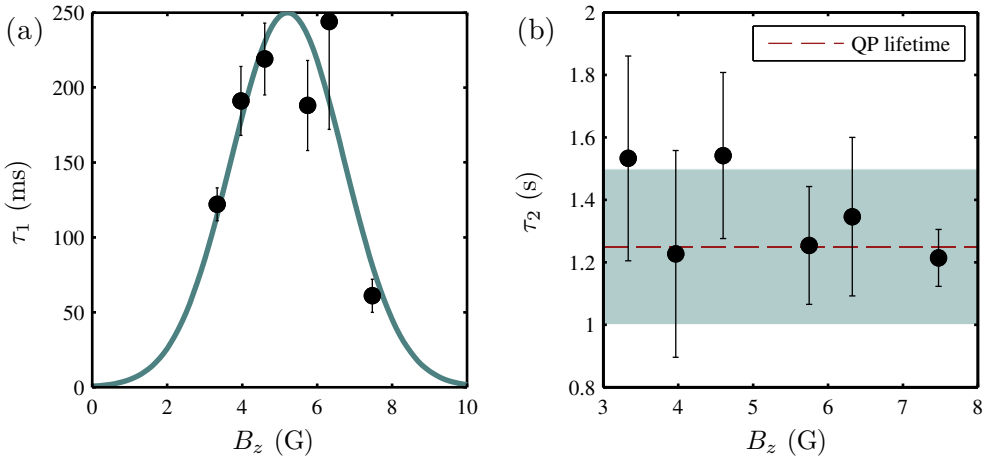

Figure 5.6: (a) Short trap lifetime τ_1 for $B_0 = 55$ G for different values of B_z. The normalised atom number profile from Figure 5.4 is added to guide the eye and to show a possible connection. (b) Long lifetime τ_2 for $B_0 = 55$ G. The QP lifetime is indicated with the red line, the shaded area is the QP lifetime uncertainty.

the trap configuration, and we find it to be constant within the uncertainties for different B_z. The short lifetime τ_1 on the other hand, which we ascribe to Majorana losses when the atoms encounter the "circle of death", is changing with B_z, first increasing from 120 ms to around 220 ms, then plateauing and finally dropping to 60 ms for the largest value of B_z. To gain an understanding of the mechanism behind these fast initial losses, Figure 5.6 shows τ_1 with varying B_z (normalised to the maximum value of τ_1), plus the Gaussian curve for the atom number $N(B_z)$ at $B_0 = 55$ G (curve from Figure 5.4, also normalised to its maximum value). Although the atom number curve is mainly added as a guide as to where on the magnetic field combination the measurement is taken (i.e. thin or thick ring trap), it is also interesting to see that τ_1 roughly follows it. The connection can be explained by making stronger Majorana losses for lower B_z responsible for smaller τ_1 (the magnetic zeroes spend more time at the position of the atoms), which corresponds to the beginning of the curve. The steep drop of the last measured τ_1 – for the highest B_z – actually corresponds to a potential already at the limit of trapping atoms in a ring, because it is so flat and shallow. We suspect that the gravitational sag then brings the atoms into the region of

magnetic zeroes. For an ideal, infinitely steep trap that does not flatten with B_z, we would expect the short lifetime to steadily increase, up to the value of τ_2.

The lifetime measurements show that if we find a way to drastically reduce the Majorana losses, our trap is limited by the vacuum lifetime of ~ 1.3 s (bearing in mind that any additional loss mechanisms slower than that are not measured with the current setup). One way to reduce Majorana losses is to cool the atoms further. This means that we can expect the lifetime for a BEC in the ring trap to be of the order of τ_2.

5.2.4 Temperature

As explained in Section 4.4, the radial velocity distribution in the ring trap is affected by the magnetic zeroes crossings, where the highest energy atoms of the thermal distribution are expelled without re-thermalisation of the cloud. The combination of the QP temperature and the Majorana cut-off temperature will result in the effective radial temperature of the ring trap, the results of which are shown in the next Section. The azimuthal temperature on the other is not directly affected by the radial magnetic zeroes, but we cannot exclude a connection between the velocity distributions in r and ϕ.

5.2.4.1 Radial temperature

We have already measured the temperature in the ring without zero-crossings when we applied the tangential bias instead of B_z, which came out to be the same temperature as the QP (Section 5.1). The Majorana-cut-off changes the temperature drastically, the results are summarised in Table 5.1 and plotted in Figure 5.7. As for the lifetime, we overlay the results with the normalised Gaussian fit to atom number for $B_0 = 55$ G from Figure 5.4 for comparison. Unfortunately, we can not measure T for all ring trap configurations: the spatial distribution for thick ring traps is not Gaussian, and no trustworthy fits can be made. While a numerical analysis might be possible using the correlations in [44], it is not scope of this work. For thin to intermediate ring traps, T first increases and then drops with B_z, so that T has similarities to the atom number curve, but does not follow the curve over B_z directly. The rise in T can

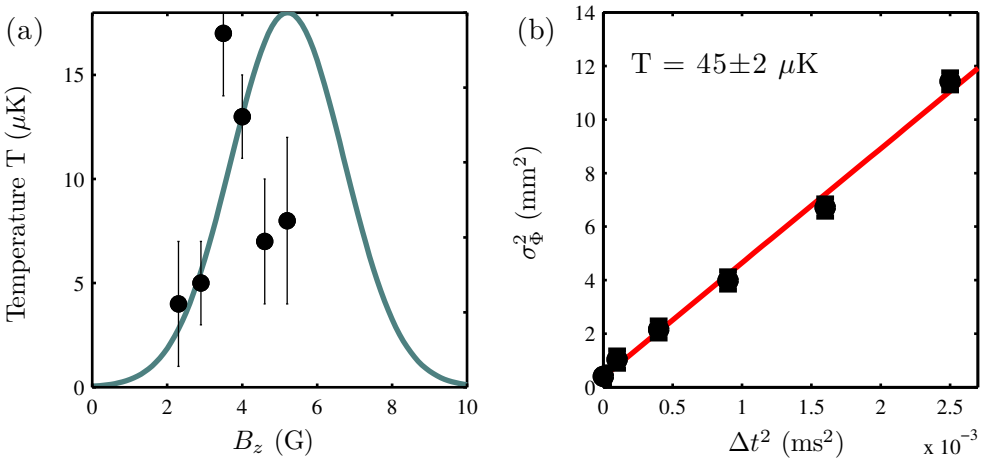

Figure 5.7: (a) Radial temperature of the atoms in the ring trap at $B_0 = 55$ G as a function of B_z. The (normalised) Gaussian atom number fit is overlayed for comparison. (b) Temperature fit for azimuthal atom distribution, using the ring trapping time as time of flight. The temperature is observed to be equal to the QP temperature.

be explained from the cut-off temperature for Majorana losses, which would be higher for higher B_z. A further increase in B_z leads to the trap not only becoming flatter but also shallower (the added bias field decreases the trap depth), so that the atoms with the highest energy can escape more easily, therefore bringing the atom temperature down again. Despite finding qualitative agreement with our understanding of the role the bias field plays for the velocity distribution of atoms, we can't put too much faith into the interpretation due to the ambiguous definition of temperature in this non-Maxwell-Boltzmann and non-re-thermalising case.

5.2.4.2 Azimuthal temperature

There is no azimuthal confinement in the ring trap, so that we can use the ring trapping time as t_{tof} and use the lifetime data for analysis. The resulting azimuthal temperature, T_Φ, is equal to the QP temperature within the uncertainties for short trapping times, see Figure 5.7, which is in agreement with the assumption that there is no further heating associated with the trap.

B_z(G)	T (μK)	f (Hz)
2.3	4 ± 3	9 ± 7
2.9	5 ± 2	8 ± 4
3.5	17 ± 3	13 ± 3
4.0	13 ± 2	15 ± 2
4.6	7 ± 3	7 ± 3
5.2	8 ± 4	8 ± 4

Table 5.1: Radial temperature and trap frequency for different ring traps, $B_0 = 55$ G, $t_{\text{hold}} = 150$ ms.

5.2.5 Trap frequency

Measuring the trap frequency gives us information about how tightly the atoms are confined in the trap by the potential, i.e. how steep the walls of the trap are. From the ring trap simulations, we expect a radial trap frequency of $\omega_r/2\pi = 16$ Hz for a thin ring trap. We obtain the radial trap frequency from the time-of-flight data used for temperature analysis, using Equation 4.8. The results from the time-of-flight method for $B_0 = 55$ G with different B_z are summarised in Table 5.1. From our understanding of the trapping potential, we expect a lower trap frequency with higher bias, as the bottom of the trap is flattened and the potential minimum is shifted to the less tight regions of the potential. We can't see this behaviour, because of the large uncertainties (especially for thin traps), mainly from the fit for the initial size being not very accurate and from the uncertainty in T. This is not surprising, since the trap and atom properties depart from the assumptions for this method (as explained in Section 4.4).

As a result, all we can conclude is that the trap frequency is of the order of 10 Hz. However, this matches our observations of radial oscillations of atoms in a thick ($B_0 = 83$ G, $B_z = 8.1$ G) ring: the peak position of the atom distribution as a function of time is recorded (shown in Figure 5.8), and radial oscillations with a period of ~ 100 ms are observed. If the cause for the radial oscillations is assumed to be the radial trap frequency, this would correspond to $\omega_r/2\pi = 10$ Hz. This complies with the idea of atoms being in a flat trap and sloshing radially.

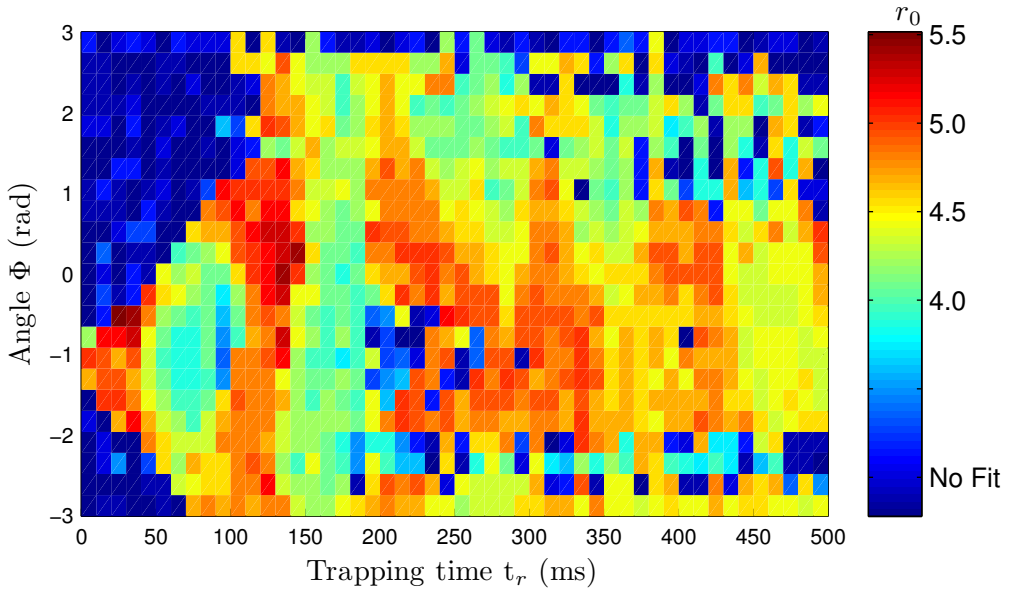

Figure 5.8: Trap frequency analysis: The peak of the radial atom distribution (red being large r_0) is plotted versus angle and time. Dark blue indicates no information. The ring trap is a thick ring with $B_0 = 83$ G, $B_z = 8.1$ G.

5.2.6 Evolution

The cloud of atoms spreads in the ring trap due to its thermal velocity and due to any momentum it gets during the loading process and from the potential when in the trap. Using the lifetime data, we can look at how the atoms evolve after being released into the ring trap and how they fill the ring with increasing trapping time. Two ring trap configurations are shown in Figure 5.9: firstly, the atoms in a thin ring ($B_0 = 55$ G, $B_z = 2.3$ G) are imaged for trapping times from $t_r = 0$ (loading) to $t_r = 150$ ms (a). We observe that the atoms spread evenly in the thin ring trap, and after 150 ms they fill the ring completely. Secondly, the atoms are shown in a "beamsplitter" configuration ($B_0 = 55$ G, $B_z = 4.6$ G) for trapping times from $t_r = 0$ (loading) to $t_r = 350$ ms (b). This configuration is an extension of the thick ring (large B_z), where the atoms are loaded at the edge of the trap and have enough energy to climb along the sides of the potential hill in the centre of the wine bottle potential. The atom cloud is thereby split into two counter-propagating wavepackets, which focus opposite the loading position

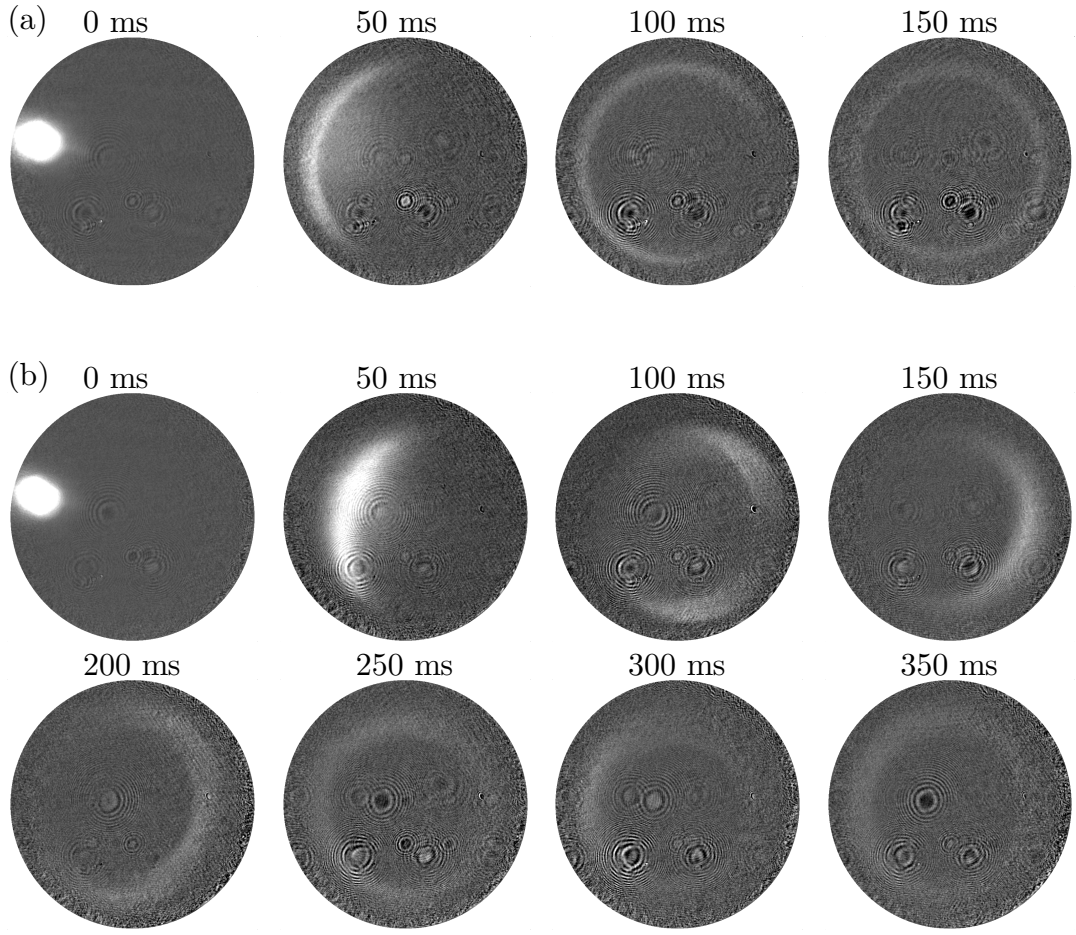

Figure 5.9: Atom evolution at two different trap geometries: (a) thin ring and (b) in a beamsplitter configuration. The trapping times are shown for each ring trap image. The thin ring trap is completely filled after 150 ms, the atoms in the beamsplitter focus opposite the loading position after 150 ms and refocus at the starting point at 300 ms.

after 150 ms and refocus at the starting point at 300 ms, afterwards the atoms fill the ring more evenly. These two ends of the spectrum of the ring trap geometry show how versatile it is. Apart from its application to confine the atoms, atom dynamics as well as trap properties can be explored. Videos of atom evolution in the thin ring trap and in the beamsplitter are available, please refer to the supplementary data in [1].

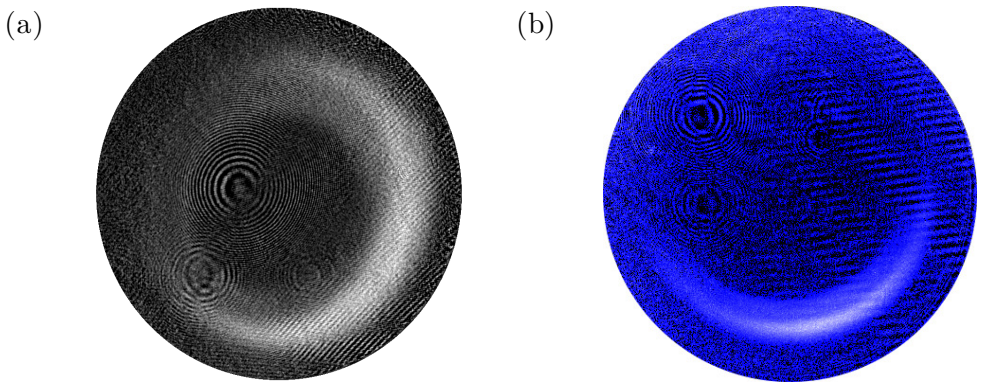

Figure 5.10: A double ring is visible for some ring traps employing high bias fields, here for (a) the axial bias and (b) the tangential bias.

5.2.7 Additional observations

There are two more interesting properties of the ring trap, which we would like to share: one regards the corrugation of the ring, the other regards the trapping of what is possibly a different m_F-state.

Ring corrugations The atoms in the trap are used as a probe to measure trap corrugation, to confirm that the use of AC instead of DC currents in the trapping field producing conductor leads to a smoother trap. Corrugations in the trapping potential should be visible as dips and hills in the atomic distribution, and the atom distribution as a function of time is analysed for signs of potential roughness. With the atom sample being at $T_{\mathrm{QP}} = 42$ μK, we are limited in the resolution of the corrugation size, which could be circumvented by using colder samples, such as a BEC. For the thin ring trap ($B_0 = 100$ G and $B_z \approx 6$ G, to have good signal strength), no corrugations above 1 μK are found.

Double ring For some traps, especially with strong magnetic bias field, a faint double ring is observed inside the regular ring trap. Two examples are shown in Figure 5.10, one for axial bias and one for tangential bias. We suspect that the

double rings are due to other m_F-states being trapped in the potential, which experience a different force and hence form at a slightly offset position.

5.3 Summary

We have examined the properties for the ring trap for different axial bias field strengths, as well as for a semi-circular trap created using a tangential bias field. Focussing on the axial bias trap, the ring trap geometry and the associated properties depend on the bias field strength. This allows us to tune the radius and the width of the trap within limits, creating either a thin ring trap, a thick ring trap, or even an atomic beamsplitter. We find the lifetime of the trap to have two components: the fast component ($\sim$ 200 ms) is due to Majorana losses, the slow component (1.3 s) is comparable to the QP lifetime and due to background collisions. We expect that the lifetime will only be vacuum limited for atoms as cold as in a BEC. A bit more difficult is the temperature measurement, because of the non-Boltzmann distribution of velocities, caused by the magnetic zeroes. This will also cease to be a problem if we cool the atoms to a BEC. With the thermal atoms in the ring, the effective temperature is a result of the QP temperature and the Majorana cut-off temperature, and it can be measured over a limited range. Azimuthally, the temperature does not change compared to the QP temperature, and it is $T_\phi = T_{QP} = 42 \pm 3$ μK. We can observe the atom evolution in the trap due to the long lifetime and see the atoms filling the trap. We also use this data for estimating how smooth the ring trap is, and we find no potential corrugations up to the resolution of our technique (limited to 1 μK). For the second generation experiment, improvements are made from what we learned during the first generation experiment.

Chapter 6

The second generation ring experiment

With the first experiment, we have aimed for a proof-of-principle of the ring trap, and the result was very satisfying: despite the fact that we had to deviate from the original proposal in [2] (by using an axial bias instead of a QP field), we were successful in creating and characterising a ring trap for cold atoms. Not only does it agree with our simulations for the ring trap which provides us with support when designing new trap, but we now also have the potential to vary between a narrow ring trap and an atomic beamsplitter. It is now time to base on what we have learned from the first experiment and create the improved, second generation ring experiment. The goal of this is to design the ring trap experiment for atom interferometry with degenerate quantum gases.

6.1 Towards Bose-Einstein condensation and atom interferometry in the ring

For the second generation ring trap experiment, the "BEC ring", we have to consider two new aspects: the requirements for the creation of a rubidium Bose-Einstein condensate (BEC) and the demands on the ring trap and the optics layout arising from wanting to perform atom interferometry in the ring. The additional tools and techniques necessary, namely an improved version of magnetic

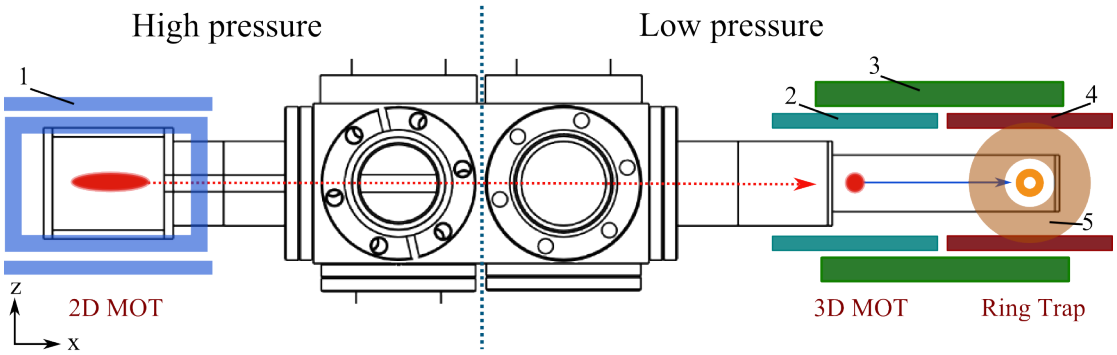

Figure 6.1: Schematic sideview of the main experimental setup: shown is the body of the vacuum chamber, divided into the high pressure side and the low pressure side, which are connected by a differential pumping tube. Atoms are pre-cooled in a 2D MOT on the high pressure side and transferred to the other side, where a 3D MOT is formed. Because the ring is separated from the MOT by a distance of ca. 6 cm, the atoms are transferred magnetically in a QP, for which three sets of coils are used to shift the magnetic minimum. Labelling: 1 - QP coils for 2D MOT (blue), 2 - 3D MOT coils (turquoise), 3 - Transport coils (green), 4 - QP coils (red), 5 - AC drive coils (beige). The coil sizes are not to scale.

transport for the ring loading, *evaporative cooling* for BEC and *Kapitza-Dirac scattering* to split the atomic wavepacket for interferometry, are accounted for in the experiment. We present the main new features of the experimental setup, followed by a more detailed description of the new techniques. The heart of the experiment is schematically shown in Figure 6.1, a full description of the setup and the step-by-step sequence will follow at a later stage.

A completely new vacuum system was built for the second generation experiment. With the old chamber, we would not have been able to create a BEC due to the high background pressure. To provide the vacuum required for BEC, we build a two-chamber vacuum system: a "high" pressure chamber where a large number of atoms is released from the atomic source and pre-cooled to provide an atomic reservoir in the form of a *2D MOT* [121] and a second chamber that is pumped to a higher vacuum and loaded from the reservoir. The two chambers are connected by the *differential pumping tube*, which provides a small opening for atom transfer while keeping the pressure at different levels. The low pressure in the second chamber allows us to make the transition from cold rubidium atoms

of tens of μK in a trap, to a degenerate quantum gas at hundreds of nK. The particular need for the low pressure arises from evaporative cooling (the final cooling stage) which lasts seconds to tens of seconds for the intended method [97]. We achieve the required trap lifetime by reducing the background pressure to minimise background collisions. Although BEC has been created in a single chamber setup [122], the obvious choice for us when designing the new setup was the two-chamber system. Once the atoms are transferred from the high pressure to the low pressure side, they are captured in a 3D MOT. As in the first experiment, we are not able to create the MOT in the plane of the ring because the optical access is blocked by the copper ring itself. The MOT position was previously underneath the ring, from where the atoms are transferred in a QP trap into the plane of the ring. In the new experiment, we apply a slightly different solution: the atoms are still moved in a QP with magnetic transport, but instead of shifting them upwards, they are moved sideways to a position fairly far away from the 3D MOT ($\sim$ 6 cm), using the method realised in [123] (magnetic field calculations follow below). This allows us to create a 3D MOT very close to the opening of the differential pumping tube where the atoms enter the low pressure chamber, it also means that we have better optical access for the cooling beams than at the ring position. The magnetic fields for the magnetic transport are produced by three overlapping sets of QP coils, which are designed to create a magnetic minimum first at the MOT position and smoothly shift it towards the ring position.

Considering atom interferometry, we prepare the setup appropriately, so that the experiment can be taken to the next level in the future. We therefore recall that the atomic wavepacket has to be split coherently to propagate along the two arms of the ring and recombined in the end to produce an interference pattern caused by the phase difference accumulated along the paths. What we need to include in the the setup to prepare for atom interferometry are therefore atomic beamsplitters, for which we use light pulses. The technique we want to use for splitting the cloud is Kapitza-Dirac scattering, as demonstrated in [17]. To enable optical access for the splitting pulse and to focus it on the atoms in the ring, the inner edge of the copper ring is tapered. The copper ring itself is also reduced in size, creating a smaller ring trap, and we change the orientation to be vertical.

For atom interferometry, the smaller size of the new ring trap is preferable: the visibility of interference fringes is governed by the fixed spatial coherence of the split atomic wavepacket, which disappears over the duration of the coherence time. From an experiment with condition similar to our own [124] (^{87}Rb BEC in a symmetric wave guide with low trap frequency), a coherence time of 72 ms is inferred from fringe visibility.

Before looking at the experimental sequence, we describe the theory behind the three new tools in more detail, starting with magnetic transport, followed by evaporation to create a BEC and Kapitza-Dirac splitting for future atom interferometry experiments in the ring trap.

6.1.1 Magnetic transport

We start by loading atoms from a 2D MOT into the 3D MOT, which is positioned near the exit of the differential pumping tube. To transfer the cloud of cold atoms from the 3D MOT position over ~ 6 cm to the ring loading position, we transport them magnetically in a QP trap, as explained in [123]. Additionally, we apply a bias field along y towards the end of the transport sequence, to shift the atoms *around* the ring. The magnetic transport along x works by adjusting the current through several, overlapping coils such that the magnetic minimum is shifted smoothly from the initial to the final position: the QP at the centre of the first coil is shifted to the centre of the second coil by increasing the current in the second coil, at the same time the current in the first coil is decreased. This is repeated for subsequent coils, until the magnetic minimum moves the atoms to their final position. Along the direction of transport, x, we want the magnetic field gradient to be constant and the transfer to be smooth, to avoid heating of cloud. It is shown experimentally [123] that heating can be kept small ($\Delta T \sim 20$ μK for a cloud at $T = 125$ μK). We use three coils for the transport, which are all centred onto $y = 0$ and $z = 0$, but displaced along x. For better control over the shape of the magnetic field during the transport, the coils are overlapped to the extend that the second coil covers nearly all of the first and the last coil (see Figure 6.1). Because the separation of the top coil pair is increased by the thickness of the lower coils, the coils are wound flat but wide. This reduces the requirement for

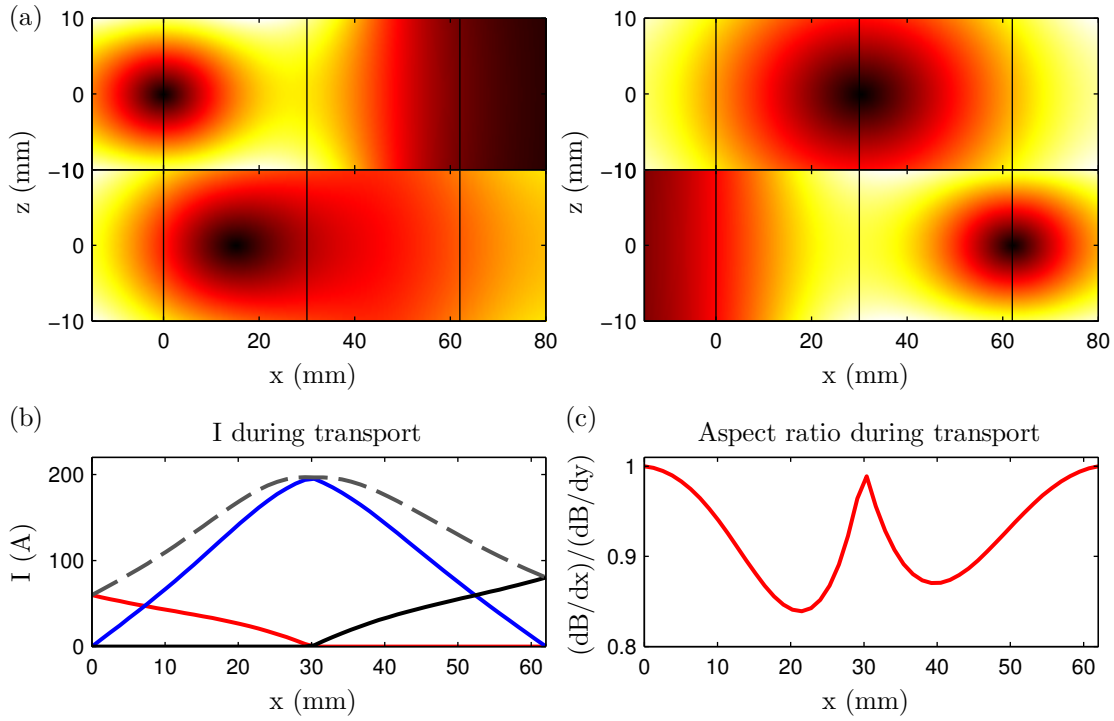

Figure 6.2: The magnetic transport: (a) magnetic minimum at different positions during the transport sequence (top to bottom and left to right): first coil centre (initial position), between first coil centre and second coil centre, at second coil centre and at the third coil centre (final position). The centre of each of the three coils in indicated with a black vertical line. (b) The calculated current distribution in the three coils to achieve the transport (coil 1 - red, coil 2 - blue, coil3 - black) and the total current (dashed line). (c) The aspect ratio can not be held constant throughout the transport, but it stays fairly close to 1.

additional current in the top coils. We now numerically solve for those currents in the coils that shift the magnetic minimum from the starting position to the finishing position. To get a suitable solution for magnetic transport, we add the constraints from [125]:

$$I_1 B_1(x,0,0) + I_2 B_2(x,0,0) + I_3 B_3(x,0,0) = 0 \ , \tag{6.1}$$

which makes sure that the total magnetic field at the minimum is $B = 0$, with B_1, B_2, B_3 being the magnetic field in Gauss per Amp for each coil and I_1, I_2, I_3

being the current. To keep the gradient constant, we use [125]:

$$I_1 \frac{\mathrm{d}B_1(x,0,0)}{\mathrm{d}x} + I_2 \frac{\mathrm{d}B_2(x,0,0)}{\mathrm{d}x} + I_3 \frac{\mathrm{d}B_3(x,0,0)}{\mathrm{d}x} = \text{gradient} \ . \tag{6.2}$$

Because of the shape of the coil, the radius differs for each turn so that the field is calculated for each turn individually and then added. The resulting magnetic field for different points in the transport sequence is shown in Figure 6.2 (a): at first the magnetic minimum (dark) is located at the centre of coil 1, then it moves along, until it reaches the centre of coil 2 to reach its final position at the centre of coil 3. At its final position, there is only current in coil 3. The corresponding coil currents are shown in (b), where the shift from one coil to the next (coil 1 - red, coil 2 - blue, coil 3 - black) is visible. The total current is indicated (grey dashes). Finally, (c) shows the calculated aspect ratio:

$$\frac{\mathrm{d}B/\mathrm{d}x}{\mathrm{d}B/\mathrm{d}y} \ . \tag{6.3}$$

We have not put any constraint on the aspect ratio, it nevertheless only varies between 1 and ~ 0.85.

At this point, the duration of the transport has to be optimised, by adjusting how fast the current distribution between the coils change and the atoms are shifted in the magnetic minimum. To make the transport smooth, the cloud's velocity, v, and acceleration, a, are gradually increased following a squared sine curve to their respective maximum values, $v_{\max}$ and $a_{\max}$, until they ramp back to zero. The limits are optimised for minimum heating and for the shortest duration, as long transport times lead to atom loss due to background scattering. With values of $v_{\max} = 20$ cm/s and $a_{\max} = 4$ m/s^2, the transport duration is less than 400 ms. Figure 6.3 shows the position, velocity and acceleration during the magnetic transport as a function of time. Before the atoms reach the loading position, we have to manoeuvre them around the copper ring, which is done with a bias field along y. The field strength is calculated from the QP field gradient and the displacement of the cloud around the ring, the duration is adjusted using the same maximum values and ramps for v and a as for the magnetic transport along x.

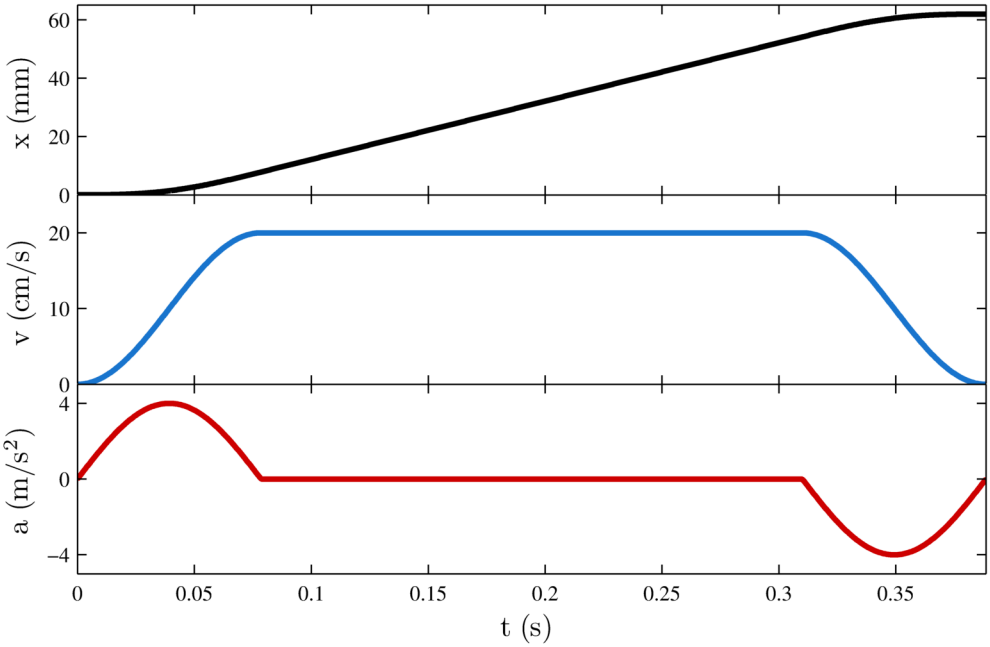

Figure 6.3: Position, velocity and acceleration during magnetic transport.

6.1.2 Evaporative cooling

In atomic physics, evaporative cooling is the final cooling stage to produce a BEC, because the cooling process is not quantised by the photon energy, which fundamentally limits the coldest temperature achievable with radiative cooling methods. A good introduction to the theory of evaporative cooling can be found in [126]. When an atom cloud with a Boltzmann-distribution of velocity is in a trapping potential, we can remove the highest energy atoms by lowering the potential at the edges. Because low energy atoms in the potential will be unaffected and only atoms with enough energy to climb the potential hill can escape, the high energy tail of the Boltzmann-distribution disappears. The atoms then re-thermalise and the Boltzmann-distribution shifts towards lower energies and narrows – cooling is achieved. This step is repeated by lowering the potential further and further, until the transition temperature for BEC is reached, while optimising for atom number (which is decreased) and phase pace density (which increases due to the cooling) at the end of the process, giving the efficiency [126]:

$$\gamma_{\mathrm{tot}} = \frac{\ln(PSD'/PSD)}{\ln(N'/N)} \ , \tag{6.4}$$

with PSD and N being the initial and PSD' and N' being the final phase space densities and atom numbers, respectively.

For evaporation to be successful and the re-thermalisation process to take place, it is important to have a large enough ratio of scattering rate for elastic collisions, $1/\tau_{\mathrm{el}}$, to the rate of inelastic collisions with the background gas, $1/\tau_{\mathrm{inel}}$. Otherwise all atoms will be lost from the trap due to background collisions [126]. When the "good" (elastic) collisions outweigh the "bad" (inelastic) collisions by a large enough factor, the elastic collision rate starts to increase with time, leading to *runaway evaporation*. Here, we use a *hybrid technique* similar to [97], where we transfer the atoms from a QP trap into a dipole trap, to make use the respective advantages: while evaporation in a QP trap leaves us with more atoms than evaporation in a dipole trap, Majorana losses affect the atoms once they are cold enough for a large fraction to spend significant amounts of time at the centre of the trap (we see increasing atom loss during evaporation in the QP from $T < 50$ μK). At that point, the atoms are transferred into the dipole trap, with a reduced QP field still on to increase the scattering rate, and the evaporation to degeneracy is continued.

RF evaporation in the QP trap In a magnetic QP trap, atoms with low kinetic energy are primarily located towards the bottom of the trap, while atoms with high energy "climb up" the potential in regions with higher magnetic fields. High energy atoms therefore experience a different energy shift of their magnetic sub-levels (m_F-levels) than atoms with low kinetic energy. This difference in energy shift is exploited by the technique of *RF evaporation* [62]: an added radio-frequency (RF) signal with frequency ω_{RF} couples a trapping and an untrapping m_F-level of an atom, if the energy difference between the levels is $\omega_{\mathrm{RF}}\hbar = g_F\mu_B B\Delta m_F$. This induces a spin-flip and the atoms are lost from the trap. The frequency of this "RF-knife" is then lowered, and another fraction of high energy atoms is selectively removed from the re-thermalised sample, until the desired temperature is achieved. After that, the dipole trapping lasers are

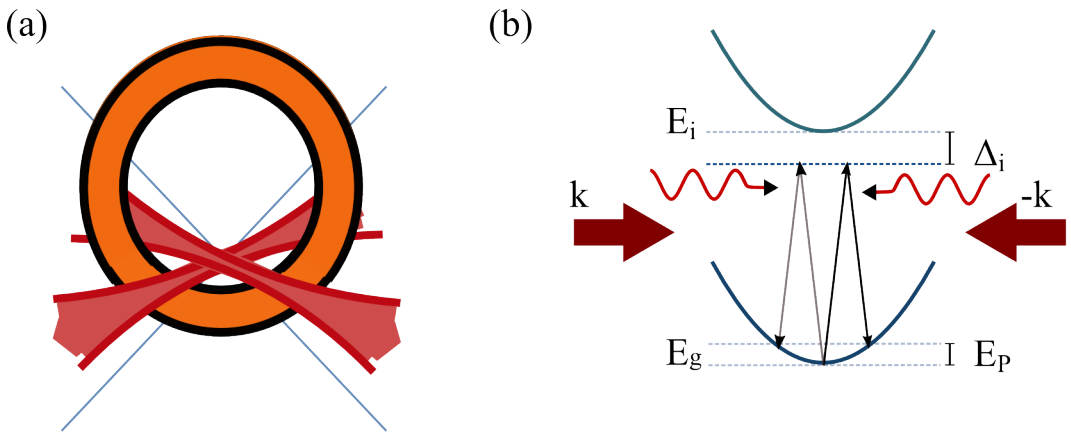

Figure 6.4: (a) Schematic of the hybrid evaporative cooling inside the copper ring: a QP field and a crossed dipole trap are employed to cool the atoms. (b) A standing light field of two counter-propagating lasers (k,-k) transfers momentum to the atoms in E_g in a two-photon process via the intermediate level E_i (the light is detuned by Δ). The two photons indicated put an atom into the $+2\hbar k$ momentum state (black), but equal distribution into the $-2\hbar k$ occurs (grey).

switched on, the QP field is relaxed and the atoms are released into the dipole trap.

Evaporation in the dipole trap Due to the attractive potential associated with the red detuning of light compared to an atom's transition, we can use high intensity light to trap atoms in dipole traps (see e.g. [37, 127]). Here, the potential arises from the interaction of the electric field of the light and the induced dipole moment of the atom. The trap depth scales with the intensity divided by the detuning, I/Δ, and to reduce the potential and release atoms at the high energy end of the distribution we decrease the light intensity. In this setup, we use a crossed-dipole trap [128], to confine the atoms axially by overlapping two beams at their focus, with a low gradient QP field for additional confinement and to aid the evaporation process. Figure 6.4 (a) shows a schematic of the hybrid trap inside the copper ring. The trapping light has a large detuning, to reduce heating from photon scattering, as the scattering rate scales with I/Δ^2. The intensity of the two beams is ramped down exponentially, and with this technique, we reach the critical temperature and make the transition to BEC.

6.1.3 Atom cloud splitting with Kapitza-Dirac pulses

With the cold atoms loaded at the ring, we have an atomic wavepacket with initial momentum of $p_0 = 0$ at the initial position x_0. To split the atomic wavepacket, we use light in form of standing waves to act like a grating and diffract the atoms into different momentum states (as first proposed in [129], for more information see e.g. [50, 53]). A schematic of photon momentum transfer from $p_0 = 0$ to $p = p_0 \pm 2\hbar k\rangle$ via an intermediate level is shown in Figure 6.4. Here, we plan to use Kapitza-Dirac pulses: a short pulse of two counter-propagating beams transfers atoms via a two-photon absorption process into several momentum states $|p_0 \pm 2n\hbar k\rangle$, where k is the photon momentum and n is the order. Ideally, we want all atoms in $n = 1$, so that the cloud splits into two halves with opposing momentum. To have as much control as possible over the population of the different orders, we consider the two-pulse scheme as applied in [17] and explained in [130], with which almost 100% of atoms where transferred into $|p_0 \pm 2k\hbar\rangle$. For this method, the pulse duration, delay and amplitude are of importance. With the atoms now in a superposition of opposing momentum states, they propagate around the ring. Once the atoms have completed their orbits and are back at the initial position, the pulse sequence is repeated to recombine the wavepackets and to let them interfere. Depending on the phase shift between the wavepackets – which is acummulated along the two arms of the ring – relative to the phase of the beamsplitter, the atoms will end up in either a $|p_0 \pm 2k\hbar\rangle$ state or in $|p_0\rangle$ (if there is no phase shift, then the splitting pulse is just inverted, and all atoms should come to a halt). Finally, the atoms are released from the trap, they spatially separate – due to their different momenta – and can be imaged to measure the population distribution and retreive the phase shift .

With the ring geometry, we can choose between different scenarios for propagation, which are depicted in Figure 6.5:

1. The atoms are loaded at the top of the ring and propagate around, with additional acceleration from gravity, to be recombined at their initial position

2. The atoms are loaded at the bottom of the ring and only propagate by $\sim \pi/2$, before gravitation pulls them back to their initial position.

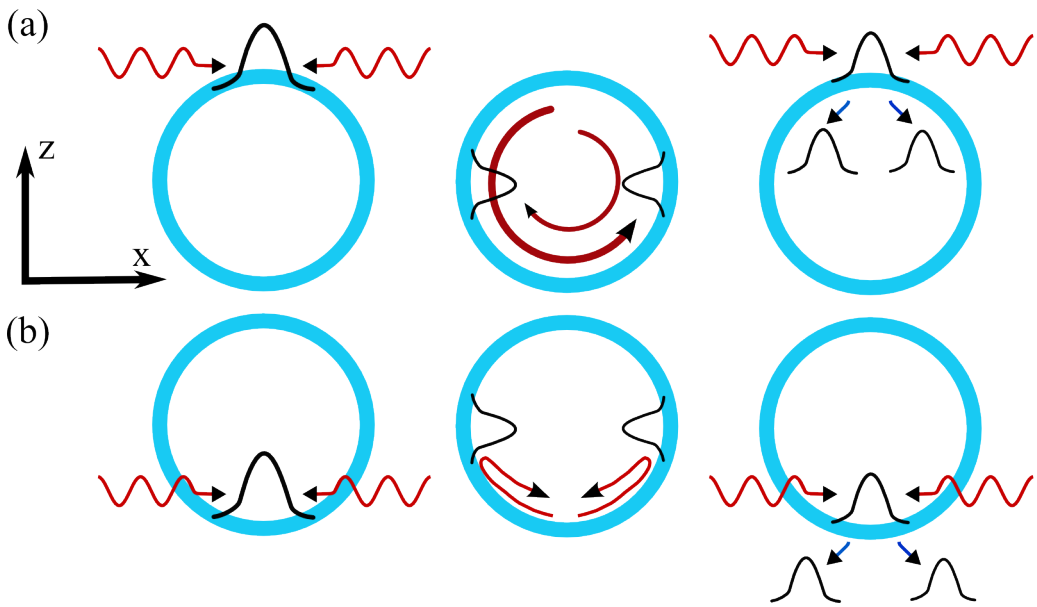

Figure 6.5: Two scenarios for interferometry: (a) the atoms are loaded at the top and split, propagate fully around the ring and are recombined at the initial position to produce interference. (b) the atoms are loaded at the bottom and split, propagate partially up the gravitational hill and return back to their initial position where they are recombined for interference.

The second scenario is a good place to start to test the interferometer, and it is possible to change the loading position later.

6.2 Experimental setup for ring trap 2

After introducing the main concepts and additional techniques for the BEC ring, we now discuss the individual elements of the setup and the experimental sequence. We start by describing the double-chamber vacuum system with the high pressure side for the 2D MOT and the low pressure side for the 3D MOT and the ring trap, continue with the magnetic coil properties and finish by going through the important steps of the experimental sequence, where relevant information about setup and experimental parameters is given. For the schematic of the main part of the experiment, please refer to Figure 6.1.

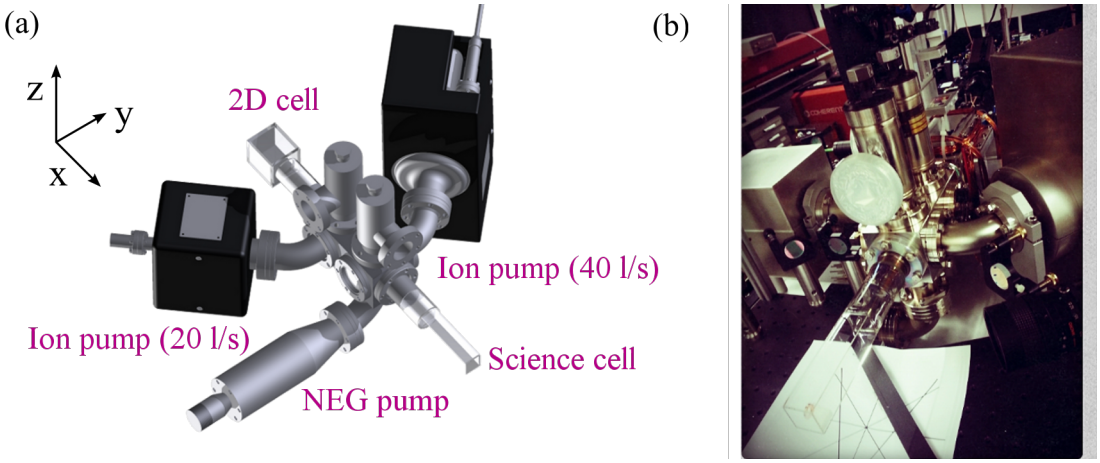

Figure 6.6: The vacuum chamber design (a) and the real chamber (b) with the science cell in the foreground. Later, the science cell is surrounded by different sets of coils.

6.2.1 Double-chamber vacuum system

The vacuum system for the second generation ring experiment consists of two cells at different pressures, connected via a differential pumping tube (narrow hole) to allow atoms to be transferred from one side to the other. This way, we can use high rubidium pressures to fill up an atomic reservoir – a 2D MOT where atoms are cooled in two directions and aligned onto the differential pumping tube along the third axis – in order to create a high atom flux for the 3D MOT, while maintaining low pressures for optimum conditions at the ring trap. The ion pumps and the glass cells are attached to a stainless steel body. A schematic as well as an image of the chamber are shown in Figure 6.6. For future reference, the direction along the long horizontal axis of the science cell is labelled x, the direction along the short horizontal axis of the science cell is labelled y and the up–down direction is labelled z. We now look at the important aspects of the vacuum system.

2D chamber The high pressure part is the 2D chamber, with a homebuilt glass cell housing the 2D MOT and the atomic sources. It is pumped by a 20 ℓ/s StarCell pump down to a pressure of initially 10^{-10} Torr as measured from

the ion pump current. With increasing rubidium usage, the pressure reading increases up to $\lesssim 10^{-8}$ Torr after several months.

3D chamber The low pressure part is the 3D chamber, with the science cell for the 3D MOT and the ring trap, the high pressure enabling long lifetimes of atoms in the trap by reducing background collisions. It is pumped by a 40 ℓ/s StarCell pump, down to below 10^{-10} Torr (the pressure is below the sensitivity of the pump reading, which stops at 10^{-10} Torr). A non-evaporable getter (NEG) pump is also connected to the 3D chamber to aid in maintaining the vacuum.

Differential pumping tube The differential pressure between the cells is maintained using a differential pumping tube – a hollow tube with a 2 mm opening on the 2D side and a length of 13.5 cm. Over this length, the pre-cooled atoms in the tube will diverge due to their transverse velocity (we expect ~ 40 mrad divergence for $v_t \approx 10$ m/s, compare [121]) and will also drop under gravity. To keep the atoms from hitting the walls, the diameter of the tube is stepwise increased: $d_{\text{diff}} = 2,\ 5.6,\ 7.2$ mm for a distance of 4, 6, 3.5 cm, as shown in Figure 6.7. With this geometry, the tube has a total conductance of ~ 0.022 ℓ/s, which should maintain a ratio of 10^{-4} between the pressure on the 3D side and the 2D side.

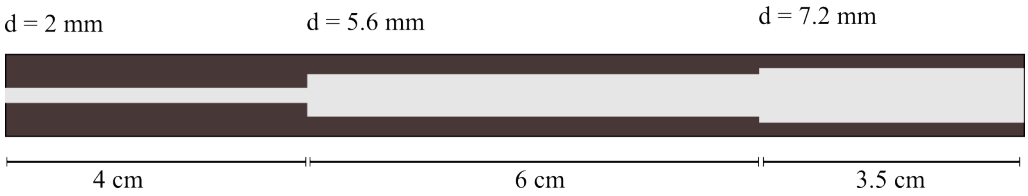

Figure 6.7: Differential pumping tube with varying hole diameter.

Baking The chamber was assembled and baked, but had to be re-opened due to problems with the dispensers. After opening and re-closing the chamber, the temperature of the chamber was slowly ramped up to around 200 °C using heating tapes, and the chamber was baked for two days.

Magnetic shielding Once the chamber is baked, the ion pumps are magnetically shielded with μ-metal, which attenuates the stray magnetic fields from the ion pumps in the cell region by a factor of 10.

6.2.2 Glass cells

For optical access during cooling and imaging of the atoms, we have two glass cells in our setup: the 2D cell, in which the 2D MOT is formed, and the science cell for the 3D MOT and the ring trap. The 2D cell is homemade, which is documented in the following Section, and the science cell is bought, but custom made due to its elongated geometry.

Homemade 2D cell The individual glass parts for making the 2D cell are anti-reflection (AR) coated glass plates from SLS Optics. Unlike with blown glass cells, here we can have AR coating on both sides of the cell. Because the glass plates are glued, a lip as wide as the glass plates' thickness is left uncoated on one side (this will be the inside of the cell). The glass plates must be glued at the same time to make sure that edges meet and the cell walls are straight. To hold the glass plates in place during assembling and curing, a jig is used as shown in Figure 6.8. Starting with the front plate of the glass cell placed at the bottom of the jug, we glue on the side plates using an epoxy (EPO-TEK 353ND). Because the glue is very fluid, we use a syringe for better control and to prevent air bubbles in the glue, which can lead to weak joints in the cell. Figure 6.8 shows the assembling process. Once the cell is glued, it is baked to cure at 130 °C and glued onto a glass-to-metal joint using a second jig. Finally, the completed cell is connected to the vacuum, see Figure 6.8 (c). The completed 2D cell has an outside diameter of 5 cm in x, y and z, with a wall thickness of 4 mm.

Science cell Due to its elongated shape, the science cell is custom made by Precision Glass Blowing. It is 10.2 cm long (4 inches) and has a square cross-section of 27.5 mm (1 inch), with a glass thickness of 1.25 mm, and it houses the copper ring. The outside is AR coated, and the cell comes with a glass-to-metal joint to connect to the vacuum chamber. Before transferring the copper ring

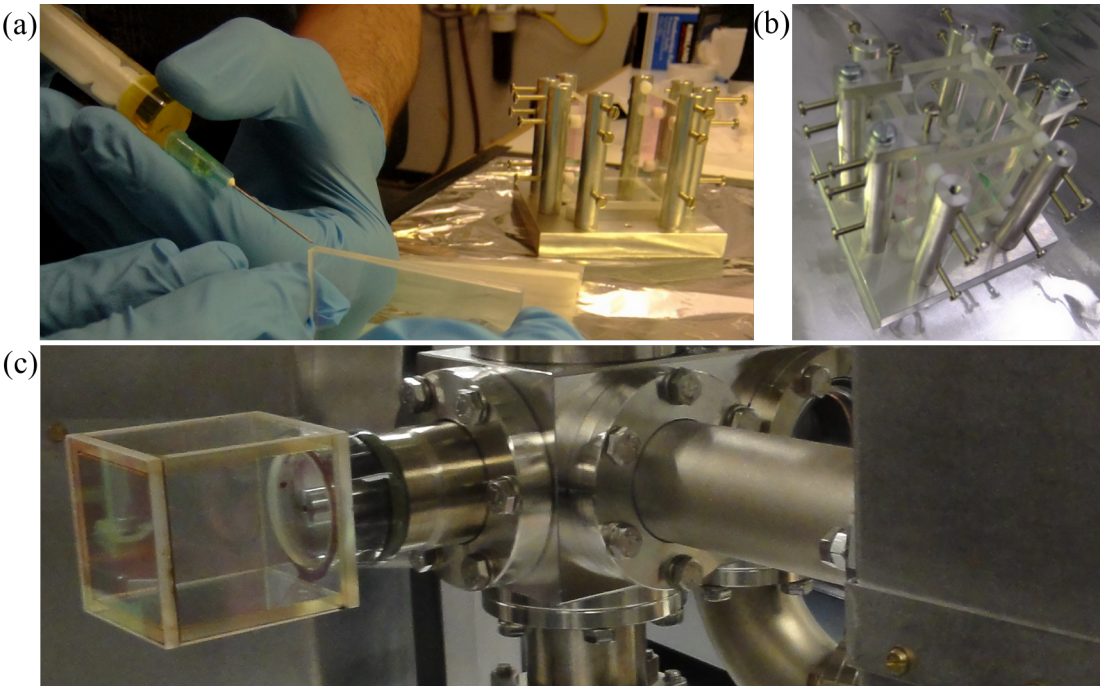

Figure 6.8: Building the glass cell for the 2D MOT: the sides of the cell are glued together with epoxy (a) and then cured at 130°C in a homemade supporting metal cage with nylon screws, before the cell is glued to the glass-to-metal joint and then baked. (c) The vacuum chamber with the completed cell.

to its position inside the cell, it is placed in its mount (shown in Figure 6.9) by pushing it into a slot where it is held tightly. The mount itself is made from Macor, which is slightly heat conductive, machinable and can be used in vacuum without outgassing. Using a Teflon shovel attached to a long handle, the mount and the ring are carefully transferred into the glass chamber as shown in Figure 6.9.

6.2.3 Atom source

To enable a wide range of possibilities for future experiments, the second generation experiment is equipped not only with a source of Rb to make BEC, but also with isotopically enhanced potassium to make DFG, especially for the application of atom interferometry with fermions. Unfortunately, we experienced difficulties when first implementing the atom source, meaning we had to break vacuum and replace the dispensers. The first assembly included 4 dispensers from

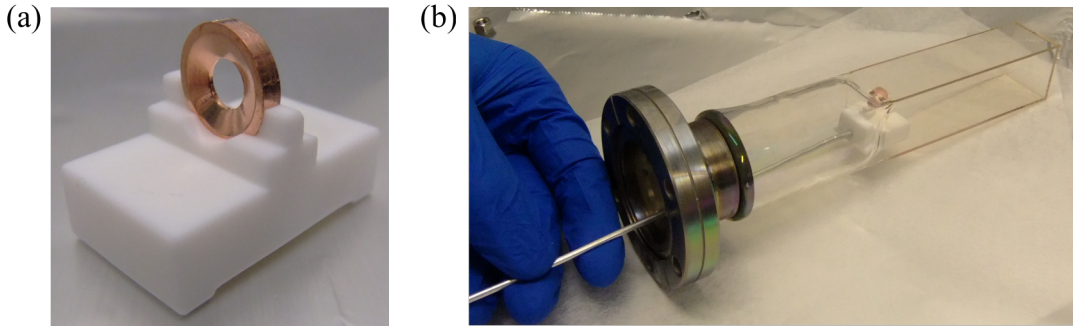

Figure 6.9: The copper ring on the Macor mount (a), which is transferred into the science cell by carefully carrying it inside with a plastic shovel on a handle (b).

Alvatec (2 Rb, 2 K), on shortened copper rods as feedthroughs (2.5 cm distance from the top of the ceramic insulation to the dispensers). To reduce the overall size of the vacuum part, the stainless steel tags at the dispensers were shortened before attaching them to the feedthrough with copper connectors. This caused the feedthroughs to act as a heatsink for the crucible with the atomic source. This prevented the active material to reach the necessary temperature for atom release, while the metal got glowing hot at other, undesired places (e.g. the metal bends of the dispensers). To be able to see any absorption, much more current was required than recommended by the manufacturer (7 A instead of the recommended 3 A). To avoid complications further into the experiment, e.g. cracking of the insulating ceramic around the metal rods due to heat, the feedthrough and the dispensers were changed. The vacuum design was extended to allow for longer legs of the atomic source and the feedthrough metal rods. Additionally, the metal rod material was exchanged for nickel, which is less heat conductive than copper and should prevent cooling of the dispensers, without sacrificing much electrical conductivity. Images of the two versions of feedthroughs with the dispensers are shown in Figure 6.10: (a) shows the old feedthrough with the dispensers on shortened legs, and (b) shows the improved feedthrough, where the metal rods and legs have only been shortened as much as necessary.

The new feedthrough also comes with eight instead of four metal rods (LewVac FHP5-15N8-40CF), so that the dispenser arrangement is changed and a total of five dispensers are connected: two ^{40}K dispensers (Alvatec, isotopically enhanced

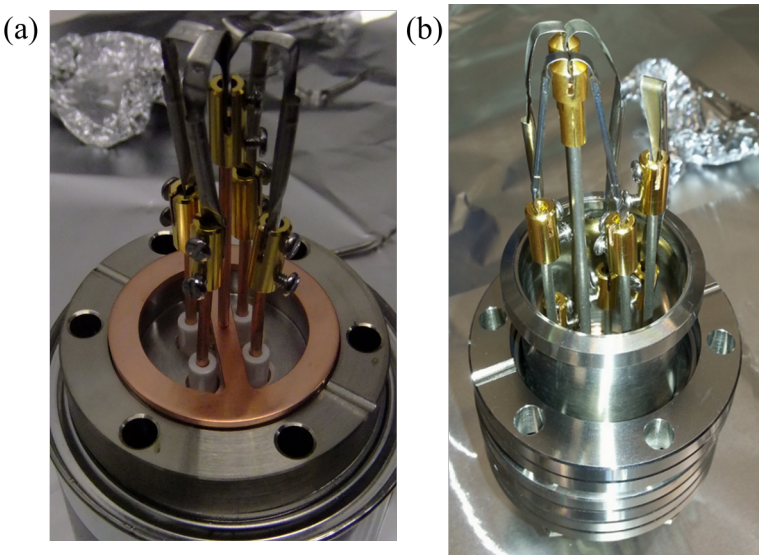

Figure 6.10: First feedthrough (a): Rb and K dispensers with shortened legs and shortened copper rods. This setup led to extensive heating at the bends of the dispenser metal and should be avoided! Second feedthrough (b): Rb and K dispensers on long nickel rods. The rods were only shortened as much as necessary to connect the dispensers. This setup dispenses atoms at the recommended currents without extensive heating at the bends.

^{40}K, increasing its abundance from $\sim$ 0.01% (natural) to $\sim$ 5%) with common ground pin, two ^{87}Rb dispensers (SAES) with common ground pin and one independent ^{87}Rb dispensers (Alvatec). The dispenser arrangement can also be seen in Figure 6.10 (b). After activation, the dispensers are run at 2.8 A during the experiment.

6.2.4 Copper ring

The copper ring in the second generation ring experiment has three major differences to ring 1:

1. It is smaller
2. It is mounted vertically
3. It is not of rectangular cross-section, instead it has a tapered inside edge

The ring has an outer radius of 5 mm, an inner radius of 2 mm and a thickness of 2 mm. Of the 3 mm width, 1 mm is flat and 2 mm are tapered. A schematic of the ring cross-section in shown in Figure 6.11.

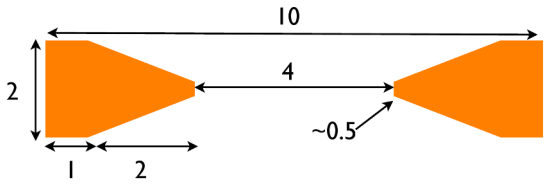

Figure 6.11: New ring (ring 2) cross section and dimensions (in mm).

Having a tapered edge means that we can reduce the ring size, while maintaining optical access for the dipole and Kapitza-Dirac beams, which cross in the plane of the ring and come in at an angle. The reduced size and the vertical orientation, on the other hand, mainly stem from considerations for atom interferometry, where the coherence time becomes an important factor: we want the orbital period of the ring trap to be within the coherence time of the BEC. A smaller ring is therefore advantageous, provided we stay in the regime for which the Larmor frequency is larger than the drive frequency, which is important for the adiabaticity of the ring trap. Including gravity, which accelerates the atoms around the ring when it is mounted vertically, we estimate an orbital period of 130 ms.

The ring is calculated to have a DC inductance of $L_{\mathrm{DC}} = 6.4$ nH, with a DC resistance of $R_{\mathrm{DC}} = 81\ \mu\Omega$. An additional impact of the reduced size of the copper ring is that the drive frequency has to be increased in order to get the desired current in the ring, and we use a drive frequency of $f_{\mathrm{AC}} = 50$ kHz. At this frequency, the inductance is calculated to be $L_{\mathrm{AC}} = 5.0$ nH, the resistance increases to $R = 236\ \mu\Omega$.

6.2.5 Magnetic coils

We need several sets of coils to produce the necessary magnetic fields for 2D MOT, 3D MOT, magnetic transport and ring trap. On the 2D side, we need a cylindrical symmetric quadrupole field for the 2D MOT, for which we use one set of

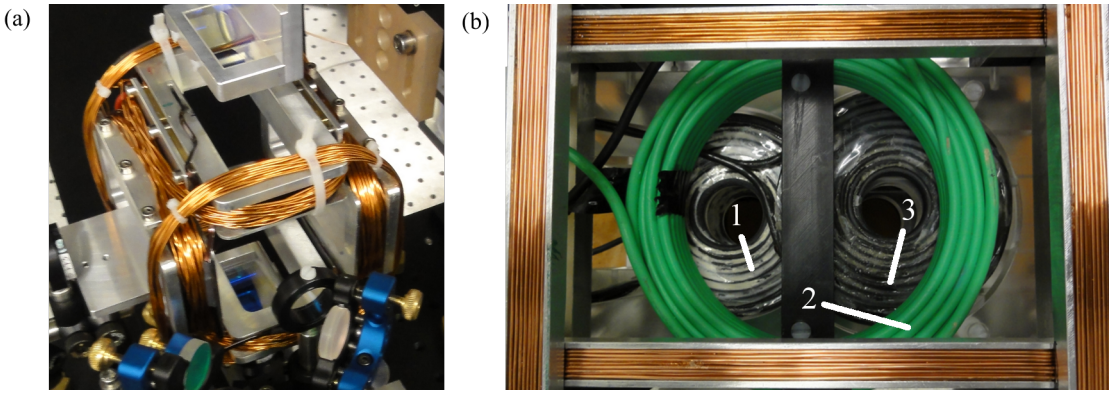

Figure 6.12: The coils of the second generation experiment: (a) rectangular QP coils plus shim coils for the 2D MOT. (b) The coils for the magnetic transport on the 3D side, seen from above: the MOT coil (1), the transport coil (2) and the QP coil (3), which is the final position for the QP and is centred on the copper ring.

rectangular QP coils aligned along the z axis, and a second identical set is aligned along the y axis. The coils are made from flat, Kapton coated wire, each coil is 11.4 cm long and 5.5 cm wide and each coil pair has a separation of 9 cm. The gradient is the same in both axes, with $\frac{\mathrm{d}B}{\mathrm{d}y} = \frac{\mathrm{d}B}{\mathrm{d}z} \approx 2.4$ G/cm/A. Additional shim coils provide bias fields ($\sim$ 2 G/A) in all three axes, they are wrapped tightly around the 2D coil holder. The coils are shown in Figure 6.12 (a).

On the 3D side, a more sophisticated housing is needed to hold all seven sets of coils in place. Having one holder for all coils has the advantage that the coils are held in place tightly to keep the magnetic fields constant, and it allows for careful alignment of the coils with respect to each other. It also confines the coils to a restricted space while keeping optical access clear where necessary. Of the three coils for the magnetic transport (compare Figure 6.1), the first set of coils, the *MOT coils*, are also used to produce the magnetic field for the 3D MOT. The coils are wound from hollow copper pipe. Designed to be as flat as possible, they have only two layers, giving a thickness of < 1 cm. We measure a gradient of 1.57 G/cm/A for the MOT coils. The second pair of coils for transport, the *transport coils*, are on top of the other coils and therefore don't need to be as flat. Hollow copper pipe is also used for these coils, and we achieve gradients of 0.53 G/cm/A. The final coil pair for the magnetic transport,

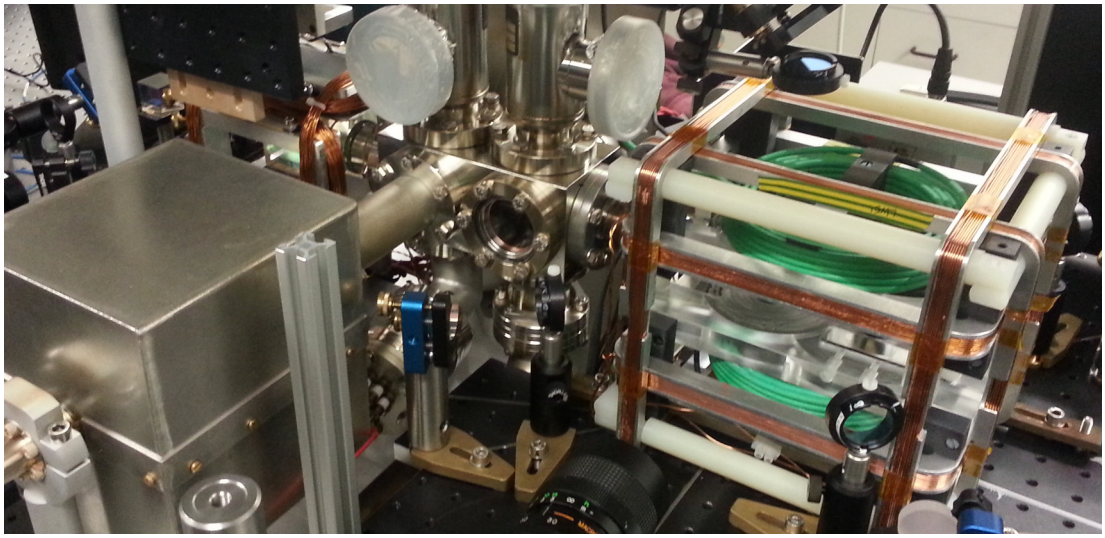

Figure 6.13: The 3D side of the chamber with all magnetic coils surrounding the science cell.

the *QP coils*, are similar to the MOT coils in design. They provide us with a gradient of 1.21 G/cm/A, and they provide the final QP field of the magnetic transport, including the QP field during evaporation at the ring loading position. Figure 6.12 (b) shows the magnetic transport coils from above. Parallel to the ring, the AC drive coils are placed in Helmholtz configuration. Unlike in the first experiment, the QP coils and the AC drive coils are orthogonal, so that induced voltage from the AC field in the QP coils will be less of a problem and a QP field can be applied to offset the magnetic zeroes for the ring trap. The AC drive coils are centred on the ring and as close to each other as possible ($\sim$ 5 cm). The AC drive coils provide a field of 5.8 G/A.

Finally, to cancel stray magnetic fields and to shift the magnetic minimum of the QP during transport and loading, shim coils made from enamelled copper wire surround the science cell. They provide bias fields in all three directions (3.4 G/A, 4.0 G/A and 7.6 G/A along x (E-W), y (N-S) and z (U-D), respectively), where no difference in field strength was measured between the MOT position and the ring position. A summary of important coil properties can be found in Table 6.1, Figure 6.13 shows the 3D side of the setup with the coils in place, surrounding the science cell.

Coils	N	R (cm)	S (cm)	dB/dz (G/cm/A)
2D QP	45	11.4 (l), 5.5 (w)	9	2.4
3D MOT	16	2.4	5.3	1.57
Transport	20	5.5	9.6	0.53
QP	20	2.7	6.8	1.21
AC drive	34	1.8	4.55	5.76 G/A

Table 6.1: Important coil properties for the second generation experiment: N is the number of turns, R is the mean radius, S is the separation. The 2D QP coils for the 2D MOT are rectangular with the values for length (l) and width (w) given instead of the mean radius. Because the AC drive coils are not in quadrupole but in Helmholtz configuration, instead of the gradient the magnetic field in G/A is given.

6.2.6 Preparing the beams - optical setup

Because we are using the same atomic species,^{87}Rb , and partly the same cooling mechanisms as in the first generation experiment, much of the optical setup to prepare the beams (splitting the beams, shifting the frequencies etc.) stays unchanged. The optical setup is now divided into the 2D MOT and the 3D MOT setup. Additionally, we shine a *push beam* along the long axis of the 2D MOT, so that the atoms are pushed through the differential pumping tube and into the 3D chamber, for a better atom flux [131]. On the 3D MOT side, we setup the beams needed for cooling, optically pumping and imaging the atoms and the dipole trap beams for evaporation. The Kapitza-Dirac beams are to be overlapped with the dipole beams, to follow the same path and focus at the loading position of the ring. The beams reach the 2D and the 3D side of the setup from the beam preparation optics via fibres, which makes the individual optical setups independent from each other.

For the radiative cooling stages, we need two lasers, which are the same as for the first generation setup: one laser is tuned to the cooling transition, with parts of the light being split off and frequency shifted, to be used for optical pumping, imaging and for the push beam. The second laser is used as a repump laser, to transfer the atoms back into the cooling cycle. As in the previous setup, the different beams are frequency shifted with AOMs. The AOMs are also used for amplitude control, but additionally shutters are put into all crucial beams.

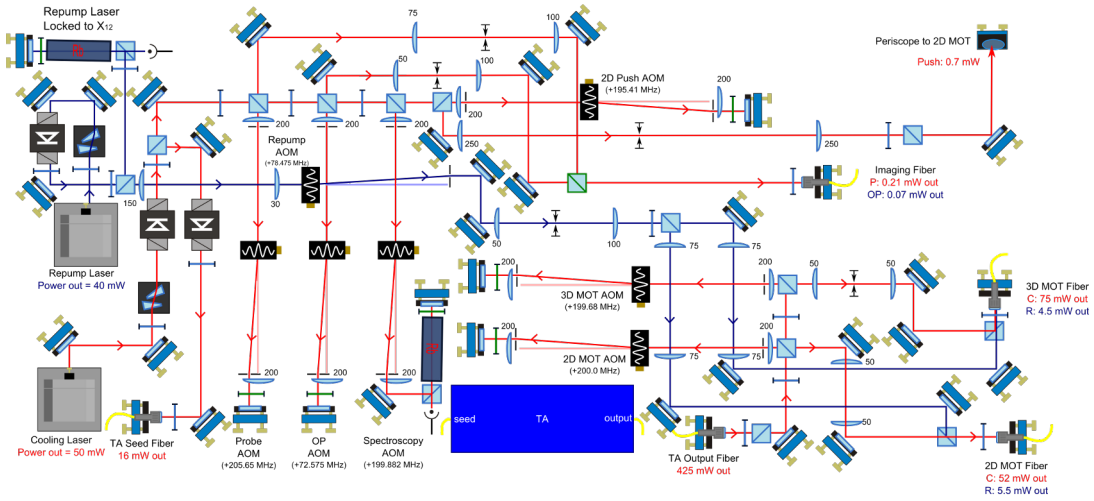

Figure 6.14: The optical setup for the preparation of the beams. The red beam is from the cooling laser, the blue beam is from the repump laser. The numbers at the lenses denote the focal lengths. Beamsplitters are either PBS (blue) or NPBS (green), and waveplates are either $\lambda/2$ (blue) or $\lambda/4$ (green).

For the probing, optical pumping and 3D MOT cooling light, we use Uniblitz shutters, while for the repump light and the push beam, we use Sunex shutters (SHT934) with a home-built drive circuit. Because we have two MOTs in this experiment, which are both reached via fibres, we need much more light than in the old experiment, and the power from the ECDL alone (50 mW) is not enough. We therefore amplify the cooling light, before it is divided into the 2D and 3D beams, using a tapered amplifier (TA) from New Focus (TA-7600). With an input power of ~ 16 mW, we saturate at an output power of ~ 470 mW, which is sufficient to supply the 2D MOT and the 3D MOT with cooling light. An overview of the beam preparation optics layout is shown in Figure 6.14, and the optical setup around the chamber for the 2D and the 3D MOT side is shown in Figure 6.15.

Imaging and optical pumping As before, we use atom absorption imaging. To be able to image the atoms in the vertical ring, we now image along the y-axis. The imaging transition is the σ^+ state ($|F = 2, m_F = 2\rangle \rightarrow |F' = 3, m_F = 3\rangle$), with a bias field being applied along y ($B_y = 5$ G, the probe beam detuning is adjusted to be resonant). The probe light, together with the OP light, reaches

the 3D side through a fibre with a power of $P_{\text{probe}} = 66\ \mu$W and $P_{OP} = 210\ \mu$W, respectively. There are then two points of interest for us: the 3D MOT position and the ring position. The probe light (together with the OP light) is therefore split so that images at both regions can be taken, see Figure 6.15 for a schematic of the imaging and OP beam path.

6.2.7 Experimental sequence

The experimental sequence is similar to the first generation experiment. Due to the design of the chamber, several extra steps have to be added, such as creation of the 2D MOT, from which the 3D MOT is loaded, and the magnetic transport. For BEC creation, we additionally need evaporation as an extra cooling stage to reach degeneracy. The sequence is then:

1. 2D MOT
2. 3D MOT loading from 2D MOT
3. Molasses
4. OP
5. Loading the QP trap and ramping up the magnetic field gradient
6. Magnetic transport in x and y, then QP trap at ring loading position
7. AC drive field to create ring trap and loading

Additionally, we evaporative cool the atoms for the creation of BEC. We now look at the different steps in the sequence separately.

6.2.7.1 Step 1 - 2D MOT

In the first experimental stage, a 2D MOT provides a cold atom reservoir from which the 3 MOT is loaded, which was first proposed by [121], a good characterisation can also be found in [131]. A 2D MOT cools and traps the atoms in the same way as a 3D MOT in two dimensions, but there is no confinement and no direct cooling along the third dimension, the x-axis. The free axis is aligned

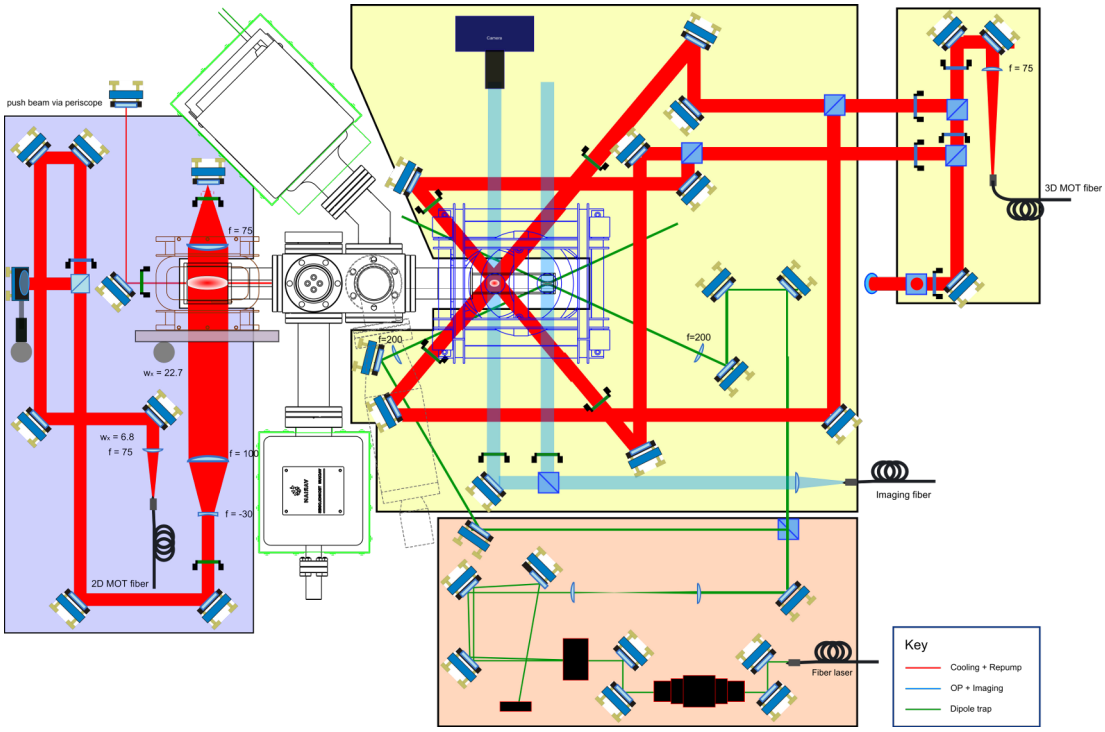

Figure 6.15: Optical setup around the 2D MOT cell and the science cell: the 2D MOT cell is on the left, with the horizontal 2D MOT beams shown. The 3D MOT beams are on the right hand side, to create the MOT inside the science cell, where the 3D MOT beams cross. Also shown are the dipole trap beams (from fibre laser, bottom right), which are crossed inside the copper ring in the science cell. The imaging and OP beam is indicated in transparent red.

with the differential pumping tube to the 3D chamber, so that cold atoms can transfer through. For an increased flux, a push beam aligned along the centre of the tube gives the atoms additional momentum to pass through the tube to the other side [131]. To maximise the time the atoms spend inside the cooling region of the 2D MOT, its volume is increased by using big, elliptical beams and a cylindrically shaped magnetic potential from rectangular quadrupole coils. The geometry is therefore extended to be elongated along the unconfined axis to maximise the cooling, from the open ends the atoms can directly transfer through the differential pumping tube into the 3D chamber. To create the elongated magnetic quadrupole field, two pairs of rectangular coils as described in Section 6.2.5 are used, with current from an Agilent power supply (HP6621A). By looking at the

loading rate of the 3D MOT, the alignment of the magnetic minimum along the centre of the differential pumping tube is optimised, for which we use the shim coils.

The light for the elongated cooling volume of the 2D MOT comes from two elliptically expanded, counter-propagating beams. For a schematic of the (horizontal) beam path, see Figure 6.15. To start with, the light enters the 2D setup from a fibre, the beam contains cooling and repump light, with 52 mW of cooling light and 5.5 mW of repump light. Here, the beam is expanded by nearly a factor of 10 to a beam waist of 6.8 mm. To provide cooling along z, a vertical beam is split off with a PBS. The horizontal and the vertical beam are then guided towards the entry faces of the cell. Before they reach the cell the beams are expanded with a cylindrical telescope ($f_1 = -30$ mm, $f_2 = 100$ mm), to give collimated, elliptical beams with a beam waist of 22 mm along the long axis (x) at the position of the 2D MOT. The beam is reflected after it passes the cell, for which we build a cat-eye configuration: directly after leaving the 2D cell, the light is focussed by a cylindrical lens ($f_3 = 75$ mm) onto a mirror, which reflects the beam back to the cell. A $\lambda/4$ waveplate is placed in front of the mirror, which is double-passed to change the polarisation of the light (as for the 3D retro MOT in the first experiment). An image of the 2D MOT is shown in Figure 6.16 (a).

Due to the large separation between 2D and 3D MOT combined with the relatively short 2D MOT cooling region, there is an large divergence in the 2D atom beam, which makes flux measurements with a probe beam (as done in [131]) challenging. Instead, we use the 3D MOT loading rate to optimise the 2D MOT parameters. We find the best 3D MOT loading rate for a 2D gradient of $\mathrm{d}B/\mathrm{d}z = 18$ G/cm, with a cooling light detuning of $\Delta_{\mathrm{2D}} = -14$ MHz. Additionally to the 2D MOT light, the push beam is implemented on the 2D side, to push the atoms through the centre of the differential tube and increase the flux. It is optimised to have a detuning of $\Delta_{\mathrm{push}} = -5$ MHz and a power of $P_{\mathrm{push}} = 500$ μW.

6.2.7.2 Step 2 - 3D MOT

The quadrupole field is produced by the MOT coils, described in section 6.2.5, the current comes from a second Agilent power supply (N8733A). Shim coils provide

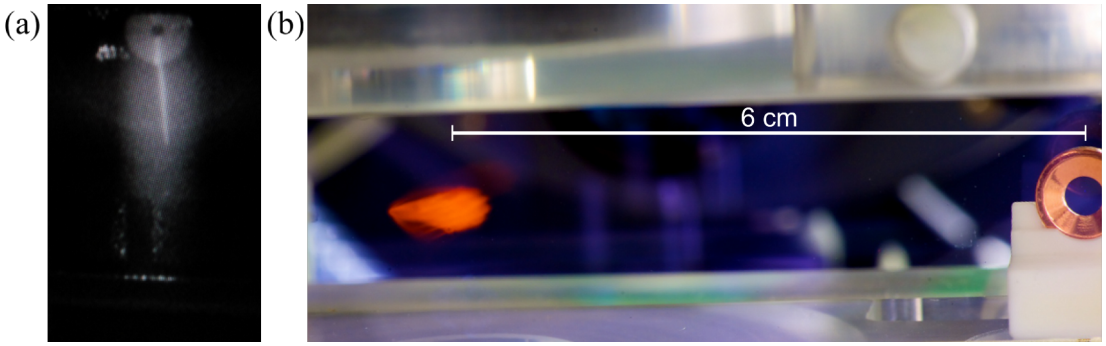

Figure 6.16: Fluorescence image of the cylindrical 2D MOT with the differential pumping tube with its aperture in the background (a). Fluorescence image of the 3D MOT in the science cell, with the ring at the other end of the cell (b), image with kind permission from G. Fleming, copyright University of Strathclyde.

local as well as external control over bias fields to cancel out stray magnetic fields. On the 3D side of the optics setup, the cooling and the repump light exits the fibre with a power of 75 mW and 4.5 mW, respectively. The beams are expanded directly after the output to have a $1/e^2$-waist of 9.8 mm. In contrast to the first generation setup, we do not use a retro-MOT. Instead, we split the the light into six separate beams, which allows for better intensity balance. The four horizontal and two vertical beams are overlapped at the centre of the MOT coils, Figure 6.15 shows a schematic of the horizontal beam path. An image of the 3D MOT in the science cell, where the distance to the copper ring is visible, is displayed in Figure 6.16 (b).

In a saturated MOT, we can capture over 3×10^9 atoms. An example fill curve is shown in Figure 6.17, with a saturation time of 3.9 s and a lifetime of 11.2 s. After optimisation, we have a MOT lifetime of $\sim$ 20 s, which is in agreement with $< 10^{-10}$ Torr background pressure (compare [132]). In the experiment, we saturate the atom number loaded in the QP trap, before we reach saturation of the MOT. We therefore don't fill the MOT completely, typically we load the MOT with $N \approx 9 \times 10^8$ atoms. We find an optimised cooling light detuning at -14 MHz, and we measure a MOT temperature of 230 μK. With an atom density of 5.5×10^{10} cm^{-3} (calculated from the atom number divided by the volume of an ellipsoid obtained from Gaussian fits to the absorption image), the phase space

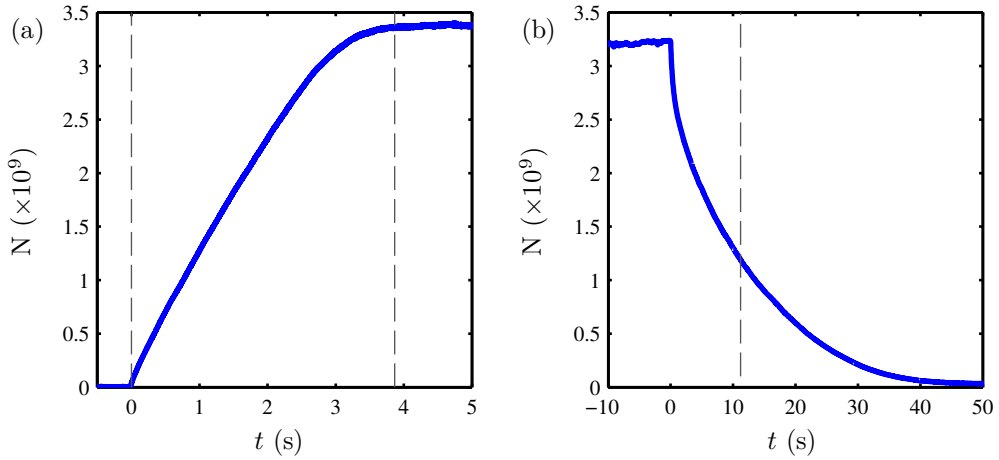

Figure 6.17: 3D MOT loading curve (a) and MOT decay (b). The atom number is calculated from the fluorescence, which is captured on a photodiode. The fill time ($\tau_{\text{fill}} = 3.9$ s) and the lifetime ($\tau = 11.2$ s) are indicated with grey dashed lines. An optimised MOT has a lifetime of ~ 20 s.

density (PSD) of the cloud during the MOT stage is estimated to be 1×10^{-7} (for transition to degeneracy, the PSD needs to be ~ 2.6).

6.2.7.3 Step 3 - Optical molasses

The molasses phase cools the atoms to $\sim$ 10 μK. For this step, the intensity is decreased and the light is far detuned, for a colder sample. To investigate the cooling time during optical molasses further, we measure the cloud temperature as a function of molasses duration, $\Delta t_{\text{Molasses}}$. The results are shown in Figure 6.18 (a). We additionally compare two different ways to set the duration with which the detuning is linearly ramped from the MOT value ($\Delta = -14$ MHz) to the molasses value ($\Delta = -60$ MHz), $\Delta t_{\text{Det.}}$:

1. Duration of detuning ramp is fixed, $\Delta t_{\text{Det.}} = 10$ ms, and only the molasses time is changed

2. Duration of detuning ramp is changed with molasses time, $\Delta t_{\text{Det.}} = \Delta t_{\text{Mol.}}$.

The results show that to achieve maximum cooling (8 μK), a minimum time of 6 ms is necessary. It also does not make much difference whether the detuning

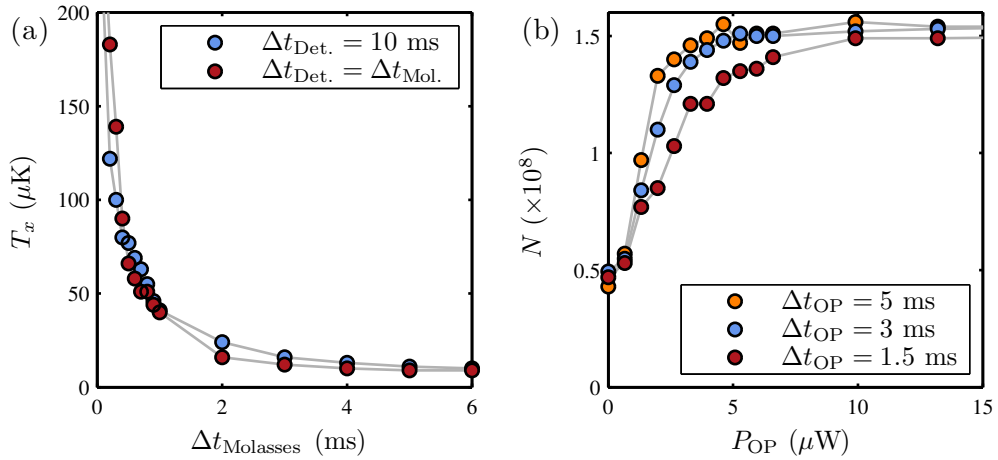

Figure 6.18: The molasses duration, $\Delta t_{\mathrm{Molasses}}$, is varied to find the minimum duration necessary for the maximum cooling (a). The lowest temperature we obtain in the molasses phase is $T_x = T_y = 8 \pm 2$ μK (shown here is only the temperature T_x). With a detuning of -60 MHz, the minimum duration is $t_{\mathrm{Molasses}} = 6$ ms, regardless whether the detuning ramp duration is fixed (blue) or variable (purple). The optical pumping power necessary to maximise the atom number depends on the OP duration (b). For durations of 5 ms (orange), 3 ms (blue) and 1.5 ms (purple), the atom number is plotted over OP beam power. The atom number increases by a factor of 3, and we note that longer times need less OP power, but heat the atoms.

ramp is fixed, or whether its duration varies with the molasses timing. We therefore decide on a changing detuning ramp and set the molasses duration to 6 ms. We also observe that with all magnetic fields cancelled, we are able to directly load atoms from the 2D MOT into the molasses.

6.2.7.4 Step 4 - Optical pumping

We want to magnetically trap the atoms, and to populate the trappable $|F = 2, m_F = +2\rangle$ state, we use the same optical pumping (OP) scheme as in the first experiment (σ^+ light resonant to $|F = 2\rangle \rightarrow |F' = 2\rangle$).

A small y bias of 1 G is applied to define a quantisation axis for the σ^+ polarisation, it is ramped down linearly during the first 1 ms of the QP phase. The atom number as a function of the OP duration and the OP beam power is

shown in Figure 6.18 (b). We can increase the atom number by a factor of ~ 3. Although a short OP duration needs slightly more OP power, long OP causes cloud heating (up to 200 μK for $\Delta t_{\mathrm{OP}} = 5$ ms and $P_{\mathrm{OP}} = 66$ μW when measured in the QP), so much that it even changes the cloud shape. This heating could be an effect of unwanted transitions being driven, or of the unbalanced beam from one direction. We therefore implement OP over a duration of $\Delta t_{\mathrm{OP}} = 0.5$ ms with $P_{\mathrm{OP}} = 18$ μW. Having some (more than ≈ 0.3 mW) repump light on during the OP phase increases the atom number slightly, and we keep the power at half of that used during the MOT phase. After the OP, the temperature of the cloud before being captured in the QP trap, is measured to be $T = 20$ μK, which is hotter than the molasses temperature. However, this does not lead to any noticeable difference in temperature for atoms in the QP trap.

6.2.7.5 Step 5 - Loading the QP trap and ramping the magnetic field gradient

With the atoms optically cooled and pumped into the trapping state, the light is now switched off and the atoms are trapped in a magnetic QP. The field is produced by the MOT coils with an increased field gradient. Because the field has been off during molasses and OP, it needs to be turned on rapidly from zero, which is described below. The overlap and mode matching determines our capture efficiency, we can capture $\sim 60\%$ of the atoms in the MOT. The lifetime in the QP is measured to be ≈ 20 s, limited by background pressure. We find it to be the same at the position of the MOT coils and at the position of the QP coils, after transport.

Heating and sloshing after loading the QP How well the centres of MOT, molasses and QP trap overlap can be estimated by looking at the sloshing and breathing of the atomic cloud after the transfer, e.g. from the molasses into the QP trap. The molasses centre is the same as the MOT centre, with a small shift due to gravity.

For a better measure of the size and shape of the cloud, which is necessary to study the sloshing and breathing, the atomic cloud can be imaged with high detuning (20 MHz). We image the atoms in the QP in steps of few ms, directly

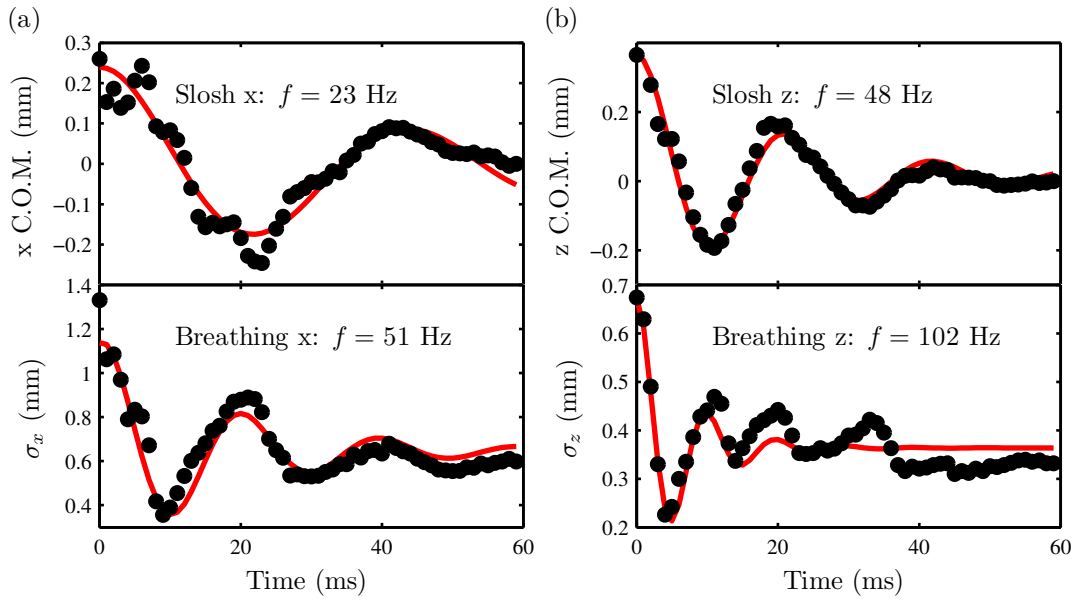

Figure 6.19: Sloshing and breathing of atomic cloud after the transfer from the molasses into the QP trap: (a) sloshing and breathing in x , (b) sloshing and and breathing in z. The frequency for the sloshing and breathing in z is twice of the frequency in x due to the QP magnetic field gradient, which is twice as strong in z as in x.

after the transfer from the molasses. This shows the oscillations of the atomic cloud's centre of mass (C.O.M.) position and of its width, σ, in the x and z-direction. Oscillations of the C.O.M. position are "sloshing" and oscillations of the cloud's width are "breathing" modes. Both are damped oscillations and can be fitted with an exponentially damped cosine, with frequencies in the region of tens of Hz that die off after tens to hundreds of ms. An example of the sloshing and breathing of an atomic cloud after being loaded from the molasses into the QP trap is shown in Figure 6.19. The frequencies for the sloshing and breathing in z (48 Hz and 102 Hz, respectively) are approximately twice of the frequencies in x (23 Hz and 51 Hz, respectively) due to the QP magnetic field gradient, which is twice as strong in z as in x.

Although sloshing and position shifting can be minimised by optimising the matching between the MOT and QP centres in the z and x direction, we are blind to the sloshing in y direction due to our imaging plane. Neither the increase

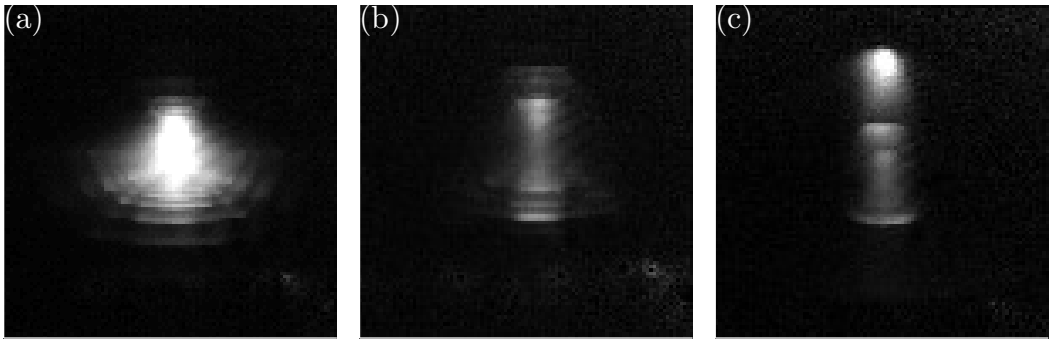

Figure 6.20: Images of a distorted cloud of atoms in the QP trap. Panel (a) shows a very hot cloud of atoms after long OP duration, while (b) and (c) show examples of different ramping duration and shape when switching on the QP field after the molasses (without OP). This slow ramping of the magnetic field gradient may have left the atoms in different magnetic sub-levels, leading to atoms being expelled from the trap.

in atom number nor the temperature are sufficiently accurate to optimise the y direction, so it is left unchanged (we do observe atom loss when creating a large displacement using strong y-bias of several Gauss, which indicates a large displacement of the two magnetic trap minima).

Ramping the magnetic field gradient Our first approach to switching the magnetic field on after the molasses/OP phase was to snap the magnetic gradient to the MOT values and then apply a slow ramping process, to be as adiabatic as possible. But after trying different ramps (different ramping functions, times and final gradients), we were always left with a distorted cloud, showing signs of splitting and expulsion out of the QP trap. Examples of those distorted clouds are shown in Figure 6.20. We suspect the splitting to be due to different m_F-states, which would experience different forces from the magnetic field and could be accelerated out of the magnetic trap.

In the end, an instantaneous switch-on is the best solution and leaves us with the roundest cloud of atoms in the QP trap (this matches ramping times used in [133]). To optimise our switching and make it as fast as possible, we have to circumvent the time-delay caused by the FET control-circuit, by sending a

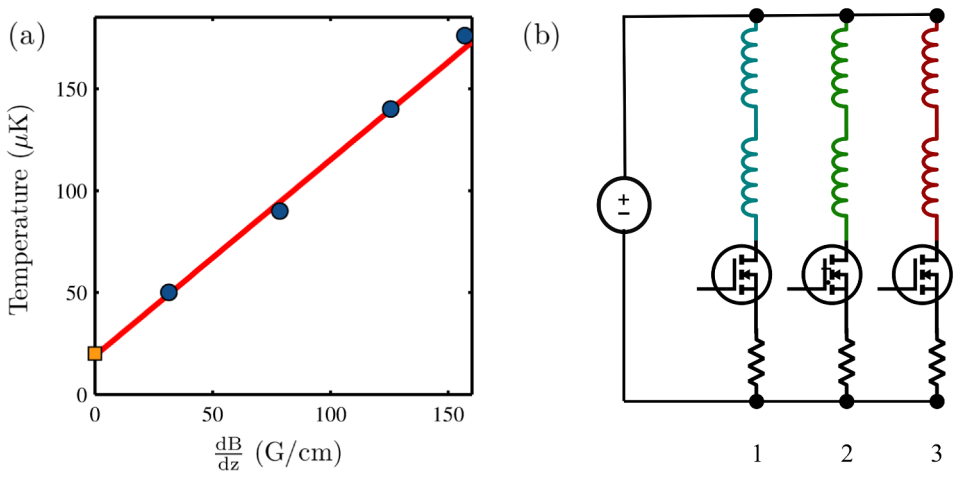

Figure 6.21: (a) The temperature of the atoms in the QP trap varies linearly with the QP gradient. The yellow square marks the temperature of the cloud after OP, before the QP. (b) Layout of the current control in the coils: the MOT coils (1), transport coils (2) and QP coils (3) are run in parallel, with individual FET control circuits and current probes.

short large voltage spike (equivalent to demanding 300 A from the circuit). We then change the voltage to match the current we actually want, e.g. 100 A. The timing is adjusted to produce the smoothest curve with the smallest ringing, which reduces the switch-on time for a current of 100 A ($\mathrm{d}B/\mathrm{d}z = 157$ G/cm) from 4 ms to 0.5 ms. In contrast to previously thought, the fast switching does not introduce additional heating: the temperature only depends on the magnetic gradient and not on the duration of the switching (over the range 0.5 ms to 4 ms). The increase of temperature with magnetic field gradient is shown in Figure 6.21 (a). Over this range, it can be fitted linearly. Indicated is also the measured temperature after the OP, before the QP field is switched on, which matches the fit very well. We ramp the magnetic field gradient to a final value of $\frac{\mathrm{d}B}{\mathrm{d}z} = 100$ G/cm to prepare for magnetic transport.

6.2.7.6 Step 6 - Magnetic transport

From the starting position (MOT coils centre), the atoms in the QP trap are moved along x to the position of the ring (QP coils centre). The magnetic trans-

port is realised using three overlapping sets of coils (MOT coils, transport coils and QP coils) in quadrupole configuration to shift the magnetic minimum by changing the current distribution in the coils, as described in Section 6.1.

Current control All coils for the magnetic transport (MOT coils, transport coils and QP coils) are run in parallel off the same power supply (Agilent N8733A). The current in each coil pair is controlled via a FET circuit, similar to the one used for the MOT coils in the first generation experiment, a schematic of the layout is shown in Figure 6.21 (b). A bank of five FETs in parallel is used for each coil pair to be able to cope with the large power drops. These occur during the magnetic transport at times when the current is at a low point but the voltage is high. The FETs fail at a total power of $P \geq 1.8$ kW, and those power peaks have to be avoided during the current sequence. As a result, the voltage is regulated together with the current, reducing it enough to remove unnecessary power dissipation while sustaining the required current at each point during the magnetic transport sequence. Due to the high currents (> 200 A), the hollow, water cooled copper tube sense resistors from the first experiment feedback circuit heat up and are therefore replaced with Hall sensors (Honeywell CSNM).

Water cooling The 3D MOT coils and the transport coils are cooled by the chilled circulating water which is supplying to the labs. The QP coils, on the other hand, carry high currents for long durations (tens of seconds), and the cooling circuit water pressure is insufficient to provide the required cooling for the QP coils. Cooling is installed by using refurbished dye-circulaters for enhanced water pressure. The water from the dye circulator for the QP coils is actively cooled by running the return water through a homebuilt heat exchanger.

Realisation As the current distribution shifts from MOT coil to transport coil to QP coil, the moving magnetic field accelerates the atoms and transfers them from the MOT position to the ring position where they come to a halt. The transport sequence is calculated to provide a constant magnetic field gradient, $\frac{\mathrm{d}B}{\mathrm{d}z} = 100$ G/cm, and to keep acceleration smooth (see Figures 6.2). Setting maximum values for velocity and acceleration determines the current amplitude

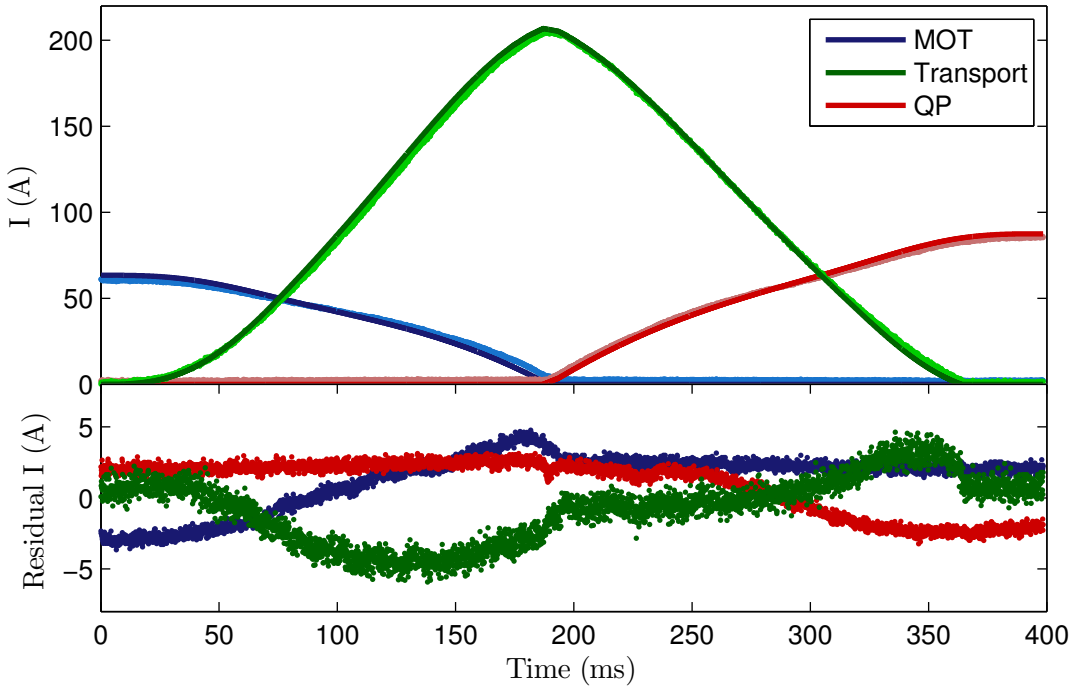

Figure 6.22: Comparison of theoretical and measured current in the MOT coils (blue), transport coils (green) and QP coils (red). The theoretical curves (dark) are overlayed with the measurements (bright). The residuals $I_{\mathrm{exp}} - I_{\mathrm{th}}$ are shown, which have a maximum of < 6 A.

in the coils with transport time and the total duration of the magnetic transport (compare Figure 6.3). When comparing how well the current follows those calculations, by monitoring the Hall sensors, we find that it matches well (residuals are within ± 6 A). Figure 6.22 shows the calculated and the measured current for all coils, together with the residuals.

Before moving the atoms the whole distance to the ring, the magnetic transport is first tested by imaging the cloud at the MOT position: the magnetic fields are set to shift the atoms over a short distance (several mm) and then return the cloud to the initial position. To find the exact ring position, we move the atoms by a distance Δx and look at the returning atom cloud. We keep about 80% of the atoms (8×10^7 out of 1.1×10^8 atoms), until we hit the ring at $x = 62$ mm and all atoms are lost. At that point, a movement in y around the ring is implemented using a y bias field from the 3D shim coils. We redirect the atoms such that they

are about 2σ (~ 2 mm) away from the ring in y, before they reach the edge of the ring in x. Once this is implemented, a camera confirms the successful manoeuvre around the ring. The y bias is then reduced and the atoms follow the magnetic field minimum to the centre of the ring. After the transport the temperature is measured to be ~ 140 μK (before transport: $T \approx 100$ μK), and the tuning of $v_{\max}$ cm/s and $a_{\max}$ m/s^2) is not critical. We therefore decide on a comparably fast transport, with $v_{\max} = 20$ cm/s and $a_{\max} = 4$ m/s^2, so that atom loss due to background scattering can be minimised, resulting in a transport duration of < 400 ms. After the transport, the QP trap is prepared for transferring the atoms into the ring trap. The gradient is increased to ~ 200 G/cm, thereby reducing the cloud's size. The atom cloud centre is positioned onto the ring trap using the x and z bias fields.

6.2.7.7 Step 7 - AC drive field and ring trap

The AC drive coils are aligned co-axially with the copper ring in a Helmholtz configuration to provide the magnetic field needed to create the ring trap. With the ring now mounted vertically, the AC coils are perpendicular to the QP coils, which reduces the EMF from the AC field in the QP coils. Due to the new geometry of the ring, we require a higher drive frequency of ~ 50 kHz. We use the audio amplifier from the first generation setup (Behringer Eurorack EP1500) to drive the AC field. The amplifier is designed to deliver up to 600 W into a 2 Ω load. We therefore have to tune the resonant circuit (refer to Figure 3.6 for a diagram) to match the required drive frequency and the output load. We change the capacitors to have $C = 247$ nF, with which a resonant frequency of $f_0 = 44.7$ kHz is achieved, and the resistors on the bank are adjusted to $R = 0.53$ Ω, which in combination with the other components of the circuit gives a total resistance of $R_{\text{load}} = 1.96$ Ω.

To adjust the resonant circuit, the resonant frequency is obtained from the impedance, Z, as a function of frequency $f = \omega/2\pi$ (f is changed at the function generator (FG)):

$$|Z| = |R + i(\omega L - \frac{1}{\omega C})| \ . \tag{6.5}$$

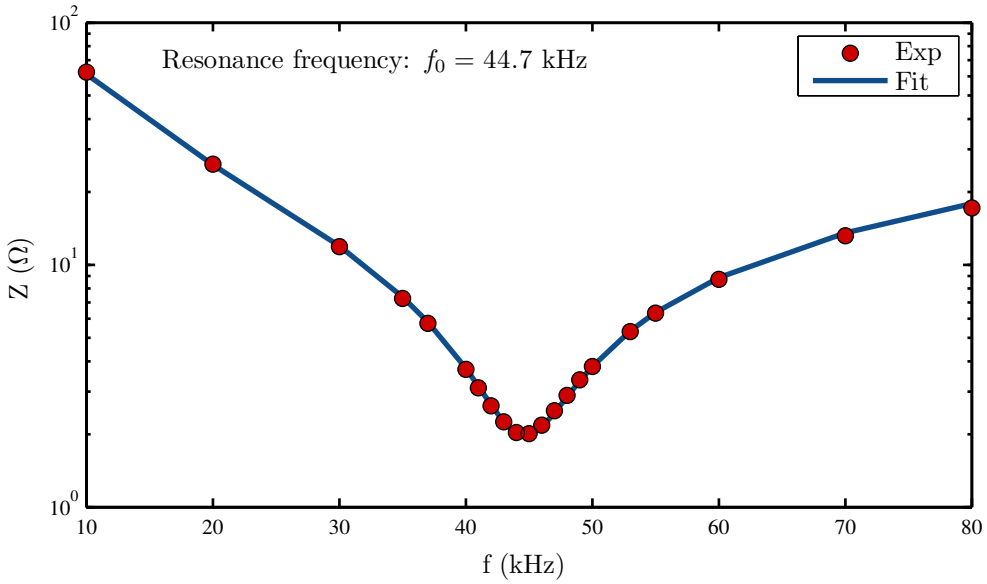

Figure 6.23: The impedance is measured as a function of drive frequency, and the values for L and C are extracted by fitting Equation 6.5. The resonance frequency is then $f_0 = \frac{1}{2\pi\sqrt{LC}} = 44.7$ kHz.

For $f = f_0$, the impedance is at its minimum. At each frequency, Z is calculated from $Z = V_s/I$, with the current $I = V_R/R$, where V_R is the voltage across the resistors and $R = 0.53\ \Omega$, and with the source voltage V_s, which is measured after the amplifier (FG voltage is constant for all measurements). The impedance curve for the optimised circuit is shown in Figure 6.23. From the fit of Equation 6.5 to the data, we extract $L_{\text{fit}} = 51.5\ \mu$H and $C_{\text{fit}} = 246.6$ nF (close match to the actual value for C), and the resonant frequency is calculated as $f_0 = \frac{1}{2\pi\sqrt{LC}} = 44.7$ kHz. The final resonant circuit has a Q of 7.4, corresponding to a frequency bandwidth of $\Delta f \approx 6$ kHz.

With an output power of up to 600 W, the audio amplifier and the resistor bank must be water cooled (see Figure 3.7). To test the power across the components, we increase the input voltage from the function generator. Just before the internal overload protection causes clipping of the signal, we measure the the total power to be 519 W (from the measured current and the source voltage), of which 384 W is in the coils. This sets the limit for the

available current in the coils. At this point, the current has an amplitude of $I_{\mathrm{pk}} = 22.78$ A, we therefore have a maximum magnetic field from the AC drive coils of $B_{\mathrm{max}} = 5.76$ G/A $\times$ 22.78 A $\approx$ 130 G. The best harmonic performance is achieved, when using the amplifier at full gain (+32 dB) and attenuating the frequency input.

Ring trap Once the atoms in the QP trap are shifted to the ring trap position, we switch on the AC drive field with an amplitude of $B_0 = 130$ G, while the QP field gradient is reduced to 10 G/cm, to provide the magnetic zero offset field. Figure 6.24 (a) shows the ring trap loaded at the top. The atoms fill the ring completely within 30 ms; the trap has a radius of $\sim$ 1.8 mm. Loaded at the bottom, which is shown in Figure 6.24 (b), the atoms start to spread around the ring, but gravity pulls the atoms back and they refocus at the loading position. Both of these configurations are suitable for atom interferometry, as shown in Figure 6.5, which can be explored in future experiments with the ring trap.

6.2.7.8 Additional step: evaporation and creation of a BEC

The results in this Section are very recent – I am happy to say that the BEC has been created just in time before concluding the work on this thesis. This means that this Section does not include an extensive characterisation of the BEC.

We have successfully loaded cold, but thermal atoms into the vertical ring trap. In order to use the ring for interferometry with BEC, we need to implement the final cooling stage before loading the atoms into the ring trap. Cooling to degeneracy is accomplished by evaporative cooling in a hybrid trap, as described in Section 6.1.2. In this two-part process, RF-evaporation in a magnetic trap reduces the temperature until Majorana losses become important. Then the atoms are transferred into a crossed dipole trap, in which they are further evaporated by lowering the trapping potential, for which the intensity of the dipole beams is reduced.

For the RF-signal, a small coil (1 turn, $r = 2.5$ cm) is placed close to the atoms. With an Agilent function generator (33522A), the frequency of the RF signal is ramped exponentially from $f_i = 25$ MHz to $f_f = 4.5$ MHz, over the duration $t_{\mathrm{evap.}} = 5$ s, thereby spin flipping the most energetic atoms out of the

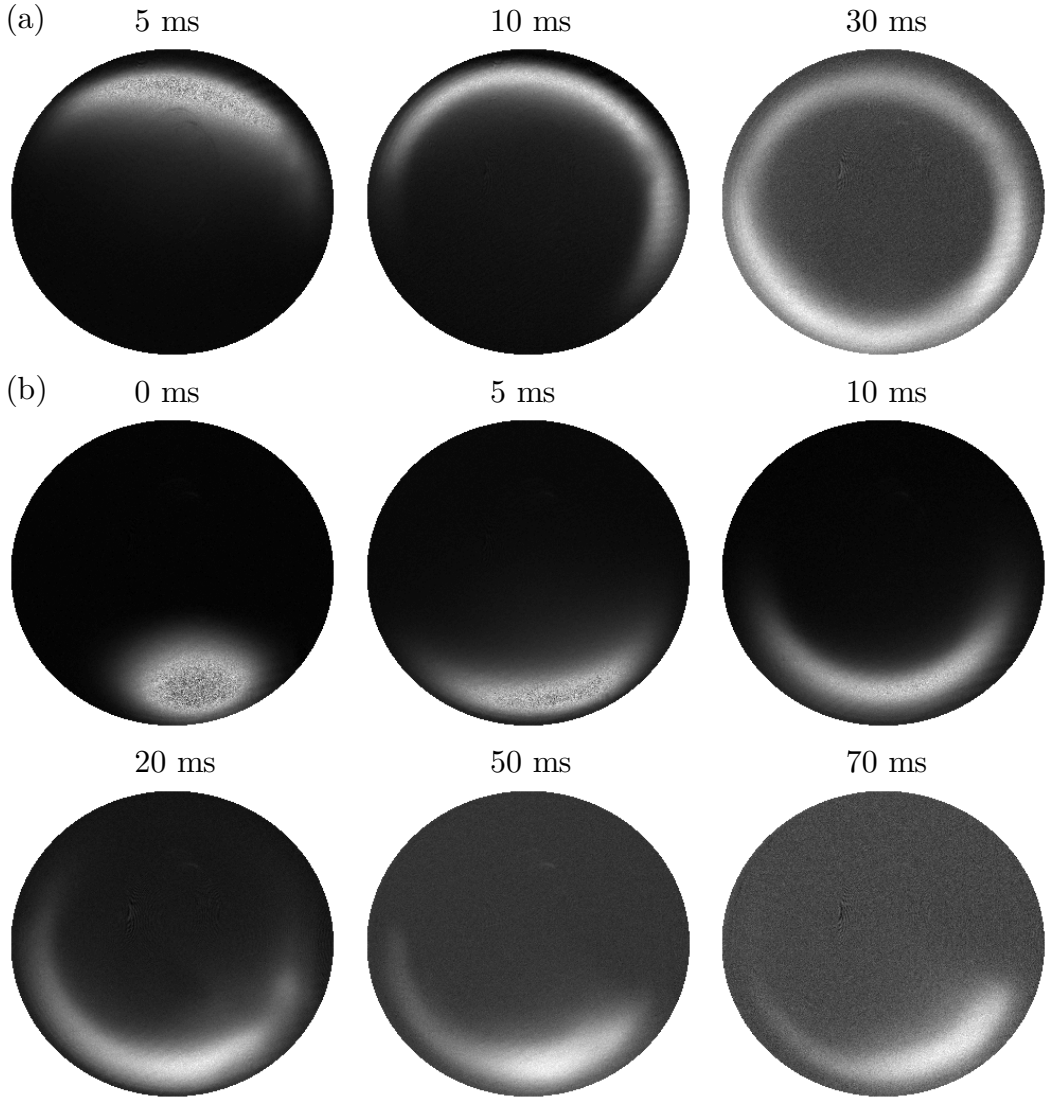

Figure 6.24: Cold atoms in the vertical ring trap. (a) When loading at the top, we can see the atoms filling the ring completely after 30 ms (b) Loading at the bottom leads to spread around the ring, until gravity causes the cloud to re-focus at the starting position.

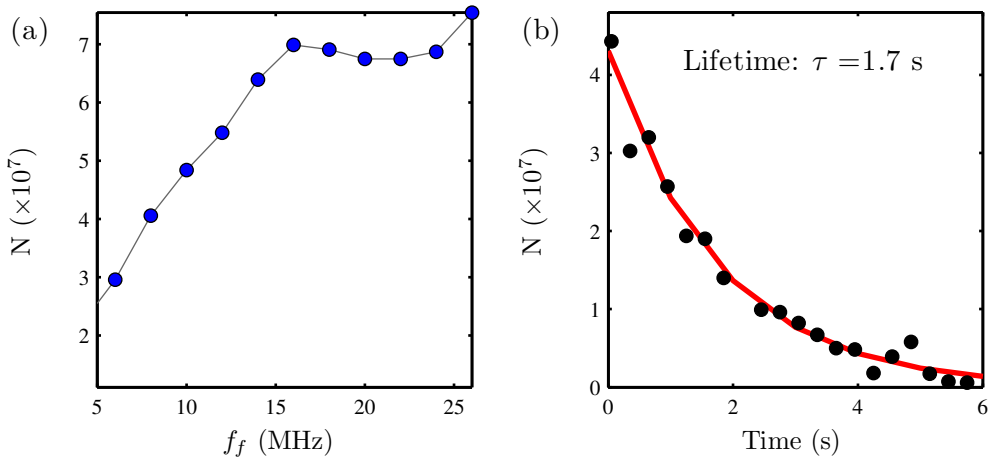

Figure 6.25: RF-evaporation characteristics: (a) the atom number decreases as a result of the final RF frequency, f_f. After RF-evaporation, the cloud temperature is low enough that Majorana losses become significant, and the lifetime of the QP trap decreases from 20 s to 1.7 s.

QP trap. To achieve a good elastic collision rate for re-thermalisation, the QP is tightened to 200 G/cm before the evaporation.

At the start of the process, the atoms have a temperature of 240 μK in the QP, with a PSD of the order of 10^{-8}. At the end of the RF-evaporation, the temperature is 40 μK, with a PSD of $\sim 10^{-5}$. Depending on the final frequency of the RF-ramp, the atom number decreases as more and more atoms at high energies are removed, as shown in Figure 6.25 (a). From the atom number and the phase space density at the start and the end of the RF-evaporation we estimate the evaporation efficiency, using Equation 6.4:

$$\gamma_{\mathrm{RF}} = \frac{\ln(10^{-5}/10^{-8})}{\ln(2\times 10^7/7\times 10^8)} = -1.94\ .$$

At this temperature and density we see significant Majorana losses, this affects the atom lifetime in the magnetic trap, reducing it to 1.7 s, see Figure 6.25 (b).

The dipole beams are then switched on and the atoms are transferred into the crossed dipole trap, with the QP field reduced to $\sim$ 11 G/cm, which merely supports the atoms against gravity.

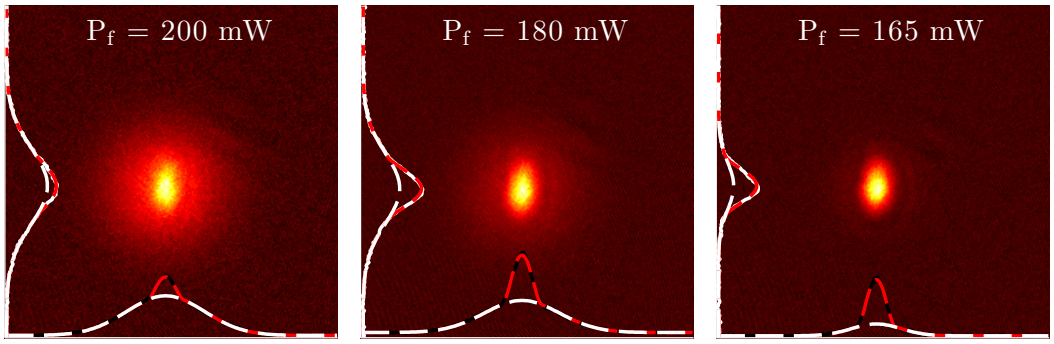

Figure 6.26: The transition to degeneracy is reached after evaporation in a dipole trap. The condensate fraction increases when the final dipole beam power is lowered, here $P_f = 200, 180$ and 164 mW.

We use a $\lambda_{\mathrm{DP}} = 1070$ nm fibre laser (IPG Photonics YLM-10-LP-SC) for the dipole trap. The beam from the fibre output passes an AOM for intensity control, is then expanded and split between two beam paths, see Figure 6.15. The beams are focussed to a spot size of ~ 45 μm, at which they are overlapped with the position of the QP trap, with an angle of $\sim 130°$ between them. We start with high power in the beams (3 W in each beam), to give a deep enough trapping potential ($U_{\mathrm{DP}} \approx 540$ μK). The power is then exponentially decreased to 165 mW ($U_{\mathrm{DP}} \approx 30$ μK) over a duration of 5 s. For powers around 200 mW, we start to see the characteristic spike on top of a Gaussian atom distribution, which is the degenerate fraction of atoms. The condensate becomes more dominant for lower beam power, see Figure 6.26, where the condensate fraction is calculated to be $N_c \approx 16, 40$ and 70 % for $P_f = 200, 180$ and 165 mW, respectively. For $P_f = 165$ mW we are left with $\sim 4 \times 10^4$ degenerate atoms. A ^{87}Rb BEC is born.

Chapter 7

Summary and outlook

We have presented the experimental realisation of an inductively coupled magnetic ring trap for cold atoms. The idea is to use an AC magnetic field to induce a current in a conducting loop, which produces a secondary magnetic field. The two fields cancel in a ring, to create a potential minimum. With the AC magnetic fields being of high enough frequency to operate in the TOP trap regime, the atoms are trapped in the time-averaged minimum. To avoid Majorana losses, we offset the magnetic zeroes at the trap minimum with an axial magnetic bias field. Ultimately, we want to use the ring trap for atom interferometry and for the study of degenerate gases (BEC).

In the first experiment, we showed that the concept of the inductively coupled magnetic ring trap works, which allows us to produce a toroidal atom trap without connecting wires to the conducting loop. We have transferred atoms with a temperature of ~ 45 μK from a QP trap into the horizontal ring trap. With the strength of offset bias and drive field, we can change the trap confinement and its shape: we can change the ring width between 5.3 and 4.3 mm and the width from 0.3 to 0.8 mm, by changing the bias. For strong offset fields, we even create a beamsplitter.

In the ring trap, we observe a fast decay of atom number of the order of ~ 200 ms due to residual Majorana losses where the atoms encounter the circle of death, which depends on the offset bias. The slow decay is of the order of ~ 1.3 s and due to background collisions. For cooling to degeneracy, we need a better lifetime for the evaporation process, which we take into account for the

second generation experiment. With the atoms in the ring, we probe the ring for potential roughness. We can't find any corrugation > 1 μK. With a BEC, we will be able to probe the ring trap with higher resolution.

After exploring the ring trap, the second generation experiment is built. We implement changes to the setup to have higher vacuum for a better lifetime (~ 20 s in the QP trap) and improve the conditions for future experiments. The copper ring itself is smaller, to create a trap with a radius of ~ 1.8 mm. It is also mounted vertically. In doing so we allow for faster orbit times around the ring when considering atom interferometry experiments. We have successfully transferred cold, thermal atoms into the second generation ring trap. The atoms can be loaded either at the top or at the bottom, which makes the geometry flexible. Besides that, BEC has been created at the loading position of the atoms. This shows us that we have created suitable conditions for BEC in the ring. Future work will include to load the BEC into the ring trap and to use the atoms for interferometry experiments. With the vertical mounted ring, we can provide smooth, symmetric and guided arms of an interferometer. The next step is to set up an interferometer with BEC, to measure h/m and the fine structure constant α. To further investigate atom interferometry, the use of ^{40}K for DFG experiments is prepared. A dual-species trap enables interference with fermions, for comparison with BEC and to improve the measurement accuracy. In a horizontal configuration, the ring trap can also be used for Sagnac interferometry, for which it provides a large enclosed area with compact experimental dimensions.

We have seen from the transition from generation 1 to generation 2 that the trap is scalable. We are now limited by the scaling laws for the AC drive field and Larmor frequencies. A solution lies in the use of RF-dressed states, which needs further investigation. When finding a way to decrease the trap size further, the properties of the inductively coupled trap would be suitable for integration on atom chips, where the suppression of potential roughness and edge effects becomes more important. With a small enough trap radius, superfluid properties and persistent currents can be studied.

Appendix A

Induced current

The induced current in the copper ring can be calculated from Equations 2.16 and 2.13, it follows the procedure in [102]:

$$\begin{aligned} U_{\mathrm{EMF}} &= -\frac{\mathrm{d}\Phi_{\mathrm{B}}}{\mathrm{dt}} && \text{(A.1)} \\ &= -\pi r_{\mathrm{ring}}^2 \frac{\mathrm{dB}_{\mathrm{drive}}}{\mathrm{dt}} && \text{(A.2)} \\ &= \pi r_{\mathrm{ring}}^2 \omega B_0 sin(\omega t) \ . && \text{(A.3)} \end{aligned}$$

We now use use the identity $sin(x) = -\cos(x + \pi/2)$ to get

$$U_{\mathrm{EMF}} = U_0 \times \cos(\omega t + \pi/2) \ . \tag{A.4}$$

The complex impedance allows us to obtain the current from

$$Z = \frac{U}{I} = \frac{U_0}{I_0} e^{i\delta} = |Z| e^{i\delta} \ , \tag{A.5}$$

where δ is the relative phase with which the current lags behind the EMF, which leads us to the expression $I_{\mathrm{ind}} = I_0 \cos(\omega t + \pi/2 - \delta)$. The complex impedance is $Z = R + i\omega L$ and $|Z| = \sqrt{R^2 + \omega^2 L^2}$. From this, we obtain the amplitude of the

current

$$I_0 = \frac{U_0}{|Z|} \tag{A.6}$$

$$= \frac{-\omega B_0 \pi r_{\text{ring}}^2}{\sqrt{R_{\text{ring}}^2 + \omega^2 L_{\text{Ring}}^2}} , \tag{A.7}$$

which can be simplified (see text). The phase is determined from $\delta = \tan^{-1}(\frac{\text{ImZ}}{\text{ReZ}}) = \tan^{-1}(\omega L/R) = \tan^{-1}(\Omega)$, but we now use the identity $\tan^{-1}(x) + \tan^{-1}(1/x) = \pi/2$ to get $\delta = \pi/2 - \tan^{-1}(1/\Omega)$. This finally leaves us with the current $I_{\text{ind}} = I_0 \cos(\omega t + \pi/2 - (\pi/2 - \tan^{-1}(1/\Omega))) = I_0 \cos(\omega t + \tan^{-1}(1/\Omega))$, and we define $\delta_0 = \tan^{-1}(1/\Omega)$. For our values for L, R and ω, we have a negligible δ_0. This leaves us with nearly the largest phase lag possible, which is a phase difference of π, expressed in the sign that we carry in the current amplitude.

Appendix B

Laser stability: Allan variance for master–slave diode–laser system

At visible wavelengths diodes with narrow linewidths are typically limited to a few tens of milliwatts of output power. For optical–power intensive experiments, such as the creation of Bose–Einstein condensates, higher powers allow for larger atom numbers and faster cycle times, both of which are desirable features [134]. Rather than duplicating the ECDL arrangement, an injection locked diode laser can provide a "slave" gain medium to amplify a relatively small power ($\sim 100\ \mu$W) from an existing laser set-up. A tapered amplifier (TA) provides a larger amount of power amplification at the cost of significantly larger amount of injected power, typically of the order of 10 mW [135, 136].

Here we present a system of master laser that provides seed power to a slave laser, using the lasers described in Section 3.5. We demonstrate the fidelity of the slave amplification through measurements of the Allan variance and electric field correlation function [137]. We show and characterize the further, faithful amplification of up to 520 mW for < 1 mW input of optical power from the master laser using a commercial TA with fibre input and output.

We observe a high degree of frequency stability in the master–slave and master–slave–TA configurations for timescales relevant to laser cooling experiments. Using the Allan variance and correlation function, we can see the transition from phase to frequency noise in both configurations, and we measure

additional phase noise due to the TA.

In practical use, lasers experience power losses when passing through optical elements, even in optimised systems, due to the non–perfect nature of anti–reflection coatings. The use of active optical elements, such as acousto–optic modulators (AOMs), results in some power being diverted into undesired modes. Furthermore, in many applications some finite amount of non-reusable power is required for frequency stabilization, such as for atomic or cavity spectroscopy or diagnostic purposes. Many experiments are greatly facilitated by having a surfeit of optical power. Our goal, the creation of quantum degenerate Bose and Fermi gases, requires a few hundred milliwatts of power for optimal number production and repetition rate. The optical power available from the laser diodes used is $\sim$ 50 mW and as such requires further amplification. We utilize two different amplifying mechanisms: an injection–locked laser diode and a commercial tapered amplifier.

For the cooling of ^{40}K we use a highly anti-reflection coated Eagleyard laser diode (EYP-RWE-0790-04000-0750), which has a tuning range $\Delta_\lambda = 40$ nm. An analysis of the diode's performance for use at 767 nm and 780 nm can be found in Nyman *et al.* [136]. Without any modification of the diode temperature the laser can be tuned over > 30 nm by rotating the angle of the diffraction grating. The threshold current and the optical power as a function of the drive current for this range, centred on 770 nm, are shown in Fig. B.1. Mode–hop free tuning ranges of 3 GHz are observed. With the wavelength tuned to $\lambda = 767$ nm (780 nm) we obtain clear saturated absorption and polarization spectra from potassium (rubidium) vapour cells at a temperature of 50°C (20°C). In operation at 767 nm the ECDL has a extra–cavity power of 30 mW of power for 60 mA current. A fibre–coupled seed power of 13 mW is required for maximum output power from the TA. For this reason we use a injection laser system as a pre–amplifier.

B.1 Characterizing amplified optical power

Two identical anti–reflection coated Fabry–Perot diode lasers, with emission wavelengths centred on 775 nm, are used in the present experimental setup. The first, "master" laser is mounted in an ECDL configuration, as described above,

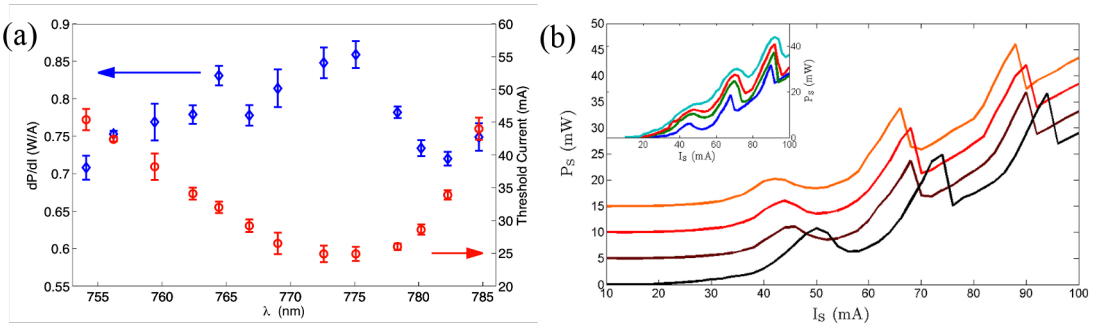

Figure B.1: (a) The variation of power with injection current (dP/dI) in the linear operating regime and the threshold current as a function of wavelength. (b) Output behaviour of the injected laser as a function of injection current for increasing temperature of the slave diode: black $T = 20.0°$ C, purple 20.3° C, red 20.4° C and orange 20.5° C. An offset of 5 mA was added to each curve for clarity. The local maxima shift toward lower currents for increasing temperatures. (Inset) Output power at a constant temperature with increasing input power: blue 0.3 mW, green 1.5 mW, red 3.0 mW, cyan 6.0 mW.

and a fraction of its output is injected into the second, "slave" laser. The slave laser is collimated and temperature stabilized, similar to the ECDL set–up, but without an external cavity. Both lasers have an optical isolator with better than −33 dB protection. The output from the slave laser is passed through an acousto–optical modulator (AOM), the frequency of which is controlled by a frequency generator with an internal 10 MHz clock. The frequency shifted light is combined with the output of the master laser on a non–polarizing beamsplitter (NPBS). A schematic of the setup is in Fig. B.2. The heterodyne beatnote, f_{rf}, is measured on a fast photodiode and either monitored directly or mixed down to the kHz regime with a second frequency source, phase locked with the AOM drive signal. The beatnote is recorded on a 2.5×10^9 samples–per–second oscilloscope and post–analysed in Matlab.

Amplification in a diode master–slave configuration results in $\sim$ 40 mW of power when used with drive currents below 100 mA. The power of the slave laser, P_{S}, has non-trivial dependence on the slave current I_{S}. Local maxima of the output power for varying slave currents are observed and are ascribed to weak etaloning within the slave diode, due to the finite reflectivity (quoted by the manufacturer as 10^{-4}) of the front facet. The local maxima shift towards lower

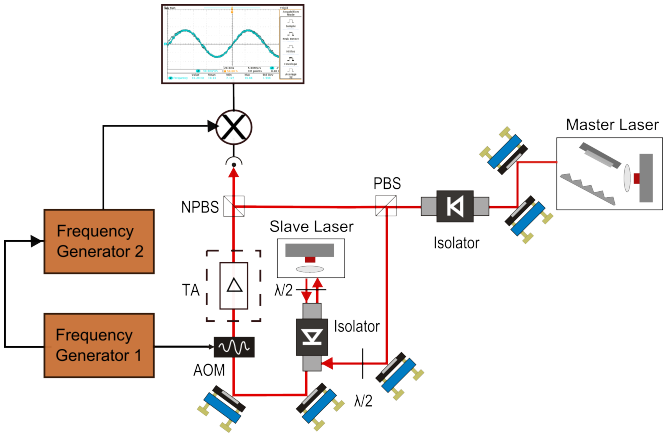

Figure B.2: The setup for measurement of the beat note. A fraction of the master laser, controlled by the half–wave plate $\lambda/2$ between the polarizing beamsplitter (PBS) and optical isolator, is injected into the slave laser. The slave laser is frequency shifted by the acousto–optical modulator (AOM) and combined with the unshifted master laser on a non–polarizing beamsplitter (NPBS) before beating both beams on a fast photodiode. The signal can be mixed down to the kHz regime and then recorded on an oscilloscope, or recorded directly from the photodiode. A second experiment includes a tapered amplifier (dashed box).

currents with increasing temperature, as shown in Fig. B.1. Increasing the seed power leads to flattening of these features, due to saturation of the gain, as shown in the inset. The slave laser temperature is stabilized to allow operation on a local maximum of the output power.

To provide further amplification, light from the slave laser was injected into a fibre–coupled, commercial tapered amplifier (TA-7600, New Focus). The phase noise of the light from the tapered amplifier, which has now been twice amplified, is interrogated in the same way as for the injection–locked diode, by beating it with the master laser.

The power from the tapered amplifier follows a more standard behaviour, increasing smoothly with drive current and injection power, as has been reported in the literature [135, 136]. The output power of our system saturates at 520 mW out of a single-mode fibre for an injected power of 13 mW.

B.2 Beatnote analysis

To characterize the stability of the slave laser response to the master laser, the Allan variance $\sigma^2(\tau)$ of the beat note between master and slave laser was obtained. There are many different modifications of the Allan variance, which can be very confusing. We are using the Allan variance in the form it was introduced in [138], being defined as

$$\sigma^2(\tau) = \frac{\langle \Delta\phi(t,\tau) \rangle_t^2}{\tau^2} \ , \tag{B.1}$$

where τ is the integration time and $\langle \Delta\phi(t,\tau) \rangle_t$ the time averaged phase difference between points separated by τ: $\langle \Delta\phi(t,\tau) \rangle_t = \langle \phi(t+\tau) - \phi(t) \rangle_t$.

The Allan variance is then obtained as follows: the beat note signal, of duration T, is divided into time bins each of length $\Delta T = M/f_{\rm rf}$ and with index t. M is chosen sufficiently large ($M \geq 10$) such that each bin contains enough cycles that the phase, $\phi(t)$, can be determined accurately by fitting a sine wave, with fixed frequency $f_{\rm rf}$ to each bin. The frequency, $f_{\rm rf}$, is known, as it is either the frequency the AOM is driven at or the mixed down frequency, as described earlier. The phase difference $\Delta\phi(t,\tau)$ for bins separated by τ is calculated for every point t of the signal and the average taken:

$$\langle \Delta\phi(t,\tau) \rangle_t = \frac{\sum_{t=1}^{N-\tau/\Delta T} \Delta\phi(t)}{N - \tau/\Delta T} \ , \tag{B.2}$$

where N is the total number of bins. The characteristic behaviour of the Allan variance as a function of τ depends on phase noise, both white and flicker, at short time scales. At longer times frequency noise, again both phase and flicker, as well as random frequency walk dominate [139]. The Allan variance as a function of integration time is then plotted as a log-log plot. In the case of white and flicker phase noise a slope of -2 is predicted. White noise of frequency produces a slope of -1. Flicker noise of frequency results in a flat Allan variance, known as the "flicker floor", before the random walk of frequency imprints a positive slope of 1 on the Allan variance [139]. The timescales for each regime depend on the experimental system. In our set–up, where we examine integration times of up to 100 seconds, we do not expect to observe the dominating characteristics of either

flicker or random frequency noise.

A related stability measure is the degree of first–order temporal coherence, $g^{(1)}$, which is the normalised auto correlation function of the electric field [140]. The degree of coherence therefore tells us how strongly correlated the signal is at times t and $t + \tau$, with $g^{(1)} = 1(0)$ meaning maximum (zero) correlation. Following the approximations in [137] we obtain

$$g^{(1)}(\tau) = \exp(-\frac{\langle \Delta\Phi(t,\tau)^2 \rangle_t}{2}) \ . \tag{B.3}$$

B.3 Results

The Allan variance is measured for integration times from 10^{-7} to 10^2 s, which sufficiently includes the timescales that are relevant for our application, Fig. B.3. For the shortest timescales, 100 ns, the Allan variance of the master–slave beat note (blue circles), $\sigma^2 = 2.6 \times 10^{10}$ rad^2/s^2 and decays with increasing integration time with a 2–part power law. From 10^{-7} to 10^{-3} s the power law decay of the master–slave Allan variance is fitted with a slope of $-1.95(1)$ (brackets denote statistical error). Comparing this slope to the theoretical predicted value of -2 for white and flicker phase noise we find that these must be the dominant noise sources over the given timescales. For integration times larger than 10^{-3} s the power law fit of the master–slave has a slope of $-1.19(4)$, which corresponds to the onset of white frequency noise.

Indicative of the increased phase noise, the Allan variance of the master–slave–TA beat note (red diamonds) has a maximum value over an order of magnitude higher, at 4.1×10^{11} rad^2/s^2. However the white frequency noise is similar to that of the master–slave configuration, and the values converge at timescales of $\sim 10^{-1}$ s, as can be seen in Fig. B.3.

Our method of detecting the phase noise is limited by the phase noise introduced by the function generators clocks. We measure the Allan variance of these, also shown in Fig. B.3 as the black squares. The laser phase noise is close to our experimental resolution for intermediate timescales around 1 ms, and it departs for longer times when frequency noise increases the laser system Allan variance.

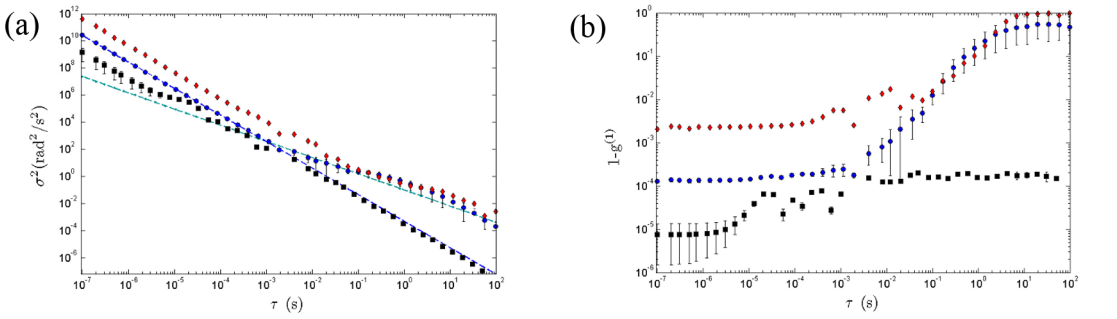

Figure B.3: (a) Measured Allan variance and (b) first–order degree of temporal coherence for the master–slave (blue circles) and master–slave–TA (red diamonds) configurations. Also shown for the Allan variance are linear fits indicating the timescales that white and flicker phase noise (for times up to 1 ms, with a slope of -1.95, blue line) and white frequency noise (for times longer than 1 ms and indicated by a slope of -1.19, turquoise line) dominate. The black squares show the lower limit of the phase stability due to noise in the electronic frequency sources. Errorbars are single standard deviations from measurements.

The Allan variance allows one to identify the nature of the noise sources, from the slope in the log–log domain, along with the phase noise normalised by the timescale. The latter is particularly useful as it can be used as a direct figure of merit between different oscillators measured for different integration times. Complementary to this the degree of first–order coherence, $g^{(1)}$, gives an absolute value for the predictability of the system. For clarity $1 - g^{(1)}$, the departure from perfect temporal coherence, is shown for the beat note data in the lower Fig. B.3. We find a nearly flat function for small timescales up to 10^{-3} s, after which the the coherence reduces until the beatnote shows little predictability for times larger than ~ 1 s. As for the Allan variance, the departure from perfect correlation for the system that includes the TA is about one order of magnitude larger at small timescales but merges with the behaviour of the system without the TA for times $> 10^{-1}$.

From the Wiener-Khinchin theorem, see e.g. [141], it is found that the power spectral density (PSD) is equivalent to the Fourier transform of the auto correlation function. We calculate the normalised PSD from the measured $g^{(1)}$ and obtain the power in the main frequency component (f_{rf}) from the amplitude of the PSD in the zeroth frequency bin ($\Delta f \approx 260$ Hz, the frequency resolution of

the data) [137]. The data obtained here imply that for timescales up to 100 ms at least 99.984(2)% of the power in the slave is phase locked with the master laser, slightly reducing to better than 99.72% when comparing the phase locking of the TA to the master laser, including the intermediate amplification of the slave.

B.4 Conclusions

We have presented a quasi–monoblock external–cavity diode laser with a large tuning range. With the aim of using the laser in a degenerate quantum gases experiment we have amplified the power with an injection locked slave laser and a commercial tapered amplifier. Etalon–effects produce local maxima in the slave output power as a function of the drive current, which shows a temperature dependence. The phase stability of the slave laser with respect to the master laser is characterised from the results of a beat note experiment. For this, the Allan variance and the degree of first–order temporal coherence (using the auto correlation function of the electric field) were measured over integration times ranging from 10^{-7} to 10^{2} s. The phase stability is uniform up to integration times of 10 ms. This sufficiently covers the timescales of interest for the intended applications. In log–log space the Allan variance has a multi-part power law, the slope depending on the type of noise. With a double linear fit to the Allan variance we obtain a slope of -1.95 for the first part, which changes around $\tau = 10^{-3}$ to a slope of -1.19. These are close to the theoretical slopes of -2 for flicker and white phase noise and -1 for white frequency noise. Further amplification with a tapered amplifier increases the Allan variance by an order of magnitude for short timescales. The additional phase noise from the TA becomes negligible for larger timescales when the frequency noise dominates. We also obtain the power spectral density from the first–order temporal coherence function and find the power in f_{rf} to be better than 99.98% without and better than 99.7% with the TA at times $10^{-7} - 10^{-3}$ s.

We note that as seed powers of ≤ 0.5 mW are required for injection of the slave laser, the system can easily be expanded to include multiple slave lasers. To produce an array of several frequency shifted lasers, each slave laser may be modulated with a different frequency, and the sidebands are then phase locked

to the master laser [137]. In this way it is possible to create an array of phase coherent sources.

Appendix C

Trap frequency and temperature - additional information

Using the approximation of a Boltzmann-distribution of atoms in a potential and assuming a harmonic trap, the initial atom distribution is:

$$n = n_0 \exp(-\frac{M_{\mathrm{Rb}}\omega^2 x^2}{2k_B T}) \tag{C.1}$$

and we can see that this is equivalent to a spatial Gaussian distribution with width

$$\sigma_0^2 = \frac{k_B T}{M_{\mathrm{Rb}}\omega^2} \ . \tag{C.2}$$

The Boltzmann distribution of velocity leads to an increase of the atom distributions' width, σ, with time of flight t_{tof} [44]:

$$\begin{aligned} \sigma^2(t_{\mathrm{tof}}) &= \sigma_0^2 + \sigma_v^2(t_{\mathrm{tof}}) && \text{(C.3)} \\ &= \sigma_0^2 + \frac{k_B T}{M_{\mathrm{Rb}}} t_{\mathrm{tof}}^2 && \text{(C.4)} \\ &= \frac{k_B T}{M_{\mathrm{Rb}}}(\frac{1}{\omega^2} + t_{\mathrm{tof}}^2) \ , && \text{(C.5)} \end{aligned}$$

from which temperature and trap frequency can be extracted.

References

[1] J.D. Pritchard *et al.*, *Demonstration of an Inductively Coupled Ring Trap for Cold Atoms*, New J. Phys. **14**, 103047 (2012)

[2] P. F. Griffin, E. Riis, and A. S. Arnold, *A Smooth, Inductively Coupled Ring Trap for Atoms*, Phys. Rev. A **77**, 051402 (2008)

[3] S. Moulder *et al.*, *Quantized Supercurrent Decay in an Annular Bose-Einstein Condensate*, Phys. Rev. A **86**, 013629 (2012)

[4] G. E. Marti, R. Olf, and D. M. Stamper-Kurn, *A Collective Excitation Interferometer for Rotation Sensing with a Trapped Bose-Einstein Condensate*, arXiv:1210.0033(2012)

[5] R. Geiger *et al.*, *Detecting Inertial Effects with Airborne Matter-Wave Interferometry*, Nature Comm. **2**, 474 (2011)

[6] A. Peters, K. Y. Chung, and S. Chu, *High-Precision Gravity Measurements using Atom Interferometry*, Metrologia **38**, 21 (2001)

[7] A. Lenef *et al.*, *Rotation Sensing with an Atom Interferometer*, Phys. Rev. Lett. **78**, 760 (1997)

[8] S. Gupta, K. Dieckmann, Z. Hadzibabic, and D. E. Pritchard, *Contrast Interferometry using Bose-Einstein Condensates to Measure h/m and α*, Phys. Rev. Lett. **89**, 140401 (2002)

[9] S. Dimopoulos, P. W. Graham, J. M. Hogan, and M. A. Kasevich, *Testing General Relativity with Atom Interferometry*, Phys. Rev. Lett. **98**, 111102 (2007)

[10] L. Maleki, *Space Tests of Relativistic Gravity with Precision Clocks and Atom Interferometers*, Gen. Rel. Gravit. **40**, 895 (2008)

[11] M. A. Hohensee and H. Müller, *Precision Tests of General Relativity with Matter Waves*, J. Mod. Opt. **58**, 2021 (2011)

[12] F. Sorrentino *et al.*, *The Space Atom Interferometer Project: Status and Prospects*, JPCS **327**, 012050 (2011)

[13] J. M. McGuirk *et al.*, *Sensitive Absolute-Gravity Gradiometry using Atom Interferometry*, Phys. Rev. A **65**, 033608 (2002)

[14] N. Yu, J. M. Kohel, J. R. Kellogg, and L. Maleki, *Development of an Atom-Interferometer Gravity Gradiometer for Gravity Measurement from Space*, App. Phys. B **84**, 647 (2006)

[15] N. Yu and M. Tinto, *Gravitational Wave Detection with Single-Laser Atom Interferometers*, Gen. Rel. Gravit. **43**, 1943 (2011)

[16] S. Dimopoulos *et al.*, *Gravitational Wave Detection with Atom Interferometry*, Phys. Lett. B **678**, 37 (2009)

[17] Y.-J. Wang *et al.*, *Atom Michelson Interferometer on a Chip using a Bose-Einstein Condensate*, Phys. Rev. Lett. **94**, 090405 (2005)

[18] T. Schumm *et al.*, *Matter-Wave Interferometry in a Double Well on an Atom Chip*, Nature Physics **1**, 57 (2005)

[19] A. Ashkin, *Applications of Laser Radiation Pressure.*, Science **210**, 1081 (1980)

[20] S. Chu *et al.*, *Three-Dimensional Viscous Confinement and Cooling of Atoms by Resonance Radiation Pressure*, Phys. Rev. Lett. **55**, 48 (1985)

[21] P. L. Gould, G. A. Ruff, and D. E. Pritchard, *Diffraction of Atoms by Light: The Near-Resonant Kapitza-Dirac Effect* **56**, 827 (1986)

[22] E. M. Rasel *et al.*, *Atom Wave Interferometry with Diffraction Gratings of Light*, Phys. Rev. Lett. **75**, 2633 (1995)

[23] M. Amniat-Talab, S. Guérin, N. Sangouard, and H. Jauslin, *Atom-Photon, Atom-Atom, and Photon-Photon Entanglement Preparation by Fractional Adiabatic Passage*, Phys. Rev. A **71**, 023805 (2005)

[24] E. Hagley *et al.*, *Generation of Einstein-Podolsky-Rosen Pairs of Atoms*, Phys. Rev. Lett. **79**, 1 (1997)

[25] M. Lettner *et al.*, *Remote Entanglement between a Single Atom and a Bose-Einstein Condensate*, Phys. Rev. Lett. **106**, 1 (2011)

[26] S. Inouye *et al.*, *Superradiant Rayleigh Scattering from a Bose-Einstein Condensate*, Science **285**, 571 (1999)

[27] A. Einstein, *Über einen die Erzeugung und Verwandlung des Lichtes betreffenden heuristischen Gesichtspunkt*, Annalen der Physik **322**, 132 (1905)

[28] L. de Broglie, *Waves and Quanta*, Nature **112**, 540 (1923)

[29] O. Carnal and J. Mlynek, *Young's Double-Slit Experiment with Atoms: A Simple Atom Interferometer*, Phys. Rev. Lett. **66**, 2689 (1991)

[30] L. P. Parazzoli, A. M. Hankin, and G. W. Biedermann, *Observation of Free-Space Single-Atom Matter Wave Interference*, Phys. Rev. Lett. **109**, 230401 (2012)

[31] M. Arndt *et al.*, *Wave-Particle Duality of C_{60} Molecules*, Nature **401**, 680 (1999)

[32] M. E. Zawadzki, P. F. Griffin, E. Riis, and A. S. Arnold, *Spatial Interference from Well-Separated Split Condensates*, Phys. Rev. A **81**, 043608 (2010)

[33] T. L. Gustavson, A. Landragin, and M. A. Kasevich, *Rotation Sensing with a Dual Atom-Interferometer Sagnac Gyroscope*, Classical and Quantum Gravity **17**, 2385 (2000)

[34] C. J. Foot, *Atomic Physics* (Oxford University Press, 2009)

[35] C. Cohen-Tannoudji and D. Guéry-Odelin, *Advances in Atomic Physics: an Overview* (World Scientific, 2011) ISBN 9789812774965

[36] C. J. Pethick and H. Smith, *Bose-Einstein Condensation in Dilute Gases* (Cambridge University Press, 2004)

[37] C. S. Adams and E. Riis, *Laser Cooling and Manipulation of Neutral Particles*, Prog. Quant. Electron. **21**, 1 (1997)

[38] H. J. Metcalf and P. van der Straten, *Laser Cooling and Trapping* (Springer Verlag New York, 1999)

[39] T. W. Hänsch and A. L. Schawlow, *Cooling of Gases by Laser Radiation*, Optics Comm. **13**, 68 (1975)

[40] P. D. Lett *et al.*, *Optical Molasses*, J. Opt. Soc. Am. B **6**, 2084 (1989)

[41] D. A. Steck, *Rubidium 87 D Line Data* (2001), `http://steck.us/alkalidata`

[42] E. L. Raab *et al.*, *Trapping of Neutral Sodium Atoms with Radiation Pressure*, Phys. Rev. Lett. **59**, 2631 (1987)

[43] P. D. Lett *et al.*, *Observation of Atoms Laser Cooled below the Doppler Limit*, Phys. Rev. Lett. **61**, 169 (1988)

[44] D. S. Weiss *et al.*, *Optical Molasses and Multilevel Atoms: Experiment*, J. Opt. Soc. Am. B **6**, 2072 (1989)

[45] P. J. Ungar, D. S. Weiss, E. Riis, and S. Chu, *Optical Molasses and Multilevel Atoms: Theory*, J. Opt. Soc. Am. B **6**, 2058 (1989)

[46] J. Dalibard and C. Cohen-Tannoudji, *Laser Cooling below the Doppler Limit by Polarization Gradients: Simple Theoretical Models*, J. Opt. Soc. Am. B **6**, 2023 (1989)

[47] H. J. Metcalf, *Laser Cooling and Trapping of Atoms*, J. Opt. Soc. Am. B **28**, 49 (2003)

[48] W. D. Phillips *et al.*, *Optical Molasses: The Coldest Atoms Ever*, Phys. Scripta **T34**, 20 (1991)

[49] A. Peters *et al.*, *Precision Atom Interferometry*, Phil. Trans. of the Royal Soc. A **355**, 2223 (1997)

[50] A. D. Cronin, J. Schmiedmayer, and D. E. Pritchard, *Optics and Interferometry with Atoms and Molecules*, Rev. Mod. Phys. **81**, 1051 (2009)

[51] M. Kasevich and S. Chu, *Atomic Interferometry using Stimulated Raman Transitions*, Phys. Rev. Lett. **62**, 181 (1991)

[52] D. W. Keith, C. R. Ekstrom, Q. A. Turchette, and D. E. Pritchard, *An Interferometer for Atoms*, Phys. Rev. Lett. **66**, 2693 (1991)

[53] S. Gupta, A. E. Leanhardt, A. D. Cronin, and D. E. Pritchard, *Coherent Manipulation of Atoms with Standing Light Waves*, C. R. Acad. Sci. Paris **2147**, 479 (2001)

[54] J. H. T. Burke and C. A. Sackett, *Scalable Bose-Einstein-Condensate Sagnac Interferometer in a Linear Trap*, Phys. Rev. A **80**, 061603 (2009)

[55] T. L. Gustavson, *Precision Rotation Sensing using Atom Interferometry*, Ph.D. thesis (2000)

[56] T. Müller *et al.*, *Versatile Compact Atomic Source for High-Resolution Dual Atom Interferometry*, Phys. Rev. A **76**, 063611 (2007)

[57] D. S. Hall, M. R. Matthews, C. E. Wieman, and E. A. Cornell, *Measurements of Relative Phase in Two-Component Bose-Einstein Condensates*, Phys. Rev. Lett. **81**, 1543 (1998)

[58] K. Bongs and K. Sengstock, *Physics with Coherent Matter Waves*, Rep. Prog. Phys **67**, 907 (2004)

[59] S. Gasiorowicz, *Quantum Physics* (Jon Wiley and Sons, 1974)

[60] W. Ketterle, D. S. Durfee, and D. M. Stamper-Kurn, *Making, Probing and Understanding Bose-Einstein Condensates*, Proceedings of the International School of Physics Enrico Fermi Course CXL, 67(1999)

[61] M. H. Anderson *et al.*, *Observation of Bose-Einstein Condensation in a Dilute Atomic Vapor*, Science **269**, 198 (1995)

[62] K. B. Davis *et al.*, *Evaporative Cooling of Sodium Atoms.*, Phys. Rev. Lett. **74**, 5202 (1995)

[63] A. Jamison, J. N. Kutz, and S. Gupta, *Atomic Interactions in Precision Interferometry using Bose-Einstein Condensates*, Phys. Rev. A **84**, 3643 (2011)

[64] G. Roati *et al.*, *Atom Interferometry with Trapped Fermi Gases*, Phys. Rev. Lett. **92**, 230402 (2004)

[65] R. A. Nyman *et al.*, *I.C.E.: A Transportable Atomic Inertial Sensor for Test in Microgravity*, App. Phys. B **84**, 673 (2006)

[66] C. Marzok *et al.*, *In Situ Ramsey Interferometry and Diffraction Echo with an Atomic Fermi Gas*, Phys. Rev. A **78**, 021602 (2008)

[67] D. S. Jin and C. A. Regal, *Fermi Gas Experiments*, in *The Enrico Fermi Summer School Course CLXVI on Ultracold Fermi Gases* (Nuovo Cimenta B&C, Rivista del Nuovo Ciment Giornale di Fisica, vol. 164, 2006) jILA Pub. 7872

[68] B. DeMarco, *Onset of Fermi Degeneracy in a Trapped Atomic Gas*, Science **285**, 1703 (1999)

[69] W. Ketterle and M. W. Zwierlein, *Making, Probing and Understanding Ultracold Fermi Gases*, in *Proceedings of the International School of Physics "Enrico Fermi", Course CLXIV, Varenna*, edited by M Inguscio, W Ketterle, and C Salomon (IOS Press, Amsterdam, 2008) p. 95

[70] S. Ospelkaus *et al.*, *Degenerate K-Rb Fermi-Bose Gas Mixtures with Large Particle Numbers*, J. Mod. Opt. **54**, 661 (2007)

[71] A. Peters, K. Y. Chung, and S. Chu, *Measurement of Gravitational Acceleration by Dropping Atoms*, Nature, 849(1999)

[72] S.-Y. Lan *et al.*, *Influence of the Coriolis Force in Atom Interferometry*, Phys. Rev. Lett. **108**, 090402 (2012)

[73] O. Garcia *et al.*, *Bose-Einstein-Condensate Interferometer with Macroscopic Arm Separation*, Phys. Rev. A **74**, 031601 (2006)

[74] H. Müller *et al.*, *Atom Interferometry with up to 24-Photon-Momentum-Transfer Beam Splitters*, Phys. Rev. Lett. **100**, 180405 (2008)

[75] S. Chiow, T. Kovachy, H.-C. Chien, and M. A. Kasevich, *102ℏk Large Area Atom Interferometers*, Phys. Rev. Lett. **107**, 130403 (2011)

[76] C. Ryu *et al.*, *Observation of Persistent Flow of a Bose-Einstein Condensate in a Toroidal Trap*, Phys. Rev. Lett. **99**, 260401 (2007)

[77] S. Beattie, S. Moulder, R. J. Fletcher, and Z. Hadzibabic, *Persistent Currents in Spinor Condensates*, Phys. Rev. Lett. **110**, 025301 (2013)

[78] A. Ramanathan *et al.*, *Superflow in a Toroidal Bose-Einstein Condensate: An Atom Circuit with a Tunable Weak Link*, Phys. Rev. Lett. **106**, 130401 (2011)

[79] L. J. Garay, J. R. Anglin, J. I. Cirac, and P. Zoller, *Sonic Analog of Gravitational Black Holes in Bose-Einstein Condensates*, Phys. Rev. Lett. **85**, 4643 (2000)

[80] J. Sauer, M. Barrett, and M. Chapman, *Storage Ring for Neutral Atoms*, Phys. Rev. Lett. **87**, 270401 (2001)

[81] A. S. Arnold, C. Garvie, and E. Riis, *Large Magnetic Storage Ring for Bose-Einstein Condensates*, Phys. Rev. A **73**, 1 (2006)

[82] A. S. Arnold, *Adaptable-Radius, Time-Orbiting Magnetic Ring Trap for Bose Einstein Condensates*, J. Phys. B **37**, L29 (2004)

[83] S. Gupta *et al.*, *Bose-Einstein Condensation in a Circular Waveguide*, Phys. Rev. Lett. **95**, 1 (2005)

[84] K. Henderson, C. Ryu, C. MacCormick, and M. G. Boshier, *Experimental Demonstration of Painting Arbitrary and Dynamic Potentials for Bose-Einstein Condensates*, New J. Phys. **11**, 043030 (2009)

[85] G. D Bruce *et al.*, *A Smooth, Holographically Generated Ring Trap for the Investigation of Superfluidity in Ultracold Atoms*, Phys. Scripta **T143**, 014008 (2011)

[86] S. Franke-Arnold *et al.*, *Optical Ferris Wheel for Ultracold Atoms.*, Opt. Express **15**, 8619 (2007)

[87] S. K. Schnelle *et al.*, *Versatile Two-Dimensional Potentials for Ultra-cold Atoms*, Opt. Express **16**, 1405 (2008)

[88] A. S. Arnold, *Extending Dark Optical Trapping Geometries.*, Opt. Lett. **37**, 2505 (2012)

[89] O. Zobay and B. Garraway, *Two-Dimensional Atom Trapping in Field-Induced Adiabatic Potentials*, Phys. Rev. Lett. **86**, 1195 (2001)

[90] W. H. Heathcote, E. Nugent, B. T. Sheard, and C. J. Foot, *A Ring Trap for Ultracold Atoms in an RF-Dressed State*, New J. Phys. **10**, 043012 (2008)

[91] I. Lesanovsky and W. von Klitzing, *Time-Averaged Adiabatic Potentials: Versatile Matter-Wave Guides and Atom Traps*, Phys. Rev. Lett. **99**, 083001 (2007)

[92] B. Sherlock *et al.*, *Time-Averaged Adiabatic Ring Potential for Ultracold Atoms*, Phys. Rev. A **83**, 043408 (2011)

[93] O. Morizot *et al.*, *Ring Trap for Ultracold Atoms*, Phys. Rev. A **74**, 023617 (2006)

[94] D. E. Pritchard, *Cooling Neutral Atoms in a Magnetic Trap for Precision Spectroscopy*, Phys. Rev. Lett. **51**, 1336 (1983)

[95] T. Bergeman, G. Erez, and H. J. Metcalf, *Magnetostatic Trapping Fields for Neutral Atoms.*, Phys. Rev. A **35**, 1535 (1987)

[96] A. L. Migdall *et al.*, *First Observation of Magnetically Trapped Neutral Atoms.*, Phys. Rev. Lett. **54**, 2596 (1985)

[97] Y.-J. Lin *et al.*, *Rapid Production of ^{87}Rb Bose-Einstein Condensates in a Combined Magnetic and Optical Potential*, Phys. Rev. A **79**, 063631 (2009)

[98] W. Petrich, M. H. Anderson, J. R. Ensher, and E. A. Cornell, *Stable, Tightly Confining Magnetic Trap for Evaporative Cooling of Neutral Atoms*, Phys. Rev. Lett. **74**, 3352 (1995)

[99] J. Denschlag, D. Cassettari, and J. Schmiedmayer, *Guiding Neutral Atoms with a Wire*, Phys. Rev. Lett. **82**, 2014 (1999)

[100] A. Haase, D. Cassettari, B. Hessmo, and J Schmiedmayer, *Trapping Neutral Atoms with a Wire*, Phys. Rev. A **64**, 043405 (2001)

[101] J. Denschlag *et al.*, *A Neutral Atom and a Wire: Towards Mesoscopic Atom Optics*, App. Phys. B **69**, 291 (1999)

[102] W. Nolting, *Grundkurs Theoretische Physik 3 - Elektrodynamik* (Springer Verlag Berlin Heidelberg, 2004)

[103] R. H. Good, *Elliptic Integrals, the Forgotten Functions*, Eur. Phys. J. **22**, 119 (2001)

[104] C. R. Paul, *Inductance: Loop and Partial* (Wiley, 2010) ISBN 9780470561225

[105] E. B. Rosa, *The Self and Mutual Inductances of Linear Conductors*, Bulletin of the National Bureau of Standards **4**, 301 (1908)

[106] J. D. Pritchard, Note: code for the finite element calculations as part of the ring trap simulations was written and implemented by J. D. Pritchard

[107] A. E. Leanhardt *et al.*, *Bose-Einstein Condensates near a Microfabricated Surface*, Phys. Rev. Lett. **90**, 100404 (2003)

[108] P. Krüger *et al.*, *Potential Roughness near Lithographically Fabricated Atom Chips*, Phys. Rev. A **76**, 063621 (2007)

[109] J.-B. Trebbia *et al.*, *Roughness Suppression via Rapid Current Modulation on an Atom Chip*, Phys. Rev. Lett. **98**, 263201 (2007)

[110] M. Vangeleyn, *Atom trapping in Non-Trivial Geometries for Micro-Fabrication Applications*, Ph.D. thesis, University of Strathclyde (2011)

[111] C. E. Wieman and L. Hollberg, *Using Diode Lasers for Atomic Physics*, Rev. Sci. Instrum **62**, 1 (1991)

[112] L. Ricci *et al.*, *A Compact Grating-Stabilized Diode Laser System for Atomic Physics*, Opt. Commun. **117**, 541 (1995)

[113] A. S. Arnold, J. S. Wilson, and M. G. Boshier, *A Simple Extended-Cavity Diode Laser*, Rev. Sci. Instrum **69**, 1236 (1998)

[114] S. D. Saliba, M. Junker, L. D. Turner, and R. E. Scholten, *Mode Stability of External Cavity Diode Lasers*, Appl. Opt. **48**, 6692 (2009)

[115] K. J. Weatherill, *A CO_2 Laser Lattice Experiment for Cold Atoms*, Ph.D. thesis, Durham University (2007)

[116] C. J. Hawthorn, K. P. Weber, and R. E. Scholten, *Littrow Configuration Tunable External Cavity Diode Laser with Fixed Direction Output Beam*, Rev. Sci. Instrum **72**, 4477 (2001)

[117] P. Siddons, C. S. Adams, C. Ge, and I. G. Hughes, *Absolute Absorption on Rubidium D Lines: Comparison between Theory and Experiment*, J. Phys. B **41**, 155004 (2008)

[118] W. Demtröder, *Laser Sepctroscopy*, Vol. 2 (Springer Verlag Berlin Heidelberg, 2008)

[119] J. M. Goldwin, *Quantum Degeneracy and Interactions in the ^{87}Rb-^{40}K Bose-Fermi Mixture*, Ph.D. thesis, University of Colorado (2005)

[120] S. Y. Mak and K. Young, *Determination of the Self-Inductance of a Metal Ring*, Phys. Educ. **21**, 111 (1986)

[121] K. Dieckmann, R. Spreeuw, M. Weidemüller, and J. Walraven, *Two-Dimensional Magneto-Optical Trap as a Source of Slow Atoms*, Phys. Rev. A **58**, 3891 (1998)

[122] I. Gotlibovych *et al.*, *A Compact Single-Chamber Apparatus for Bose-Einstein Condensation of* ^{87}Rb (2012)

[123] M. Greiner, I. Bloch, T. Hänsch, and T. Esslinger, *Magnetic Transport of Trapped Cold Atoms over a Large Distance*, Phys. Rev. A **63**, 031401 (2001)

[124] J. Burke, B. Deissler, K. Hughes, and C. Sackett, *Confinement Effects in a Guided-Wave Atom Interferometer with Millimeter-Scale Arm Separation*, Phys. Rev. A **78**, 023619 (2008)

[125] J. I. Gillen, *The Quantum Gas Microscope*, Ph.D. thesis, Harvard University (2009)

[126] W. Ketterle and N. J. V Druten, *Evaporative Cooling of Trapped Atoms*, Adv. At. Mol. Opt. Phys.(1996)

[127] R. Grimm, M. Weidemüller, and Y. B. Ovchinnikov, *Optical Dipole Traps for Neutral Atoms*, Adv. At. Mol. Opt. Phys. **42**, 95 (2000)

[128] C. S. Adams *et al.*, *Evaporative Cooling in a Crossed Dipole Trap.*, Phys. Rev. Lett. **74**, 3577 (1995)

[129] P. L. Kapitza and P. a. M. Dirac, *The reflection of electrons from standing light waves*, Math. Proc. Cambridge **29**, 297 (1933)

[130] S. Wu, Y.-J. Wang, Q. Diot, and M. Prentiss, *Splitting Matter Waves using an Optimized Standing-Wave Light-Pulse Sequence*, Phys. Rev. A **71**, 043602 (2005)

[131] J. Schoser *et al.*, *Intense Source of Cold Rb Atoms from a Pure Two-Dimensional Magneto-Optical Trap*, Phys. Rev. A **66**, 023410 (2002)

[132] K. J. Weatherill *et al.*, *A Versatile and Reliably Reusable Ultrahigh Vacuum Viewport.*, Rev. Sci. Instrum **80**, 026105 (2009)

[133] M. Theis, *Optical Feshbach Resonances in a Bose-Einstein Condensate*, Ph.D. thesis, Leopold-Franzens-Universität Innsbruck (2005)

[134] E. W. Streed *et al.*, *Large Atom Number Bose-Einstein Condensate Machines*, Rev. Sci. Instrum **77**, 023106 (2006)

[135] D. Voigt, E. C. Schilder, R. J. C. Spreeuw, and H. B. van Linden van den Heuvell, *Characterization of a High-Power Tapered Semiconductor Amplifier System*, Appl. Phys. B. **72**, 279 (2001)

[136] R. A. Nyman *et al.*, *Tapered-Amplified Antireflection-Coated Laser Diodes for Potassium and Rubidium Atomic-Physics Experiments*, Rev. Sci. Instrum **77**, 033105 (2006)

[137] M. J. Snadden, R. B. M. Clarke, and E. Riis, *Injection-Locking Technique for Heterodyne Optical Phase Locking of a Diodelaser*, Opt. Lett. **22**, 892 (1997)

[138] D. W. Allan, *Statistics of Atomic Frequency Standards*, in *Proceedings of the IEEE*, Vol. 54 (1966) p. 221

[139] J. Vanier and C. Audoin, *The Quantum Physics of Atomic Frequency Standards*, Vol. 2 (IOP Publishing Ltd, 1989)

[140] R. Loudon, *The Quantum Theory of Light* (Oxford Science Publications, 2000)

[141] C. W. Gardiner, *Handbook of Stochastic Methods* (Springer Verlag, 2004)